ENTANGLEMENT AND HALL VISCOSITY

BY

THOMAS TUEGEL

DISSERTATION

Submitted in partial fulfillment of the requirements
for the degree of Doctor of Philosophy in Physics
in the Graduate College of the
University of Illinois at Urbana-Champaign, 2018

Urbana, Illinois

Doctoral Committee:

Professor Michael Stone, Chair
Associate Professor Taylor L. Hughes, Director of Research
Associate Professor Smitha Vishveshwara
Assistant Professor Gregory MacDougall

Abstract

This dissertation studies quantum entanglement in relation to the geometric response known as Hall viscosity. We begin by reviewing geometric response in the quantum Hall effect in comparison to its well-known electromagnetic response, Hall conductivity. We develop an understanding of momentum transport due to Hall viscosity in analogy to charge transport under Hall conductivity. We apply our momentum transport argument to continuum and lattice models of the quantum Hall effect. We also leverage this insight to reveal a previously-unrecognized manifestation of Hall viscosity: the acoustic Faraday effect in superfluid ^{3}He$-$B. We suggest that the acoustic Faraday effect is a new platform for the direct observation of Hall viscosity in ^{3}He$-$B and other systems. We then turn our focus to the entanglement spectrum. We calculate the momentum polarization of lattice models of the quantum Hall effect to determine the Hall viscosity based on the entanglement spectrum, revealing the close connection between geometric response and entanglement. Finally, we turn away from the quantum Hall effect to consider other topological insulators; we use the entanglement spectrum to develop a topological classification of composite systems comprising components of topological phases in different dimensions. Our composite topological index generalizes classification of weak and antiferromagnetic topological insulators. We predict the presence of topological bound states localized to defects in systems that are trivial under all other topological classifications.

To Erin Rebecca and Rosalind Grace

Acknowledgments

I am profoundly grateful to my advisor, Taylor L. Hughes; his guidance has been indispensable to my work and to my growth as a physicist.

I would also like to thank the Department of Physics at the University of Illinois Urbana–Champaign for their support and for the opportunities I have had here as a student, a researcher, and a teacher.

I thank Taylor, Michael Stone, Smitha Vishveshwara, and Gregory MacDougall for agreeing to take the time to serve on my Doctoral Committee.

I also thank Victor Chua for his collaboration and for many illuminating discussions about physics.

I thank James A. Sauls, Hassan Shapourian, and Vatsal Dwivedi for their discussions which influenced my work.

I am also grateful to many people whose discussions were important to my education; there are too many to thank them all individually, but among them are Wladimir Benalcazar, Anthony Hegg, Mayukh Khan, Ian Mondragon-Shem, Srinidhi Ramamurthy, and Garrett Vanacore.

I am grateful to my parents, Eric and Loretta, who have brought me up with every opportunity in life.

Most importantly, I must thank my wife Erin; her love, support, and patience have made everything possible.

Contents

List of Figures

Chapter 1

Introduction

The topological responses of the quantum Hall effect have been studied intensely for more than three decades, beginning with the quantized integer and fractional Hall conductance [2, 32, 69, 90, 104, 105, 127, 137] and more recently the remarkable geometric responses. Quantum Hall systems exhibit a dissipationless geometric response known as Hall viscosity [1, 2, 4, 7, 9, 12, 14, 15, 17, 20, 21, 34, 42–45, 49, 51, 57, 58, 62, 73, 92, 93, 104, 108, 120, 128, 136, 138, 142], which they share with other liquids that break time-reversal symmetry [4]: not only the quantum Hall effect, but also the quantum anomalous Hall effect [57, 58], and chiral superconductors/superfluids [14, 51, 104]. It has also been predicted in gapless systems where strain fields couple to the low-energy electronic degrees of freedom as gauge fields (emergent elastic gauge fields) such as graphene [24], borophene [141], and Weyl semimetals [24, 68, 75]. Chapter 2 gives a generic description of Hall viscosity in isotropic two-dimensional systems, which may be understood as an effect of a Berry curvature of the ground state in analogy to the Hall conductivity [7, 73]. We extend the analogy to describe momentum transport due to Hall viscosity in the same manner as charge transport due to Hall conductivity. Momentum transport under adiabatic conditions is used to quantify the Hall viscosity of the integer quantum Hall effect in ordinary Landau levels and linearly-dispersing Dirac–Landau levels. Chapter 3 extends the momentum transport method to lattice models of the quantum Hall effect, overcoming difficulties defining momentum transport in systems without continuous translation symmetry.

The material presented in this section was previously published in: Thomas I. Tuegel and Taylor L. Hughes. “Hall viscosity and momentum transport in lattice and continuum models of the integer quantum Hall effect in strong magnetic fields”. Phys. Rev. B **92**, 165127 (2015). DOI: 10.1103/PhysRevB.92.165127 and Thomas I. Tuegel and Taylor L. Hughes. “Hall viscosity and the acoustic Faraday effect”. Phys. Rev. B **96**, 174524 (2017). DOI: 10.1103/PhysRevB.96.174524. Some text has been modified.

Despite an exhaustive theoretical description of the geometric responses of the quantum Hall effect developed over more than two decades, no experiment has directly observed Hall viscosity in a two-dimensional electron gas. The viscosity drives momentum transport, and the difficulty in directly probing the 2DEG momentum is a significant obstacle to this observation. However, the charge current and density responses at finite wavevector [52, 87], and the density response to spatial curvature [2, 17] have been predicted to have corrections due to the Hall viscosity, and may lead to more realistic experimental proposals in the integer and fractional quantum Hall contexts. Indeed, proposals exist to measure the Hall viscosity response [55] and the electron viscosity more generally [129], but none have yet been realized. Interestingly, the effects of the Hall viscosity have been observed in a non-electronic system: a photonic analog of the quantum Hall effect [112], and other recent articles propose to measure the Hall viscosity in superfluids [37] and (classical) chiral active fluids [8]. Such systems may be a more expedient route to observing this response because the momentum can be probed directly. In Chapter 4, we explore another consequence of Hall viscosity: circular birefringence of transverse acoustic waves, also known as the acoustic Faraday effect. In fact, the acoustic Faraday effect has already been observed in experiments in ^{3}He$-$B, but the connection to the Hall viscosity was not appreciated at the time. We expect that superfluid ^{3}He$-$B could serve as a new platform for the experimental study of geometric responses. The connection to Hall viscosity is also relevant in other contexts where the acoustic Faraday effect has been observed or predicted, e.g., in the crystal $Tb_3Ga_5O_{12}$ [123, 124] or in superconductor vortex lattices [27, 28, 118].

In the second half of this dissertation, we shift to the application of methods based on the entanglement spectrum. The entanglement spectrum has come to popularity in the last decade as a purely-quantum classifier of condensed matter systems. Recently, the method has been applied to the study of artificial neural-network states [26, 88] to justify the remarkable efficiency of such representations of quantum states. The entanglement spectrum first gained popularity in a variety of applications including the study of topological phases in the quantum Hall effect [30, 74, 100, 119], spin chains [16, 25, 97, 126], topological insulators and superconductors [31, 98, 134], and others [22, 140]. The entanglement spectrum is found to correspond to the spectrum of the boundary theory in a topological phase [31, 134] (due to the

virtual boundary introduced to calculate the entanglement spectrum) in an elucidation of the bulk-boundary correspondence; that realization led to the development of a family of *bulk* entanglement spectrum methods [38, 39, 53, 54, 77, 110, 143], where an extensive cut throughout the system reveals the critical theory at the phase transition. Chapter 5 lays the groundwork for our applications of the entanglement spectrum.

In Chapter 6, we continue the study of Hall viscosity by using the entanglement spectrum to compute the Hall viscosity coefficient of lattice and continuum systems through the momentum polarization. The momentum polarization was initially proposed to calculate the topological spin and central charge of the conformal field theory at the edge of a topological phase; these data are extracted from the expectation value of a certain translation operator applied to a periodic system [130]. In addition to the universal features of the conformal edge theory, the momentum polarization also contains a non-universal contribution from the Hall viscosity [142].

Finally, we leave the Hall viscosity behind to discuss the classification of topological phases based on the entanglement spectrum. Gapped free-fermion systems exhibit a wide variety of symmetry-protected topological (SPT) phases. Free-fermion SPT phases strongly protected by global time-reversal, charge-conjugation, or chiral symmetries are classified under the "tenfold way" of Altland-Zirnbauer classes [11, 59, 60, 63, 101, 102, 109, 113]. Descending from the strong SPT phases are weaker phases protected by local translation (weak TIs) [36, 85, 107], point-group (crystalline TIs) [10, 35], or antiferromagnetic (AFTIs) [29, 84, 117] symmetries. Defects, i.e., local symmetry violations generate stable, localized bound states [103, 125]. In Chapter 7, we describe the classification of *composite* systems comprising components of different dimensionalities descending from the strong SPT phases.

Chapter 2

Hall Viscosity

2.1 Introduction

Hall viscosity is a non-dissipative geometric response of time-reversal symmetry breaking fluids [4]. Under shear strain, the viscosity tensor η relates the stress tensor T to the strain rate $\dot{w}$:

$$T^{\mu\nu} = -\eta^{\mu\nu\alpha\beta}\dot{w}_{\alpha\beta}; \tag{2.1}$$

the (finite) strain tensor is

$$w_{\alpha\beta} = \frac{1}{2}\left(g_{\mu\nu} - g^{(0)}_{\mu\nu}\right) \tag{2.2}$$

where $g^{(0)}_{\mu\nu}$ is the metric of the undeformed system [122] where the strain tensor is constructed from a symmetrized gradient of the local displacement u_α. In the limit of infinitesimal deformation along vector u, the definition reduces to the Lie derivative of the metric with respect to u [67, 122],

$$w_{\alpha\beta} = \mathcal{L}(u)g_{\alpha\beta} = \frac{1}{2}(\partial_\alpha u_\beta + \partial_\beta u_\alpha). \tag{2.3}$$

The dissipative contributions to the viscosity, e.g., the bulk and shear viscosities, then $\eta^{\mu\nu\alpha\beta}$ is symmetric under exchange of $(\mu\nu)$ with $(\alpha\beta)$. The non-dissipative Hall viscosity generates an antisymmetric contribution, i.e.,

$$\eta_H^{\mu\nu\alpha\beta} = -\eta_H^{\alpha\beta\mu\nu}. \tag{2.4}$$

The antisymmetric part of the viscosity tensor in a two-dimensional isotropic system is determined by a single parameter η_H, giving, in an orthonormal

The material presented in Chapter 2 was previously published in: Thomas I. Tuegel and Taylor L. Hughes. "Hall viscosity and momentum transport in lattice and continuum models of the integer quantum Hall effect in strong magnetic fields". Phys. Rev. B **92**, 165127 (2015). DOI: 10.1103/PhysRevB.92.165127. Some figures are reprinted with minor modifications. Some text and figure captions have been modified.

frame [4, 7],

$$\eta_H^{1112} = \eta_H^{1222} = -\eta_H \tag{2.5a}$$
$$\eta_H^{1122} = 0. \tag{2.5b}$$

The Hall viscosity can be calculated using a variety of different methods. The first calculations were performed via the adiabatic transport of the Hall fluid under shear strain on a torus [7, 73, 104, 128]. For Schrödinger electrons at integer filling factors, this type of calculation yields $\eta_H = \hbar\nu\rho/4$ where ρ is the electron number density, and ν is the integer filling fraction [7, 73, 104, 105]. More recently, Bradlyn, Goldstein, and Read [14] developed Kubo formulas for the Hall viscosity which obtain the same result. Also, a new possibility for calculating the Hall viscosity was proposed via the so-called momentum polarization entanglement technique [130, 142], though there is very little explicit discussion of the results of this method in the literature. Remarkably, from the adiabatic transport calculations it has been shown that for rotationally-invariant integer and fractional quantum Hall systems in large magnetic fields, the viscosity is quantized in units of the density [104] and takes the form

$$\eta_H = \frac{\kappa}{4}\hbar\rho \tag{2.6}$$

where κ is a universal number characterizing the particular integer/fractional quantum Hall phase, and ρ is the uniform electron number density. Generically, the Hall viscosity has units of $[\frac{\hbar}{\ell^2}]$ for some length scale ℓ, but it need not always retain such a clear quantization in terms of the particle density.

2.2 Hall conductivity and charge transport

Before considering the subject of momentum transport due to Hall viscosity, it is useful to review charge transport due to Hall conductivity. Recall the continuity equation for charge current:

$$\partial_t\rho + \partial_a J^a = 0 \tag{2.7}$$

where ρ is charge density and J is charge current. The Hall conductivity relates the charge current to the electric field via

$$J^a = \sigma^{ab}E_b. \tag{2.8}$$

The similarity to Eq. (2.1) becomes apparent when we consider that the electric field is a *flux rate* according to Faraday's law,

$$E_b = -\epsilon_{bc}\dot{\Phi}^c \tag{2.9a}$$
$$J^a = -\sigma^{ab}\epsilon_{bc}\dot{\Phi}^c. \tag{2.9b}$$

Time-reversal symmetry-breaking in the quantum Hall effect generates a quantized, antisymmetric conductivity,

$$\sigma^{ab} = \sigma_H \epsilon^{ab}. \tag{2.10}$$

Consider an cylinder of length L_x periodic in the y–direction with circumference L_y. Threading flux along the axis of the cylinder, i.e., $\dot{\Phi}_x \neq 0$, gives a Hall current in the same direction,

$$J^x = \sigma_H \dot{\Phi}^x. \tag{2.11}$$

The current transports charge from left to right along the axis of the cylinder. Imagine cutting the cylinder at $x = 0$; charge builds up in the right half at a rate given by

$$\partial_t Q = \int_0^{L_y} \mathrm{d}y \int_0^{L_x} \mathrm{d}x\, \partial_t \rho. \tag{2.12}$$

The continuity relation gives

$$\partial_t \rho = -\partial_x J^x - \partial_y J^y; \tag{2.13}$$

the latter term on the right-hand side integrates to zero due to periodic boundary conditions in the y-direction and the former term integrates to

$$\int_0^{L_x} \mathrm{d}x\, \partial_x J^x = J^x\big|_{x=0}^{L_x} = -J^x\big|_{x=0} \tag{2.14}$$

where we have assumed that $J^x\big|_{x=L_x} = 0$. The Hall conductivity can be determined from the charge transport rate,

$$\partial_t Q = \sigma_H\, L_y\, \partial_t \Phi^x, \quad \text{or} \quad \sigma_H = \frac{1}{L_y}\frac{\mathrm{d}Q}{\mathrm{d}\Phi^x}. \tag{2.15}$$

The stress tensor (momentum current) is related to the strain rate in the same way that charge current is related to the flux rate, so a similar procedure can be used to calculate the Hall viscosity.

2.3 Momentum transport

Now let us consider the closely-related problem of momentum transport in the quantum Hall effect. To begin, let us explicitly define our terms with respect to the metric and strain tensors. Suppose there is a coframe field $\bar{\mathrm{e}}^a$ giving the metric

$$g_{\mu\nu} = \delta_{ab}\, \bar{\mathrm{e}}^a{}_\mu\, \bar{\mathrm{e}}^b{}_\nu. \tag{2.16}$$

There is a corresponding frame field denoted e_a such that $\bar{\mathrm{e}}^a(\mathrm{e}_b) = \delta^a_b$. We assume that the spatial connection $\omega^a{}_{bc}$ is flat. The electromagnetic field strength $ieF_{ab}/\hbar$ is the curvature of the electromagnetic gauge connection $ieA_a/\hbar$. The metric varies under the strain tensor $w_{\mu\nu}$ as

$$g \to (g_{\mu\nu} + 2w_{\mu\nu})\, \mathrm{d}x^\mu\, \mathrm{d}x^\nu. \tag{2.17}$$

Assuming uniform strain and an underlying Cartesian (x, y) coordinate system yields three equations for the components of the strain tensor in terms of the local frame,

$$g_{xx} + 2w_{xx} = \left(\bar{\mathrm{e}}^1{}_x\right)^2 + \left(\bar{\mathrm{e}}^2{}_x\right)^2 \tag{2.18a}$$
$$g_{yy} + 2w_{yy} = \left(\bar{\mathrm{e}}^1{}_y\right)^2 + \left(\bar{\mathrm{e}}^2{}_y\right)^2 \tag{2.18b}$$
$$g_{xy} + 2w_{xy} = \bar{\mathrm{e}}^1{}_x\, \bar{\mathrm{e}}^1{}_y + \bar{\mathrm{e}}^2{}_x\, \bar{\mathrm{e}}^2{}_y. \tag{2.18c}$$

The first two equations describe circles in the $\bar{\mathrm{e}}^1{}_x$–$\bar{\mathrm{e}}^2{}_x$ plane and the $\bar{\mathrm{e}}^1{}_y$–$\bar{\mathrm{e}}^2{}_y$ plane, respectively, so it is illustrative to parameterize the coframe fields as:

$$\bar{\mathrm{e}}^1 = \mathrm{d}x\, r_x \cos\phi_x - \mathrm{d}y\, r_y \sin\phi_y \tag{2.19a}$$
$$\bar{\mathrm{e}}^2 = \mathrm{d}x\, r_x \sin\phi_x + \mathrm{d}y\, r_y \cos\phi_y \tag{2.19b}$$

Under this parameterization, the strain tensor equations above are reduced to

$$g_{xx} + 2w_{xx} = r_x^2 \tag{2.20a}$$
$$g_{yy} + 2w_{yy} = r_y^2 \tag{2.20b}$$
$$g_{xy} + 2w_{xy} = r_x r_y \sin(\phi_x - \phi_y). \tag{2.20c}$$

Under strain, the area scales as

$$\sqrt{\det g} = r_x r_y \cos(\phi_x - \phi_y), \tag{2.21}$$

the area of the parallelogram with sides e_x and e_y in the e_1–e_2 plane. The last two equations encode the fact that a uniform rigid rotation of the frame

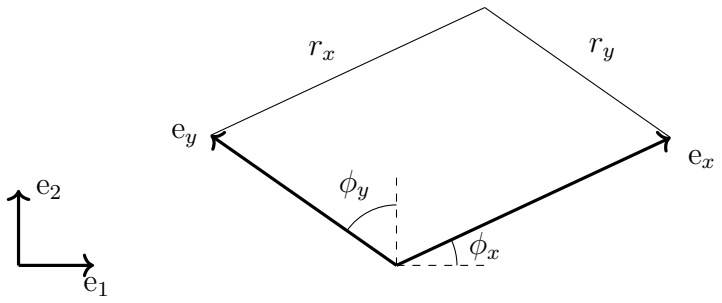

Figure 2.1: The x–y (strained) and u–v (lab) coordinate systems.

field, i.e., shifting ϕ_x and ϕ_y together, induces no strain. For reference, the frame fields are

$$\sqrt{\det g}\,\mathrm{e}_1 = r_y \cos\phi_y \partial_x - r_x \sin\phi_x \partial_y \tag{2.22a}$$
$$\sqrt{\det g}\,\mathrm{e}_2 = r_y \sin\phi_y \partial_x + r_x \cos\phi_x \partial_y \tag{2.22b}$$

The coframe fields inspire us to define an orthogonal coordinate system

$$u = x\, r_x \cos\phi_x - y\, r_y \sin\phi_y \tag{2.23a}$$
$$v = x\, r_x \sin\phi_x + y\, r_y \cos\phi_y \tag{2.23b}$$

so that $\mathrm{d}u = \bar{\mathrm{e}}^1$ and $\mathrm{d}v = \bar{\mathrm{e}}^2$ (and likewise $\partial_u = \mathrm{e}_1$ and $\partial_v = \mathrm{e}_2$).

The structure of the Hall viscosity tensor implies that strain under changing $\phi_x - \phi_y$ leads to momentum transport parallel to the direction of momentum (T^{11} and T^{22}) while changing r_x and r_y leads to momentum transport perpendicular to the momentum direction (T^{12}). A convenient parameterization for shear strain (area-preserving deformations) is to set

$$r_y \;= r_x^{-1} = \alpha \tag{2.24a}$$
$$\phi_x \;= \phi_y = 0 \tag{2.24b}$$

so that

$$-\dot{w}_{11} \;= \dot{w}_{22} = \frac{\dot{\alpha}}{\alpha} \tag{2.25a}$$
$$\dot{w}_{12} \;= \dot{w}_{21} = 0. \tag{2.25b}$$

The Hall viscosity gives rise to stress tensor components odd under time reversal,

$$T^{12}_{(\mathrm{odd})} \;= T^{21}_{(\mathrm{odd})} = 2\eta_H \frac{\dot{\alpha}}{\alpha} \tag{2.26}$$

When the system is anisotropic ($\alpha \neq 1$), we can have $\eta_H^{1122} \neq 0$. Unfortunately, that term cannot be extracted from the momentum transport calculation because it does not appear in the relevant component of the stress tensor, but it also does not affect our calculation of the other viscosity coefficients.

By analogy to the case of charge transport considered in Section 2.2, we calculate the momentum transported into the right half of a cylindrical system as it is deformed. We take the cylinder to have length L and circumference $2\pi R$; the length and circumference vary because the cylinder is under strain; it is helpful to define the cylinder's strained dimensions $L = \alpha^{-1} L_0$ and $R = \alpha R_0$ in terms of its original dimensions L_0 and R_0. If $\mathcal{P}_R$ is the projection operator onto the right half-cylinder, then the total momentum in that half is

$$\langle \Pi_y \mathcal{P}_R \rangle = \int_0^L \mathrm{d}u \int_0^{2\pi R} \mathrm{d}v \; \Pi_y(u, v) \tag{2.27}$$

where $\Pi_y = P_y + eA_y$ is the canonical momentum density. The stress tensor gives the momentum flux across the cut [3, 40], i.e.,

$$\partial_t \Pi_y + \partial_a T^a{}_y = 0. \tag{2.28}$$

Using the continuity equation, and assuming that the momentum flux T^{12} vanishes at $u = L$,

$$\partial_t \langle \Pi_y \mathcal{P}_R \rangle_{(\mathrm{odd})} = \int_0^{2\pi R} \mathrm{d}v \; \bar{\mathrm{e}}^b{}_y T^1{}_b \big|_{u=0} = 4\pi R \, \eta_H \dot{\alpha}. \tag{2.29}$$

where we have used periodicity in the v-coordinate to eliminate a term $\partial_v T^2{}_2$ and evaluated the integral using translation invariance, assuming the ground state is uniform. From this equation we can immediately read-off the important result:

$$\eta_H = \frac{1}{4\pi R} \frac{1}{\dot{\alpha}} \partial_t \langle \Pi_y \mathcal{P}_R \rangle_{(\mathrm{odd})} = \frac{1}{2\pi R_0} \frac{\mathrm{d}}{\mathrm{d}\alpha^2} \langle \Pi_y \mathcal{P}_R \rangle_{(\mathrm{odd})}. \tag{2.30}$$

We use this relationship between η_H and the strain-dependence of the half-cylinder momentum to calculate the viscosity. The subscript (odd) indicates that we have antisymmetrized the term under $B \to -B$, i.e.,

$$2\langle \Pi_y \mathcal{P}_R \rangle_{(\mathrm{odd})} = \langle \Pi_y \mathcal{P}_R \rangle|_B - \langle \Pi_y \mathcal{P}_R \rangle|_{-B}, \tag{2.31}$$

although we make liberal use of the fact that $\langle \Pi_y \mathcal{P}_R \rangle|_B = -\langle \Pi_y \mathcal{P}_R \rangle|_{-B}$ for the systems considered here.

2.4 Landau levels

2.4.1 Hamiltonian and wavefunctions

Let us begin with the conventional Landau level problem of electrons moving in two-dimensions through a uniform transverse magnetic field, including the

possibility of geometric deformations similar to Ref. [7]. The Hamiltonian of such a system is

$$H = \frac{1}{2m}\left(\Pi_1^2 + \Pi_2^2\right). \tag{2.32}$$

Π_a is the canonical momentum given by $-i\hbar\nabla_a$ where ∇_a is the spatially- and gauge-covariant derivative. As is conventional, we define the lowering operator

$$\hat{a} = \frac{1}{\sqrt{2\hbar e F_{12}}}\left[\Pi_1 - i\Pi_2\right] \tag{2.33}$$

and its conjugate, $\hat{a}^\dagger$. It is easy to verify that $\hat{a}$ and its conjugate are the ladder operators of a harmonic oscillator,

$$\left[\hat{a}, \hat{a}^\dagger\right] = \frac{-\hbar}{2eF_{12}}[\nabla_1 - i\nabla_2, \nabla_1 + i\nabla_2] = \frac{-i\hbar}{eF_{12}}[\nabla_1, \nabla_2] = 1. \tag{2.34}$$

The field strength $F_{12} = B$ (i.e., the transverse magnetic field) arises because it is the curvature $[\nabla_1, \nabla_2]$ of the gauge connection. Although the spatial curvature is set to zero here, it would have entered the calculation in the same way as the gauge curvature; this explains the approach of Schine et al. [112] to treat spatial curvature as a modification to the local magnetic field. The Hamiltonian is revealed to be the harmonic oscillator,

$$H = \hbar\omega\left(\hat{a}^\dagger\hat{a} + \frac{1}{2}\right) \tag{2.35}$$

where $\omega = eB/m$ is the cyclotron frequency. The harmonic oscillator takes discrete energy values which are termed Landau levels for this problem. The Landau level wavefunctions $\phi_{(n)}$ are generated by

$$\hat{a}\,\phi_{(0)} = 0 \tag{2.36a}$$
$$\hat{a}^\dagger\,\phi_{(n-1)} = \sqrt{n}\,\phi_{(n)}. \tag{2.36b}$$

The Landau level wavefunctions are given by Avron, Seiler, and Zograf [7] and Lévay [73] under arbitrary strain on a torus (periodic in x and y coordinates). To make connection with more recent iDMRG work [92, 142], and to aid analogy to Hall conductivity, we work with wavefunctions on a cylinder periodic in the v-coordinate with infinite extent in the u-coordinate. The lowest Landau level wavefunction is the null vector of the harmonic oscillator lowering operator $\hat{a}$; in u–v coordinates, this condition is

$$0 = \frac{1}{\sqrt{2\hbar e F_{12}}}[\Pi_1 - i\Pi_2]\phi_{(0)} \tag{2.37}$$

under the boundary conditions

$$\phi_n(u,v) = \phi_n(u, v + 2\pi R) \tag{2.38a}$$
$$\lim_{u \to \pm\infty} \phi_n(u,v) = 0. \tag{2.38b}$$

We impose periodicity in the v-coordinate instead of the y-coordinate because the application of uniform strain with periodicity in y leads to an unnatural twisted boundary condition. To proceed further, we must choose an electromagnetic gauge; the periodic boundary condition suggests the Landau gauge, $A = B\,u\,\mathrm{d}v$. In this gauge, the lowest Landau level wavefunction satisfies

$$0 = \frac{1}{\sqrt{2\hbar eB}}[-i\hbar\,\partial_1 - (\hbar\,\partial_2 - i\,eB\,u)]\phi_0 \tag{2.39}$$

or

$$\phi_0(k;\,u,v) = \frac{\exp\left[ikv - \frac{1}{2}\left(\ell_B^{-1}u + \ell_B k\right)^2\right]}{\sqrt{2\pi R\,\ell_B\sqrt{\pi}}} \tag{2.40}$$

where $\ell_B^2 = \hbar/eB$ and $k = n/R$ for $n \in \mathbb{Z}$. The strain dependence of the wavefunction enters through the radius of the cylinder $R = \alpha R_0$, where R_0 is the undeformed radius of the cylinder. The raising operator $\hat{a}^\dagger$ generates the higher Landau level wavefunctions from ϕ_0; the general formula for the wavefunctions of the n-th Landau level is

$$\phi_n(k;\,u,v) = \frac{\exp\left[ikv - \frac{1}{2}\left(\ell_B^{-1}u + \ell_B k\right)^2\right]}{\sqrt{2^{(n+1)}n!\,\pi^{3/2}R\,\ell_B}} H_n\left(\ell_B^{-1}u + \ell_B k\right), \tag{2.41}$$

where H_n is the n-th Hermite polynomial.

2.4.2 Hall viscosity

To obtain a Hall viscosity formula for the n-th Landau level, we expand Eq. (2.30) in terms of the single-particle eigenstates,

$$\eta_H^{(n)} = \frac{1}{2\pi R_0}\frac{\mathrm{d}}{\mathrm{d}\alpha^2}\left[\sum_k \hbar\alpha k\langle\mathcal{P}_R\rangle_{(n,k)}\right] + \frac{eB}{2\pi R_0}\frac{\mathrm{d}}{\mathrm{d}\alpha^2}\left[\sum_k \alpha\langle u\mathcal{P}_R\rangle_{(n,k)}\right]. \tag{2.42}$$

n indexes Landau levels and $\sum_k$ is the sum over occupied states by wavenumber k. The second term above vanishes here, in the limit $L \to \infty$, but in Section 2.6 we consider how it gives rise to an edge dipole moment in finite systems; in either case, it does not contribute to momentum transport.

Using Eq. (2.42), it is straightforward to calculate the Hall viscosity for a system of Landau levels by the momentum transport method. At filling factor ν, we need only compute the derivative of

$$\langle P_y \mathcal{P}_R \rangle = \sum_{n=0}^{\nu-1} \sum_{k=-K}^{K} \hbar \alpha k \, C_n(k) \tag{2.43a}$$

$$\text{where } C_n(k) = \int_0^\infty \mathrm{d}u \int_0^{2\pi R} \mathrm{d}v \; |\phi_n(k;\, u, v)|^2 \,. \tag{2.43b}$$

with respect to α, cf. Eq. (2.30). We note two things:

1. $C_n(k)$ is the probability of finding a particle on the right ($u > 0$) half of the cylinder, given that the particle is in the state $\phi_n(k)$, and

2. these quantities match the correlation-function eigenvalues $C_n(k)$ if one calculates the entanglement spectrum of this system by cutting the cylinder at $u = 0$.

Thus the projections $C_n(k)$ of the Landau level wavefunctions onto the right half-cylinder are also used to evaluate the momentum polarization. We list their analytic forms here for the first three Landau levels:

$$C_0(k) = \frac{1}{2} \operatorname{erfc}(k\ell_B) \tag{2.44a}$$

$$C_1(k) = k\ell_B \frac{1}{\sqrt{\pi}} e^{-(k\ell_B)^2} + \frac{1}{2} \operatorname{erfc}(k\ell_B) \tag{2.44b}$$

$$C_2(k) = \left[(k\ell_B)^3 + \frac{1}{2} k\ell_B \right] \frac{1}{\sqrt{\pi}} e^{-(k\ell_B)^2} + \frac{1}{2} \operatorname{erfc}(k\ell_B) \tag{2.44c}$$

The strain dependence of the projections $C_n(k)$ is not manifest; recall that the quantization of k depends on α. The half-cylinder projections were also computed by Rodríguez and Sierra [106]. The Landau level wavefunctions are localized in u, so we expect Eq. (2.43a) to converge for sufficiently large, but finite K, although we should ostensibly take $K \to \infty$. The last filled states are centered at $u = \pm K\ell_B^2$; we find that the viscosity derived from the sum over k converges to its expected continuum value when $K > \sqrt{2\pi}\ell_B^{-1}$, i.e., when each half of the cylinder is wider than a single wavefunction. We show the result of the viscosity calculation when successively filling up to the first three Landau levels in Fig. 2.2. We see that the Hall viscosity contribution from each Landau level converges to the established result [73]

$$\eta_H^{(n)} = \frac{\hbar}{8\pi\ell_B^2}(2n+1), \tag{2.45}$$

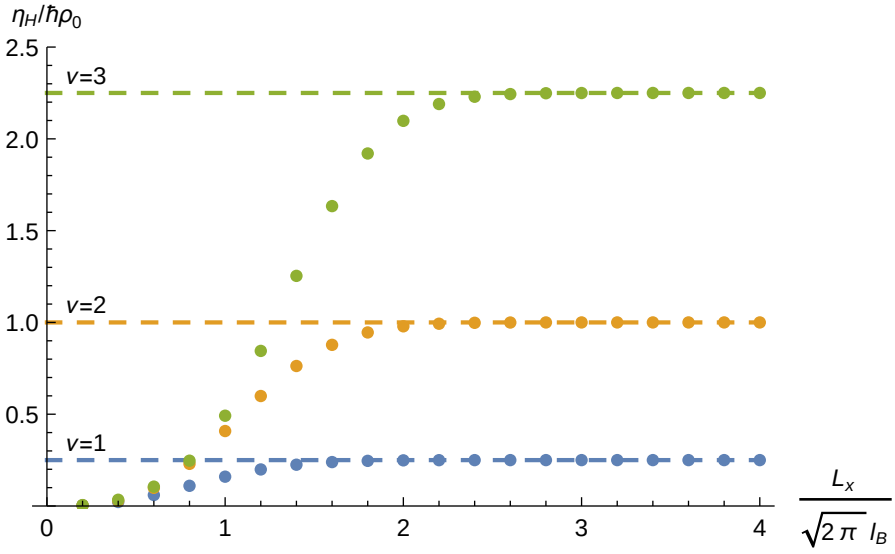

Figure 2.2: The Hall viscosity (η_H) of the lowest Landau levels calculated by the momentum transport method. The calculation converges when $L_x > 2\sqrt{2\pi}\ell_B$, i.e., when each half of the cylinder is wider than a single wavefunction. The Hall viscosity is given in units of $\hbar\rho_0$ where $\rho_0 = 1/2\pi\ell_B^2$ is the electron density of the lowest Landau level. From: Thomas I. Tuegel and Taylor L. Hughes. "Hall viscosity and momentum transport in lattice and continuum models of the integer quantum Hall effect in strong magnetic fields". Phys. Rev. B **92**, 165127 (2015). DOI: 10.1103/PhysRevB.92.165127.

which is the Hall viscosity contribution of the n-th Landau level.

2.4.3 Thermodynamic limit

The result above is also obtained analytically in the thermodynamic limit. Beginning from Eq. (2.30),

$$\eta_H^{(n)} = \frac{1}{2\pi R_0}\frac{\mathrm{d}}{\mathrm{d}\alpha^2}\langle \Pi_y \mathcal{P}_R\rangle_{(n)}. \tag{2.46}$$

we proceed by calculating

$$\frac{1}{2\pi R_0}\langle \Pi_y \mathcal{P}_R\rangle_{(n)} = \frac{\alpha}{2\pi R_0}\frac{\hbar}{\ell_B}\sum_k \int_0^\infty \mathrm{d}u \int_0^{2\pi R} \mathrm{d}v \left(\ell_B k + \ell_B^{-1} u\right) |\phi_n(k;\, u, v)|^2 \tag{2.47}$$

where the Landau level wavefunctions are given by Eq. (2.41). Next define $\xi = \ell_B^{-1} u + \ell_B k$ so that

$$\frac{1}{2\pi R_0}\langle \Pi_y \mathcal{P}_R \rangle_{(n)} = \frac{\alpha}{2\pi R_0}\frac{\hbar}{\ell_B^2}\sum_k \int_0^\infty \mathrm{d}u \, \frac{\xi e^{-\xi^2}}{2^n n!\sqrt{\pi}} H_n(\xi)^2. \tag{2.48}$$

The limit $R_0 \to \infty$ to converts the sum over k to an integral in the thermodynamic limit,

$$\frac{1}{2\pi R_0}\langle \Pi_y \mathcal{P}_R \rangle_{(n)} = \frac{\hbar\alpha^2}{2\pi\ell_B^2}\int_{-\infty}^\infty \mathrm{d}k \int_0^\infty \mathrm{d}u \, \frac{\xi e^{-\xi^2}}{2^n n!\sqrt{\pi}} H_n(\xi)^2. \tag{2.49}$$

This is the expression differentiated in Eq. (2.30) to determine the viscosity.

At this point, one might naively think to carry out the integration over ξ by making a change of variable, but ξ is the sum of two potentially diverging quantities; we must take great care with the limits of integration because x assumes only positive values, while k covers the entire real line. If the lower bound on the x integral were $-\infty$, we could be somewhat careless about the order of limits, but we must take the limits simultaneously,

$$\frac{1}{2\pi R_0}\langle \Pi_y \mathcal{P}_R \rangle_{(n)} = \lim_{K\to\infty} \frac{\hbar\alpha^2}{2\pi\ell_B^2}\int_{-K}^K \mathrm{d}k \int_0^{K\ell_B^2} \mathrm{d}u \, \frac{\xi e^{-\xi^2}}{2^n n!\sqrt{\pi}} H_n(\xi)^2. \tag{2.50}$$

Now we are free to carry out the integrals in either order; beginning with the integral over k,

$$\int_{-K}^K \mathrm{d}k \, \frac{\xi e^{-\xi^2}}{2^n n!\sqrt{\pi}} H_n(\xi)^2 = \frac{1}{2^n n!\sqrt{\pi}\ell_B}\int_{U-\Xi}^{U+\Xi} \mathrm{d}\xi \; \xi e^{-\xi^2} H_n(\xi)^2 \tag{2.51}$$

where $\Xi = \ell_B K$ and $U = \ell_B^{-1} u$. We denote as $I_n(U)$ the integral

$$I_n(U) = \int_{U-\Xi}^{U+\Xi} \mathrm{d}\xi \; \xi e^{-\xi^2} H_n(\xi)^2. \tag{2.52}$$

Integrating by parts obtains

$$I_n(U) = \frac{1}{2}\left[e^{-\xi^2} H_n(\xi)^2\right]\Big|_{U+\Xi}^{U-\Xi} + G_n(U) \tag{2.53}$$

where

$$G_n(U) = 2n\int_{U-\Xi}^{U+\Xi} \mathrm{d}\xi \; e^{-\xi^2} H_n(\xi) H_{n-1}(\xi). \tag{2.54}$$

In this step we have used the derivative of the Hermite polynomial,

$$\partial_\xi H_n(\xi) = 2n H_{n-1}(\xi). \tag{2.55}$$

We evaluate $G_n(U)$ by developing a recursion relation: First, we use the recursion relation for the Hermite polynomials,

$$H_{n+1}(\xi) = 2\xi H_n(\xi) - 2nH_{n-1}(\xi), \tag{2.56}$$

to reduce the order of the $H_n(\xi)$ term:

$$\begin{aligned} G_n(U) &= 4n\, I_1^{(n-1)}(U) - 2n\, G_{n-1}(U) \\ &= 2n\, \left[e^{-\xi^2} H_{n-1}(\xi)^2\right]\Big|_{U+\Xi}^{U-\Xi} + 2n\, G_{n-1}(U). \end{aligned} \tag{2.57}$$

With this recursion relation in mind, and noting that $G_0(U) = 0$, we rewrite the recursion relation as an explicit sum:

$$G_n(U) = \sum_{m=1}^{n} \frac{2^m n!}{(n-m)!}\, \left[e^{-\xi^2} H_{n-m}(\xi)^2\right]\Big|_{U+\Xi}^{U-\Xi}. \tag{2.58}$$

At this point we have a complete expression for $I_1(U)$, which can be written

$$I_n(U) = F_n(U-\Xi) - F_n(U+\Xi) \tag{2.59}$$

where we have defined

$$F_n(\xi) = \frac{1}{2} e^{-\xi^2} H_n(\xi)^2 + \sum_{m=1}^{n} \frac{2^m n!}{(n-m)!} e^{-\xi^2} H_{n-m}(\xi)^2. \tag{2.60}$$

We return to our expression for the projected momentum, which now reads

$$\frac{1}{2\pi R_0} \langle \Pi_y \mathcal{P}_R \rangle_{(n)} = \lim_{K\to\infty} \frac{\hbar\alpha^2}{2\pi\ell_B^2} \int_0^{K\ell_B^2} \mathrm{d}u\ \frac{I_n(U)}{2^n n!\,\sqrt{\pi}\ell_B}. \tag{2.61}$$

Changing variables gives

$$\frac{1}{2\pi R_0} \langle \Pi_y \mathcal{P}_R \rangle_{(n)} = \lim_{K\to\infty} \frac{\hbar\alpha^2}{2\pi\ell_B^2} \int_0^{K\ell_B} \mathrm{d}U\ \frac{I_n(U)}{2^n n!\,\sqrt{\pi}} \tag{2.62}$$

The integral can be expanded in terms of F_n:

$$\int_0^{K\ell_B} \mathrm{d}U\ I_n(U) = \int_0^{K\ell_B} \mathrm{d}U\ F_n(U-\Xi) - F_n(U+\Xi). \tag{2.63}$$

Making separate changes of variable $Y = U - \Xi$ and $Z = U + \Xi$ gives

$$\int_0^{K\ell_B} \mathrm{d}U\ I_n(X) = \int_{-K\ell_B}^{0} \mathrm{d}Y\ F_n(Y) - \int_{K\ell_B}^{2K\ell_B} \mathrm{d}Z\ F_n(Z). \tag{2.64}$$

The bounds of both integrals may be expanded simultaneously to give

$$\int_0^{K\ell_B} \mathrm{d}U\ I_n(U) = \int_{-K\ell_B}^{K\ell_B} \mathrm{d}Y\ F_n(Y) - \int_0^{2K\ell_B} \mathrm{d}Z\ F_n(Z). \tag{2.65}$$

The function F_n is even, so the latter term may be written

$$\int_0^{2K\ell_B} \mathrm{d}Z\ F_n(Z) = \frac{1}{2}\int_{-2K\ell_B}^{2K\ell_B} \mathrm{d}Z\ F_n(Z). \tag{2.66}$$

Now it becomes obvious that both integrals are equal in the $K \to \infty$ limit, so that

$$\lim_{K\to\infty} \int_0^{K\ell_B} \mathrm{d}U\ I_n(U) = \frac{1}{2}\int_{-\infty}^{\infty} \mathrm{d}Y\ F_n(Y). \tag{2.67}$$

If we had not taken care with the order of limits in the beginning, we would not have obtained this result here.

Returning to the expression for the projected momentum,

$$\frac{1}{2\pi R_0}\langle \Pi_y \mathcal{P}_R \rangle_{(n)} = \frac{\hbar\alpha^2}{4\pi\ell_B^2}\int_{-\infty}^{\infty} \mathrm{d}Y\ \frac{F_n(Y)}{2^n n!\sqrt{\pi}} \tag{2.68}$$

where

$$\int_{-\infty}^{\infty} \mathrm{d}Y\ \frac{F_n(Y)}{2^n n!\sqrt{\pi}} = \frac{1}{2}(2n+1). \tag{2.69}$$

The projected momentum is

$$\frac{1}{2\pi R_0}\langle \Pi_y \mathcal{P}_R \rangle_{(n)} = \frac{\hbar\alpha^2}{8\pi\ell_B^2}(2n+1). \tag{2.70}$$

Finally, from Eq. (2.30), we obtain the Hall viscosity of the nth Landau level,

$$\eta_H^{(n)} = \frac{\hbar}{8\pi\ell_B^2}(2n+1), \tag{2.71}$$

in agreement with previous results [7, 73, 104, 105].

2.5 Dirac–Landau levels

2.5.1 Hamiltonian and wavefunctions

The quantum Hall effect was originally understood in the context of electron motion obeying the Schrödinger equation, i.e., a quadratic dispersion relation. As the Schrödinger equation is the spin-polarized, non-relativistic limit of the Dirac equation for electrons, it is not surprising that the latter

also exhibits quantized Landau levels under a magnetic field. This quantum Hall effect in linearly-dispersing electrons became fundamentally important with the rise of graphene [18], and more recently has become relevant in the study of 3D topological insulators with low-energy surface fermions of Dirac nature [47]. The Landau level problem is described by the massive Dirac Hamiltonian under strain,

$$H = v_F \sigma^1 \Pi_1 + v_F \sigma^2 \Pi_2 + m\sigma^3 \tag{2.72}$$

where v_F is the Fermi velocity, m is the mass, and σ^a are the Pauli matrices,

$$\sigma^1 = \begin{pmatrix} 0 & 1 \\ 1 & 0 \end{pmatrix}, \quad \sigma^2 = \begin{pmatrix} 0 & -i \\ i & 0 \end{pmatrix}, \text{ and } \quad \sigma^3 = \begin{pmatrix} 1 & 0 \\ 0 & -1 \end{pmatrix}. \tag{2.73}$$

The Hamiltonian can be reformulated in terms of the harmonic oscillator ladder operators (2.33),

$$H = \begin{pmatrix} m & v_F\sqrt{2\hbar\, eB}\,\hat{a} \\ v_F\sqrt{2\hbar\, eB}\,\hat{a}^\dagger & -m \end{pmatrix} \tag{2.74}$$

so that the Dirac–Landau level wavefunctions are

$$\psi_0(k) = \begin{pmatrix} 0 \\ \phi_0(k) \end{pmatrix} \tag{2.75a}$$

$$\psi_{\pm n}(k) = \frac{1}{\sqrt{n + p_{\pm n}^2}} \begin{pmatrix} p_{\pm n}\,\phi_n(k) \\ \sqrt{n}\,\phi_{n+1}(k) \end{pmatrix} \tag{2.75b}$$

where ϕ_n are the Landau level wavefunctions (2.41); for convenience, we define $p_{\pm n} = \gamma \pm \sqrt{\gamma^2 + n}$ where $\gamma = m/v_F\sqrt{2\hbar\, eB}$ is the ratio of (mass and magnetic) energy scales in the problem. The energy eigenvalues are

$$E_{(0)} = -\gamma v_F \sqrt{2\hbar\, eB} = -m \tag{2.76a}$$

$$E_{(\pm n)} = \pm v_F \sqrt{2\hbar\, eB}\,\sqrt{\gamma^2 + n}. \tag{2.76b}$$

2.5.2 Hall viscosity

Now that we have the Landau level wavefunctions, we can calculate the viscosity using Eq. (2.30), i.e., by differentiating

$$\langle P_y \mathcal{P}_R \rangle = \sum_{k=-K}^{K} \hbar\alpha k \begin{cases} C_0(k) & n = 0 \\ \big(nC_n(k) + p_{\pm n}(\gamma)^2 C_{n-1}(k)\big)\big(n + p_{\pm n}(\gamma)^2\big)^{-1} & n > 0. \end{cases} \tag{2.77}$$

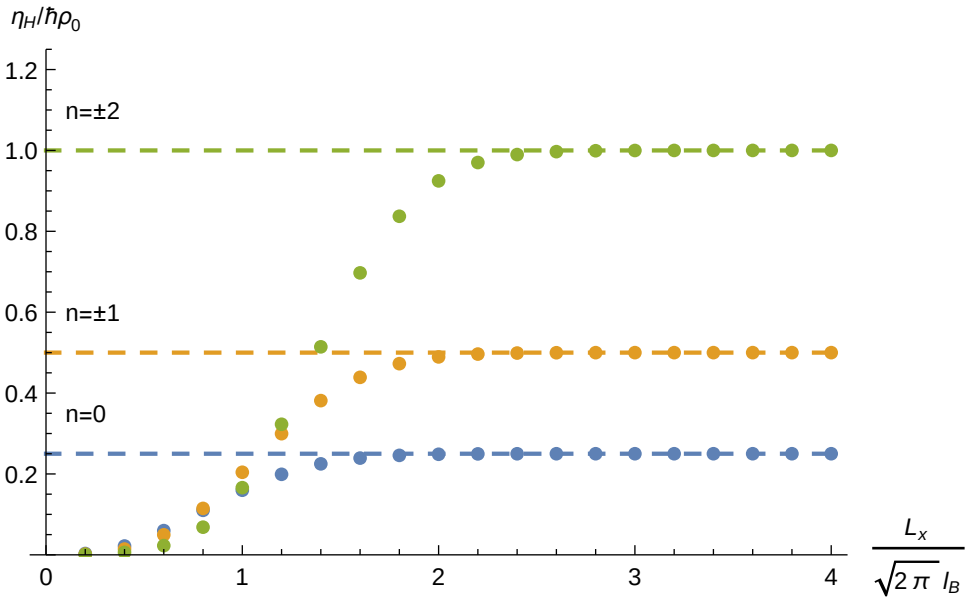

Figure 2.3: The Hall viscosity (η_H) of the lowest Dirac–Landau levels calculated by the momentum transport method. As in Figure 2.2, the calculation converges when $L_x > 2\sqrt{2\pi}\ell_B$. The derivatives in Eq. (2.30) were taken numerically with $\langle p_y \mathcal{P}_R \rangle$ given by Eq. (2.77). The Hall viscosity is given in units of $\hbar\rho_0$ where $\rho_0 = 1/2\pi\ell_B^2$ is the electron density of the lowest Landau level. From: Thomas I. Tuegel and Taylor L. Hughes. "Hall viscosity and momentum transport in lattice and continuum models of the integer quantum Hall effect in strong magnetic fields". Phys. Rev. B **92**, 165127 (2015). DOI: 10.1103/PhysRevB.92.165127.

Recall that $C_n(k)$ is defined in Eq. (2.43a), and matches our earlier results since the Dirac–Landau levels are constructed from the Schrödinger Landau levels.

The connection between the Dirac and Schrödinger Landau-levels leads us to conclude that the Hall viscosity of each Dirac–Landau level is

$$\eta_{H,D}^{(n)} = \begin{cases} \eta_{H,S}^{(0)} & n = 0 \\ \\ \left(n\eta_{H,S}^{(n)} + p_{\pm n}(\gamma)^2 \eta_{H,S}^{(n-1)} \right) / \left(n + p_{\pm n}(\gamma)^2 \right) & n \neq 0 \end{cases} \tag{2.78}$$

where $\eta_{H,S}^{(n)}$ is the Hall viscosity (2.45) of the nth Landau level of the continuum Schrödinger equation. In the massless limit, when $m = \gamma = 0$ so that

$p_{\pm n} = \pm\sqrt{n}$, we find

$$\eta_{H,D}^{(n)} = \begin{cases} \hbar/(8\pi\ell_B^2) & n = 0 \\ \hbar\,|n|\,/(4\pi\ell_B^2) & n \neq 0. \end{cases} \tag{2.79}$$

This result is in agreement with previous work by Kimura [62] based on an adiabatic curvature calculation, except in the case $n = 0$, for which we have found a value twice as large. We attribute the difference to a probable error in the normalization of the zeroth Landau level in Ref. [62]. We confirm the results numerically in Fig. 2.3 using the momentum transport method of calculating the Hall viscosity. Because the Hall viscosity of the Dirac–Landau levels is expressed in terms of the Hall viscosity of the Schrödinger–Landau levels, the convergence criterion is expected to be the same. Indeed, we find the result converges to the expected value when $L_x > 2\sqrt{2\pi}\ell_B$. The same result is obtained by the momentum polarization method, with similar convergence criteria, though we do not show the figure here.

Let us now test if the Dirac calculation reproduces the Schrödinger result in the large mass ($\gamma \to \pm\infty$) limit:

$$p_{+n}(\gamma) \approx 2\gamma + \frac{n}{2\gamma^2} \tag{2.80a}$$

$$p_{-n}(\gamma) \approx \frac{n}{2\gamma^2} \tag{2.80b}$$

and the resulting wavefunctions are

$$\psi_{+n}(k) \approx \begin{pmatrix} 0 \\ \phi_{n+1}(k) \end{pmatrix} \tag{2.81a}$$

$$\psi_{-n}(k) \approx \begin{pmatrix} \phi_n(k) \\ 0 \end{pmatrix}. \tag{2.81b}$$

The limiting values of the wavefunctions can easily be determined by considering the order, with respect to γ, of each component of the spinors. Additionally, the ψ_0 wavefunction is completely unmodified in this limit. From this result we can conclude immediately that, in the infinite mass limit, the Dirac Landau levels carry the same set of values of the viscosity as Schrödinger Landau levels, though we still need to see how they are organized. Additionally, in this limit the energy eigenvalues are

$$E_0 = -m \tag{2.82a}$$

$$E_{\pm n} \approx \pm\sqrt{2\hbar eB}\left(\gamma + \frac{n}{2\gamma}\right) = \pm|E_0| \pm \hbar\omega n \tag{2.82b}$$

with $\omega = |eB/m|$ the usual cyclotron frequency. The spectrum has a gap of width $2|E_0|$ with Landau levels above and below separated from neighboring Landau levels by a gaps of uniform width $\hbar\omega$, much like the Schrödinger spectrum.

The conclusions so far hold generically in the $\gamma \to \pm\infty$ limits. Let us now consider each limit independently, and furthermore, let us consider taking each limit by fixing B and sending $m \to \pm\infty$, respectively. In either case, the wavefunction of the $n = 0$ Landau level is essentially unchanged from the Schrödinger system. When $m \to \infty$, the $n = 0$ Landau level sits at the top of the valence ($E < 0$) band, separated from the $n > 0$ Landau levels by the (large) mass gap. On the other hand, when $m \to -\infty$, the $n = 0$ band sits at the bottom of the conduction ($E > 0$) band with only the cyclotron gap separating it from the $n > 0$ states. It is this configuration, when $m \to -\infty$, and with the $E < 0$ states filled, which more precisely matches the Schrödinger case. This should not be surprising; the $m\sigma^z$ term of the Hamiltonian attaches a positive mass to the $n = 0$ Landau level when $m < 0$. Thus, we see that the massive Dirac case matches the Schrodinger case if one focuses on the positive energy levels when $m \to -\infty$.

2.6 Edge dipole moment

Until now, we have considered infinite cylindrical systems. Our argument that the Hall viscosity can be calculated by measuring the momentum flow across a cut relies mainly on the fact that, while momentum flows into the right half at $u = 0$, it does not flow out again. Therefore, we expect our argument to apply equally well to finite systems since we are measuring the momentum transport deep inside the bulk. However, we know from Haldane [45] that systems with non-zero Hall viscosity support a dipole moment at an edges. We show that the dipole moment complicates the calculation in a finite system and how the complications is resolved.

Following Haldane [45], there is a dipole moment at the edge of a quantum Hall system originating from electrostatic equilibrium: the electric force on the dipole moment is required to balance the pressure (from the Hall viscosity response) at the edge. The dipole moment is

$$dp^a = -\Delta Q^{ab}\epsilon_{bc}dL^c \tag{2.83}$$

where p^a is the anomalous particle number dipole moment, dL^c is the length element along the edge, and Q^{ab} is a symmetric tensor related to the viscosity:

$$\eta^{a\ c}_{\ b\ d} = \frac{\hbar}{2\ell_B^2}\epsilon_{be}\epsilon_{df}\left(\epsilon^{ac}Q^{ef} + \epsilon^{af}Q^{ec} + \epsilon^{ec}Q^{af} + \epsilon^{ef}Q^{ac}\right). \tag{2.84}$$

From this relation, it is straightforward to calculate

$$Q^{gh} = \frac{\ell_B^2}{\hbar}\epsilon_{ac}\epsilon^{gb}\epsilon^{hd}\eta^{a\ c}_{\ b\ d}. \tag{2.85}$$

Using the strain configuration described in Eq. (2.24) this gives

$$Q^{12} = Q^{21} = 0 \tag{2.86a}$$

$$Q^{11} = Q^{22} = \frac{\ell_B^2}{\hbar}\eta_H \tag{2.86b}$$

Hence, a semi-infinite cylindrical system with radius R and an edge on the right has a dipole moment

$$p^1 = \frac{\ell_B^2}{\hbar}2\pi R\Delta\eta_H \tag{2.87}$$

where $\Delta\eta_H$ is the change in Hall viscosity across the edge.

The preceding argument also applies to the finite cylinder by noting that the electrostatic equilibrium condition at the edge applies equally well to both edges. Now consider the right half of the finite cylinder. There is no force applied at its left boundary, i.e., at the center of the entire cylinder, deep in the bulk, because the pressure vanishes inside a Hall fluid [45]. At the right edge there is a dipole moment

$$p^1 = \int_0^{2\pi R} \mathrm{d}v \int_0^{\infty} \mathrm{d}u\ (\rho - \rho_0)(u - u_R) = 2\pi R\frac{\ell_B^2}{\hbar}\Delta\eta_H \tag{2.88}$$

where u_R is the location of the right edge, and ρ_0 is the uniform, neutralizing background charge density. Total charge neutrality requires that

$$u_R\int_0^{\infty} \mathrm{d}x\ (\rho - \rho_0) = 0 \tag{2.89}$$

so we may express the dipole moment independently of choice of origin:

$$p^x = \int_0^{2\pi R} \mathrm{d}v \int_0^{\infty} \mathrm{d}u\ (\rho - \rho_0)\,\alpha u. \tag{2.90}$$

For a discrete system with open boundaries this becomes

$$p^x = \sum_{u>0}\sum_{n,k}\left(|\phi_n(k;\,u)|^2 - \rho_0\right)\alpha u \tag{2.91}$$

with the neutrality requirement that

$$\sum_{u>0}\sum_{n,k}\left(|\phi_n(k;\,u)|^2-\rho_0\right)=0. \tag{2.92}$$

Noting that ρ_0 is independent of α, the derivative of the dipole moment is

$$\frac{\mathrm{d}p^x}{\mathrm{d}\alpha^2}=\frac{\mathrm{d}}{\mathrm{d}\alpha^2}\left[\sum_k \alpha\langle u\mathcal{P}_R\rangle_{(n,k)}\right] \tag{2.93}$$

which exactly matches the second term of Eq. (2.42) to yield

$$\eta_H^{(n)}=\frac{1}{2\pi R_0}\frac{\mathrm{d}}{\mathrm{d}\alpha^2}\left[\sum_k \hbar\alpha k\langle\mathcal{P}_R\rangle_{(n,k)}\right]+\frac{eB}{2\pi R_0}\frac{\mathrm{d}p^x}{\mathrm{d}\alpha^2} \tag{2.94}$$

for a finite system. We see now that the second term of Eq. (2.42) captures an edge effect due to the boundary dipole. While the dipole moment is ultimately due to the viscosity, it does not contribute to bulk transport. Indeed, infinite systems lack the edge to support a dipole moment, yet there is bulk momentum transport which is fully captured by the first term. Therefore, we may safely disregard the edge dipole moment term if we compute the viscosity from $\langle P_y\mathcal{P}_R\rangle$ rather than $\langle\Pi_y\mathcal{P}_R\rangle$.

2.7 Summary

In Chapter 2 we introduced Hall viscosity, a non-dissipative geometric response of time-reversal symmetry breaking fluids, particularly the Landau levels of the quantum Hall effect. The Hall viscosity coefficient describes momentum transport in analogy to the Hall conductivity for charge transport. Based on this correspondence, we described a procedure to transport momentum along a cylindrical system in the same way that charge is transported in the classic "flux-threading" argument. We showed that this procedure can be used to infer the Hall viscosity coefficient from momentum transport, in agreement with established results, for Landau levels and Dirac–Landau levels. Finally, we showed that Hall viscosity leads to a dipole moment at an open boundary, but this term may be safely neglected when computing bulk transport. The ability to neglect edge effects is important in Chapter 3 where we consider finite lattice models of the quantum Hall effect.

Chapter 3

Lattice Models of the Quantum Hall Effect

3.1 Introduction

Chapter 2 introduced a method—based on directly calculating momentum transport—to determine the Hall viscosity which is readily adapted to discrete, lattice systems in magnetic fields. Lattice systems have discrete translation and rotation symmetries, and have an additional length scale a, the lattice constant. Without continuous rotation symmetry, the viscosity is not quantized in terms of the density [104]. Continuous translation symmetry is broken by the lattice so that momentum is not well-defined, but with discrete translation symmetry, we can consider quasi-momentum transport instead. Despite these fundamental differences between lattice and continuum systems, the lattice results converge to the continuum limit as the magnetic length becomes much longer than the lattice length scale (as the magnetic field weakens).

3.2 Continuum limit

Our purpose is to consider the lattice models equivalent to the continuum models studied in Sections 2.4 and 2.5; therefore, we should ensure that our implementation of strain on the lattice is compatible with that limit. We might imagine applying strain to a lattice system by displacing the lattice sites. However, the effective metric of the continuum system is not set by the lattice length scale alone, but also through the effective mass by the hopping

The material presented in Chapter 3 was previously published in: Thomas I. Tuegel and Taylor L. Hughes. "Hall viscosity and momentum transport in lattice and continuum models of the integer quantum Hall effect in strong magnetic fields". Phys. Rev. B **92**, 165127 (2015). DOI: 10.1103/PhysRevB.92.165127. Some figures are reprinted with minor modifications. Some text and figure captions have been modified.

potential, computed as an overlap of atomic wavefunctions in neighboring potential wells [81]. Distorting the lattice could alter the hopping potential, so we see no reason to believe *a priori* that distorting the lattice would leave the effective mass unchanged. Therefore, we keep the lattice vectors fixed and approach the implementation of strain in a more abstract way, while ensuring that the dispersion of the lattice tight-binding model tends to the continuum limit. The dispersion of the two-dimensional tight-binding model is

$$\epsilon(\mathbf{k}) = -2t_1 \cos(\mathbf{k}\cdot\mathbf{a}_1) - 2t_2 \cos(\mathbf{k}\cdot\mathbf{a}_2) \tag{3.1}$$

where t_1 and t_2 are the hopping potentials along the lattice vectors $\mathbf{a}_1$ and $\mathbf{a}_2$ respectively. In the continuum limit, $\mathbf{k}\cdot\mathbf{a}_i \ll 1$, expansion to lowest order in $\mathbf{k}$ gives

$$\epsilon(\mathbf{k}) = -2(t_1 + t_2) + t_1(k_1 a_1)^2 + t_2(k_2 a_2)^2. \tag{3.2}$$

To keep compatibility in the continuum limit, we should ensure that this expansion matches the quadratic dispersion of free electrons in the continuum model,

$$\epsilon(\mathbf{k}) = \frac{\hbar^2}{2m} g^{ab} k_a k_b = \frac{\hbar^2}{2m}\left(g^{11}k_1^2 + g^{22}k_2^2\right) \tag{3.3}$$

where g^{ij} is the inverse effective metric; neglecting the constant offset of the lattice model,

$$t_i = \frac{\hbar^2}{2m}\frac{g^{ii}}{a_i^2}. \tag{3.4}$$

Implementing strain by allowing t_i to vary under the effective metric *without* deforming the lattice is compatible with the continuum limit, although the strain is disconnected from an interpretation based on deformation of the underlying lattice. We consider the disconnect an appropriate compromise, however, because the relation between the continuum-limit strain and the lattice deformation depends strongly on the physical details of the system [115]. We remark that the prescription (3.4) also avoids other difficulties related to distorting the lattice which are discussed in Ref. [115], such as the need to define a distortion periodic across the Brillouin zone or the definition of a new conserved momentum-like quantity (the quantum numbers $\mathbf{k}\cdot\mathbf{a}_i$ already being necessarily conserved under adiabatic evolution).

3.3 Models

3.3.1 Hofstadter–Landau levels

The Landau level problem treated in Section 2.4 is the continuum limit of a tight-binding model due to Hofstadter [50]. The model is a square lattice ($a_x = a_y = a$) tight-binding model on a cylinder with rational flux $\phi = p/q$ per plaquette,

$$H = \sum_{n,k} -t_1 c^\dagger_{n+1,k} c_{n,k} - t_2 \cos(ka - 2\pi\phi n) c^\dagger_{n,k} c_{n,k} + \text{h.c.} \tag{3.5}$$

where $c_{n,k}$ annihilates an electron in the with y-wavenumber k on the n-th site in the x-direction. In the Landau gauge as above, the Hofstadter model does not retain the fundamental lattice translation symmetry in the x direction, but it is symmetric under translation by a whole magnetic cell (q unit cells). On a torus, this symmetry is respected by keeping the size an integer number of magnetic cells, i.e., $N_x = lq$ for integer l. To preserve the symmetry on a cylinder, consider cutting the torus by setting the wavefunction to zero on all the sites at on x coordinate; the cylinder has the same number of unit cells as the torus, lq, but it has one fewer site, $N_x = lq - 1$ [48]. The magnetic translation symmetry affects not only the construction of the lattice, but also the correct scaling of the viscosity (by the lowest Landau level density). With these *commensurate* boundary conditions on a cylinder, the Hofstadter Hamiltonian (3.5) has q nearly flat bands (Hofstadter–Landau levels) consisting of $l - 1$ states at each momentum k. In the gaps between bands are edge states (one mode per gap per k) which connect the bands. For example, the spectrum with open boundary conditions at $q = 20$ is shown in Fig. 3.1.

Now let us explicitly detail how the momentum transport is calculated. Under the strain parameterization (2.24) and the prescription (3.4) for lattice models, we have $t_1 \propto \alpha^2$ and $t_2 \propto \alpha^{-2}$. Therefore, under uniform strain, the Hofstadter Hamiltonian becomes

$$H = \sum_{n,k} -t_1 \alpha^2 c^\dagger_{n+1,k} c_{n,k} - \frac{t_2}{\alpha^2} \cos(ka - 2\pi\phi n) c^\dagger_{n,k} c_{n,k} + \text{h.c.} \tag{3.6}$$

The projected quasi-momentum is

$$\langle p_y \mathcal{P}_R \rangle = \sum_k \sum_{m=1}^{\nu l} \hbar k \langle m, k | \mathcal{P}_R | m, k \rangle \tag{3.7}$$

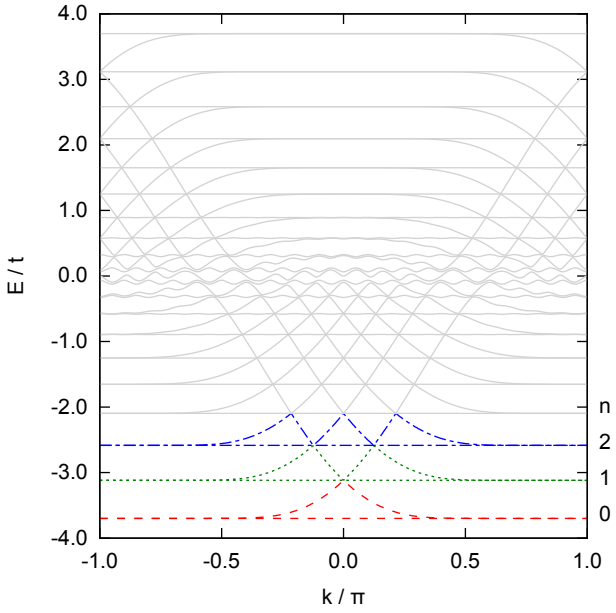

Figure 3.1: The spectrum of the Hofstadter Hamiltonian in Equation (3.6) with $q = 20$. The three lowest Landau levels are highlighted to illustrate the level filling scheme. From: Thomas I. Tuegel and Taylor L. Hughes. "Hall viscosity and momentum transport in lattice and continuum models of the integer quantum Hall effect in strong magnetic fields". Phys. Rev. B **92**, 165127 (2015). DOI: 10.1103/PhysRevB.92.165127.

where $\mathcal{P}_R$ projects onto the right half of the cylinder:

$$\mathcal{P}_R = \sum_{n=0}^{\frac{1}{2}N_x} |n\rangle\langle n|. \tag{3.8}$$

The integers m run over energy eigenstates at a given k from 1 (lowest energy) to a value depending on the filling. If $\nu > q/2$, then the edge states associated with each Landau level above the middle of the spectrum are actually below the flat Landau level, rather than above, so we must take care choosing which states are filled if the viscosity of those Landau levels is of interest. The filling scheme for the first few Landau levels is illustrated in Fig. 3.1. Finally, note that we have omitted the eA_y term in the momentum, i.e., we have computed $\langle p_y \mathcal{P}_R \rangle$ and not $\langle \Pi_y \mathcal{P}_R \rangle$. As explained in Section 2.6, the omitted term captures only unimportant edge effects. Although the Hall viscosity is responsible for these edge effects, they are not related to the *bulk* momentum transport, and so we do not include them in our calculation of the Hall viscosity.

The viscosity can be computed directly from the eigenstates of the Hamiltonian (3.6) using Eqs. (2.30) and (3.7). At large q, the magnetic field is weak, and the magnetic length is much larger than the lattice spacing. In this regime we expect that the Hall viscosity should approach the continuum model. In fact, as in Fig. 3.2, we see that it does converge to the continuum result for the fillings we tested. Biswas [12] also found convergence to the continuum result in the weak-field limit in Hofstadter–Landau levels by a different methodology. As one increases the magnetic field, the effects of the lattice become more prominent. Figure 3.2 also indicates that lattice effects more strongly affect higher Landau levels because the convergence to the continuum limit is slower. Eventually, as the magnetic field strengthens, i.e. as $q \to 0$, the viscosity begins to depend on the lattice scale. From our results in the continuum we expect that, when divided by the density, the viscosity should be a constant, independent of ℓ_B. Instead we find, due to lattice effects, that the viscosity has contributions that depend on the magnetic and lattice length scales,

$$\frac{2\pi\ell_B^2}{\hbar}\eta_H^{(1)} \approx 0.2499 + \frac{0.0017}{\sqrt{2\pi}}\frac{a}{\ell_B} + \frac{0.3865}{2\pi}\frac{a^2}{\ell_B^2} \tag{3.9a}$$

$$\frac{2\pi\ell_B^2}{\hbar}\eta_H^{(2)} \approx 1.0042 + \frac{0.1513}{\sqrt{2\pi}}\frac{a}{\ell_B} + \frac{4.3204}{2\pi}\frac{a^2}{\ell_B^2} \tag{3.9b}$$

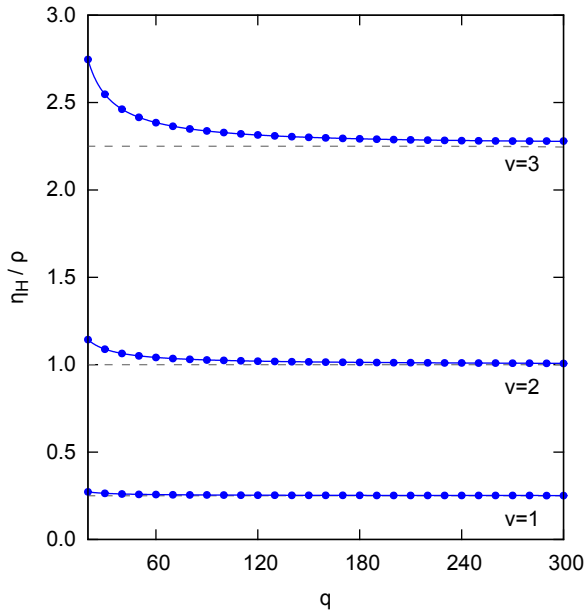

Figure 3.2: The Hall viscosity of the lowest Hofstadter Landau levels calculated by the momentum transport method with $N_y = 51$. The length of the system varies as $N_x = 2q - 1$ to keep commensurate boundaries. The Hall viscosity of the corresponding continuum Landau levels is shown by a dashed line for comparison. From: Thomas I. Tuegel and Taylor L. Hughes. "Hall viscosity and momentum transport in lattice and continuum models of the integer quantum Hall effect in strong magnetic fields". Phys. Rev. B **92**, 165127 (2015). DOI: 10.1103/PhysRevB.92.165127.

$$\frac{2\pi\ell_B^2}{\hbar}\eta_H^{(3)} \approx 2.2289 + \frac{0.5938}{\sqrt{2\pi}}\frac{a}{\ell_B} + \frac{2.2256}{2\pi}\frac{a^2}{\ell_B^2}, \tag{3.9c}$$

where we have rewritten the q dependence in terms of the relevant length scales with $qa^2 = 2\pi\ell_B^2$. We find that each term in the viscosity switches sign under $B \to -B$, as expected.

The Hall viscosity of *anisotropic* ($\alpha \neq 1$) Hofstadter–Landau levels is also readily determined by this method, shown in Figure 3.3. The magnetic field is fixed at values of q large enough ($q = 120, 180$) that the Hall viscosities for the first three Landau levels have (nearly) saturated at the continuum limit. The anisotropic system has only 180°-rotation symmetry and it is quasi-1D for large deviations from $\alpha = 1$. The Hall viscosity of the Hofstadter–Landau levels varies as a function of α itself; in comparison, the viscosity of the continuum Landau level is constant as α is varied. If the system is anisotropic

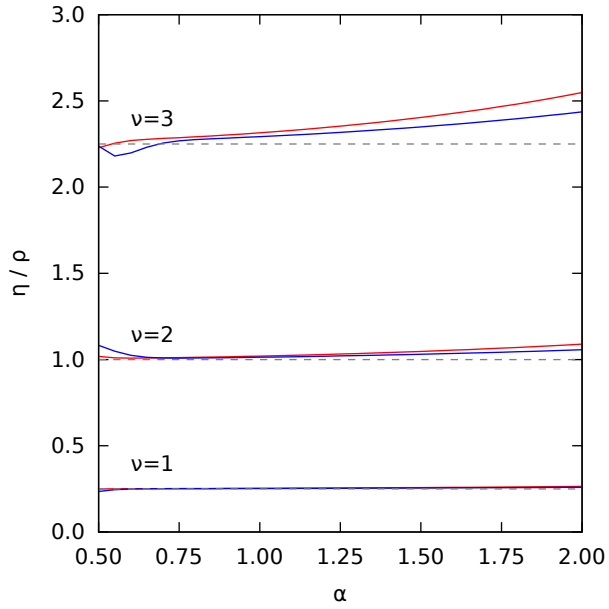

Figure 3.3: The Hall viscosity of the lowest Hofstadter Landau levels is shown at $q = 120$ (red) and $q = 180$ (blue) under anisotropic deformation parameterized by α. For comparison, the Hall viscosity of the corresponding isotropic Landau levels is shown (dashed gray) for filling $\nu \in \{1, 2, 3\}$. The system is isotropic when $\alpha = 1$ and the unit cells are elongated in the y-direction when $\alpha > 1$. From: Thomas I. Tuegel and Taylor L. Hughes. "Hall viscosity and momentum transport in lattice and continuum models of the integer quantum Hall effect in strong magnetic fields". Phys. Rev. B **92**, 165127 (2015). DOI: 10.1103/PhysRevB.92.165127.

we would expect the Hall viscosity to have more than one coefficient, for example $\eta_H^{1112} \neq \eta_H^{1222}$ or $\eta_H^{1122} \neq 0$. The $\alpha \leftrightarrow \alpha^{-1}$ symmetry of the metric under $x \leftrightarrow y$ allows us to determine both viscosity coefficients from the figure by considering α and α^{-1} simultaneously. The third coefficient η_H^{1122} is not expected to enter the momentum transport calculation, and so unfortunately cannot be extracted from the figure. Finally, note that the effect of anisotropy is reduced at larger q because the lattice scale is significantly smaller than the magnetic length, $\ell_B \gg a$.

3.3.2 Lattice Dirac–Landau levels

In Section 3.3.1 we considered a lattice model which has the Landau level problem as its continuum limit. Now let us consider a lattice regularization of the Dirac–Landau level problem from Section 2.5. The lattice Dirac insulator has attracted great interest because of its application to graphene; however, graphene's honeycomb lattice presents extra difficulties—there are multiple Dirac points located away from the Γ-point in the Brillouin zone—so that its continuum limit is not the simple Dirac–Landau level problem. Instead of the honeycomb lattice, we consider a simpler model of a Dirac fermion on a square lattice. As in the square-lattice Hofstadter model, there is rational flux $\phi = p/q$ per unit cell and the system is a cylinder periodic in the y-direction. Under strain parameterization (2.24) and the prescription (3.4), the lattice Dirac Hamiltonian is

$$\begin{aligned} H = \sum_{n,k} \frac{1}{2}\Big[c^\dagger_{n+1,k}\big(i\alpha\sigma^1 - \sigma^3\big)c_{n,k} + \text{h.c.}\Big] + \alpha^{-1}\sin\left(ka - 2\pi\phi n\right)c^\dagger_{n,k}\sigma^2 c_{n,k} \\ + \left[2 - m - \cos\left(ka - 2\pi\phi n\right)\right]c^\dagger_{n,k}\sigma^3 c_{n,k} \end{aligned} \tag{3.10}$$

where $c_{n,k}$ is a two-component annihilation operator. There is a single Dirac cone at $\mathbf{k} = (0,0)$ ($\mathbf{k} = (\pi,\pi)$) when $m = 0$ ($m = 4$). The system dimensions are chosen to preserve magnetic translation symmetry, i.e., the system width is an integer multiple of q, or $N_x = lq - 1$ for integer l, so that the boundaries are commensurate [48]. Figure 3.4 shows the Landau levels at $m = 0$ and $m = 4$. The edge states for $m = 0$ are near $k = 0$, but the edge states for $m = 4$ are near $k = \pi$; this difference affects the calculation of the Hall viscosity below.

The viscosity is calculated by projecting the total momentum onto the right half of the cylinder, as in Eq. (2.30), and differentiating with respect to α. The momentum projection is

$$\langle p_y \mathcal{P}_R\rangle = \sum_k \sum_j^{\text{occ.}} \hbar k \langle j,k|\mathcal{P}_R|j,k\rangle \tag{3.11}$$

where $\mathcal{P}_R$ projects onto the right half of the cylinder:

$$\mathcal{P}_R = \sum_{x=0}^{\frac{1}{2}N_x} \sum_{\sigma=\pm\frac{1}{2}} |x,\sigma\rangle\langle x,\sigma| \tag{3.12}$$

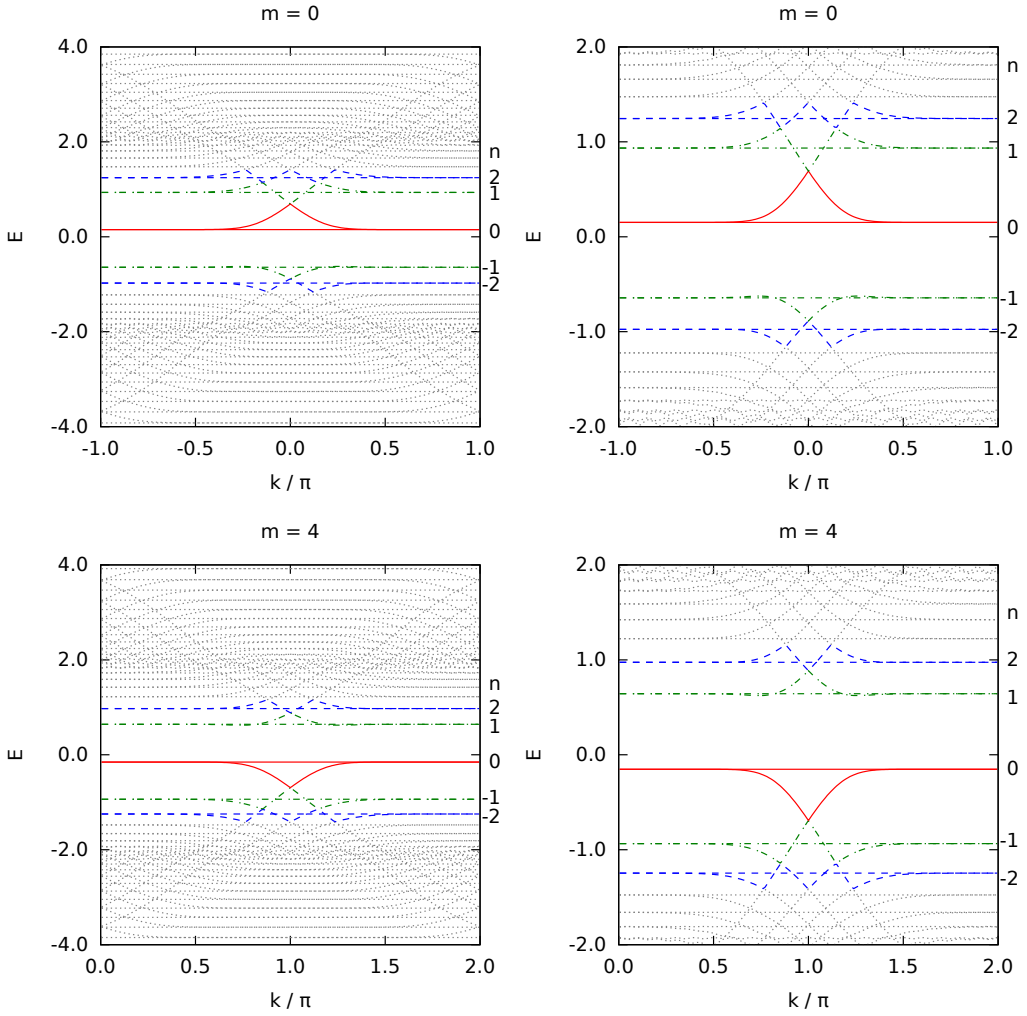

Figure 3.4: The spectrum of the lattice Dirac Hamiltonian in Eq. (3.10) is shown at $m = 0$ (top) and $m = 4$ (below). The $n \in \{0, \pm 1, \pm 2\}$ Dirac Landau levels are indicated. The highlighted Landau levels are enlarged in the panels at right. From: Thomas I. Tuegel and Taylor L. Hughes. "Hall viscosity and momentum transport in lattice and continuum models of the integer quantum Hall effect in strong magnetic fields". Phys. Rev. B **92**, 165127 (2015). DOI: 10.1103/PhysRevB.92.165127.

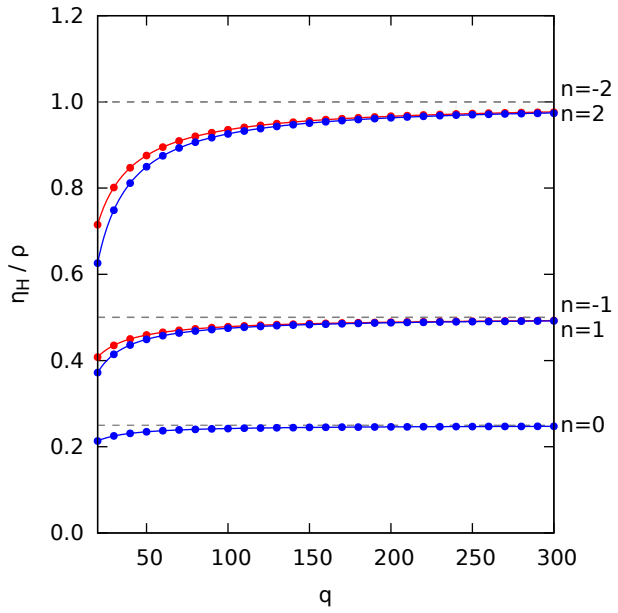

Figure 3.5: The Hall viscosity of the lowest lattice Dirac Landau levels calculated by the momentum transport method. The height of the system is $N_y = 51$ and the width varies as $N_x = 2q - 1$ to keep commensurate boundaries. Only the indicated individual Landau levels are filled. For comparison, the Hall viscosity of the individual continuum Dirac Landau levels is shown by the dotted gray lines. From: Thomas I. Tuegel and Taylor L. Hughes. "Hall viscosity and momentum transport in lattice and continuum models of the integer quantum Hall effect in strong magnetic fields". Phys. Rev. B **92**, 165127 (2015). DOI: 10.1103/PhysRevB.92.165127.

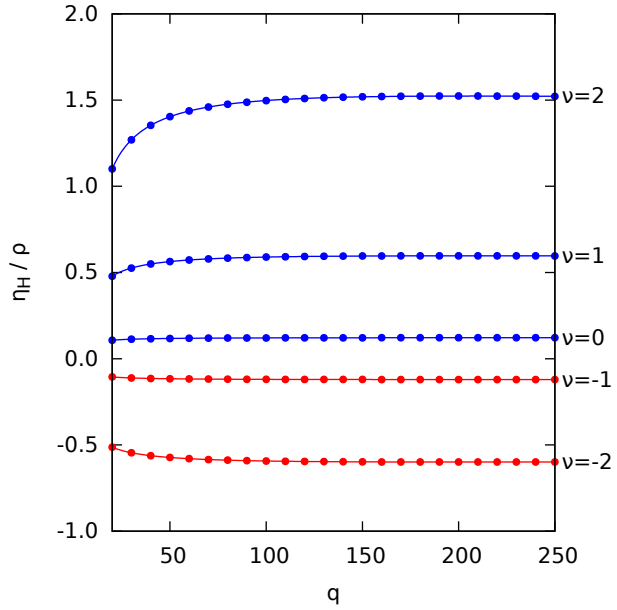

Figure 3.6: The Hall viscosity of the lattice Dirac model is shown with filling through the indicated Landau levels. The height of the system is $N_y = 51$ and the width varies as $N_x = 2q - 1$ to keep commensurate boundaries. The model is filled from the bottom of the lattice Dirac spectrum. When filling from the bottom of the spectrum, the number of filled lattice Dirac Landau levels increases with q (unlike in the ordinary quantum Hall effect); therefore, a linear term $0.011q$ has been subtracted from each series. From: Thomas I. Tuegel and Taylor L. Hughes. "Hall viscosity and momentum transport in lattice and continuum models of the integer quantum Hall effect in strong magnetic fields". Phys. Rev. B **92**, 165127 (2015). DOI: 10.1103/PhysRevB.92.165127.

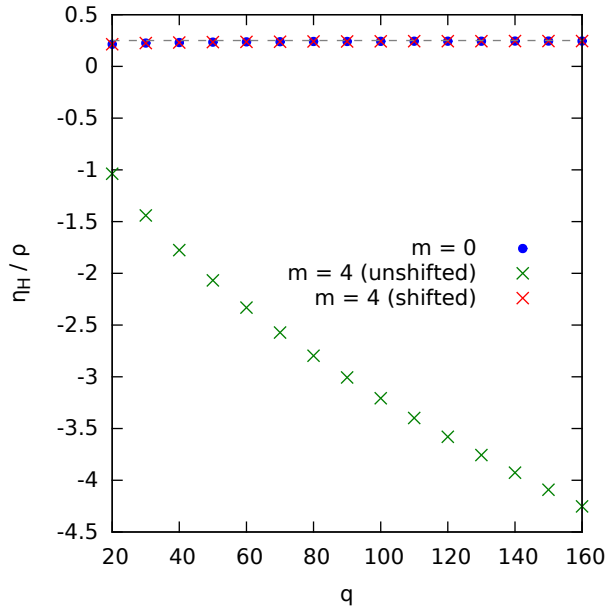

Figure 3.7: The Hall viscosity of the zeroth lattice Dirac Landau level is shown at $m = 0$ (circles) and $m = 4$ (crosses) over a range of q values. The height of system is $N_y = 51$ and the width varies as $N_x = 2q - 1$ to keep commensurate boundaries. The $m = 4$ series is plotted twice; the unshifted plot shows the viscosity when the Brillouin zone is unshifted so that the Dirac point is at $k = \pm\pi$ and the shifted plot shows the viscosity when the Brillouin zone has been shifted so that the Dirac point falls at $k = 0$. From: Thomas I. Tuegel and Taylor L. Hughes. "Hall viscosity and momentum transport in lattice and continuum models of the integer quantum Hall effect in strong magnetic fields". Phys. Rev. B **92**, 165127 (2015). DOI: 10.1103/PhysRevB.92.165127.

The integers j run over the occupied energy eigenstates at a given k_y. For most of the cases we consider we only fill the Landau levels near half-filling. We note that near half-filling the n-th Landau level consists of the states (see Fig. 3.4)

$$N_x + nl < j \leq N_x + (n+1)l, \quad \text{for } m = 0 \tag{3.13a}$$

$$N_x + (n-1)l < j \leq N_x + nl, \quad \text{for } m = 4. \tag{3.13b}$$

Notice that the 0-th Landau level moves from the bottom of the conduction band at $m = 0$ to the top of the valence band at $m = 4$. This is clearly shown in Fig. 3.4.

The Hall viscosity of individual lattice Dirac–Landau levels was calculated

at $m = 0$ by the momentum transport method in Eq. (2.30) to obtain the results in Fig. 3.5. The values here represent the viscosity calculations from individually filling (not successively filling) the $n = 0, \pm 1$, and ± 2 Landau levels (where $n = 0$ is referenced to the zeroth Landau level of the Dirac point, not the bottom of the entire bandwidth). To help illustrate, we have shown which Landau levels were filled in Fig. 3.4. The lattice calculation converges to the continuum value in the large-q (weak magnetic field) limit, i.e. the Hall viscosity of the lattice system approaches the continuum value in the limit where the magnetic length ℓ_B is much larger than the spacing between unit cells. As the magnetic field strength increases, so does the effect of the lattice, with the viscosity taking on q-dependent terms:

$$\frac{2\pi\ell_B^2}{\hbar}\eta_H^{(-2)} \approx 0.9868 + \frac{0.4276}{\sqrt{2\pi}}\frac{a}{\ell_B} + \frac{12.0267}{2\pi}\frac{a^2}{\ell_B^2} \tag{3.14a}$$

$$\frac{2\pi\ell_B^2}{\hbar}\eta_H^{(-1)} \approx 0.5018 + \frac{0.0576}{\sqrt{2\pi}}\frac{a}{\ell_B} + \frac{1.7067}{2\pi}\frac{a^2}{\ell_B^2} \tag{3.14b}$$

$$\frac{2\pi\ell_B^2}{\hbar}\eta_H^{(0)} \approx 0.2498 + \frac{0.0045}{\sqrt{2\pi}}\frac{a}{\ell_B} + \frac{0.8290}{2\pi}\frac{a^2}{\ell_B^2} \tag{3.14c}$$

$$\frac{2\pi\ell_B^2}{\hbar}\eta_H^{(1)} \approx 0.5025 + \frac{0.0857}{\sqrt{2\pi}}\frac{a}{\ell_B} + \frac{1.3075}{2\pi}\frac{a^2}{\ell_B^2} \tag{3.14d}$$

$$\frac{2\pi\ell_B^2}{\hbar}\eta_H^{(2)} \approx 0.9802 + \frac{0.6299}{\sqrt{2\pi}}\frac{a}{\ell_B} + \frac{14.1092}{2\pi}\frac{a^2}{\ell_B^2}, \tag{3.14e}$$

where we have used the relation $qa^2 = 2\pi\ell_B^2$. As predicted by the continuum calculation, the Hall viscosity converges to approximately the same value for positive and negative Landau levels.

Instead of calculating the Hall viscosity of individual Dirac–Landau levels near the Dirac point, let us now consider filling states from the bottom of the spectrum up to a mid-gap Fermi level such as might occur in actual materials; the results are shown in Figure 3.6. It is not clear *a priori* how this should compare to the continuum results because such a filling is not possible in an unregularized continuum Dirac model. In fact, the Hall viscosity scales linearly with q if it is calculated with bands filled from the bottom of the spectrum because increasing q adds extra bands to the bottom of the spectrum that must be filled. The continuum Dirac–Landau model, in contrast, has an constant, infinite number of filled levels below the Fermi level; without a regularization scheme, we cannot sum over an infinite number of negative-energy levels. Obviously the lattice result with a variable number

of filled bands cannot be directly compared to the continuum model, so we have subtracted off a linear term $0.011q$ in Figure 3.6. It is noteworthy that the *difference* in the viscosity between filling $\nu = n$ and $\nu = n + 1$ matches the Hall viscosity of the $(n+1)$-th individual continuum Dirac–Landau level. Although the Hall viscosity may be regularization-dependent, the difference in viscosity across a filled Dirac–Landau level seems to retain a universal character.

The lattice Dirac insulator has massless Dirac points when $m = 0$ and $m = 4$; having already considered the former case, we turn now to the latter. Figure 3.7 compares the Hall viscosity calculated by the momentum transport method at $m = 0$ and $m = 4$. The naive result for the Hall viscosity shows a monotonically decreasing function that does not converge for large q. However, to properly interpret this result, care must be taken to recenter the Brillouin zone. If m is fixed, but $k \to k - \pi$, then the momentum transport calculation *exactly* recovers the result at $m = 0$. When the Brillouin zone is not shifted, the edge states near $k = \pi$ transport extra momentum leading to the discrepancy. Generically, when a low-energy Dirac point is shifted away from $\mathbf{k} = 0$ in the Brillouin zone, there is additional momentum transport due to simply to the Dirac cone.

3.4 Summary

In Chapter 2, we introduced a procedure to compute the Hall viscosity based on momentum transport, applied to continuum models. In Chapter 3, we applied this procedure to compute the Hall viscosity of two lattice models equivalent to each of the continuum models in the previous chapter. We addressed the difficulty applying strain to a lattice model while maintaining equivalence in the continuum limit. In both models, we found convergence to the continuum Hall viscosity in the limit that the magnetic length scale is much longer than the lattice length scale, as expected. In the first case of the Hofstadter model, we also determined that the Hall viscosity coefficient deviates from its continuum value in an anisotropic system, even in the continuum limit. Finally, we addressed two peculiar features of the lattice Dirac–Landau levels: the existence of negative-indexed Landau levels and the distinct phases at $m = 0$ and $m = 4$.

Chapter 4

Hall Viscosity in Helium-3

4.1 Introduction

The primary obstacle to observing Hall viscosity in the quantum Hall effect is the difficulty to probe directly the momentum of the two-dimensional electron gas; however, proposals do exist to measure the Hall viscosity indirectly [2, 17, 52, 55, 87, 129]. In contrast, superfluid ^{3}He−B provides a direct probe of momentum transport: although simple fluids usually support only longitudinal acoustic waves, three-dimensional paired superfluids such as ^{3}He−B support *transverse* acoustic waves. Despite early predictions of transverse acoustic waves in ^{3}He−B [65, 80], and early observation of longitudinal acoustic waves [70, 94], transverse acoustic waves were not described in detail theoretically [86], or observed [71] until much later. In a typical experiment the superfluid resides in a cavity with one wall that acts as a transducer. The collective mode excitations of the superfluid pairs are largely responsible for supporting the propagation of transverse acoustic waves in the superfluid. If the (intrinsically time-reversal invariant) superfluid is placed under a weak magnetic field, the degeneracy of the collective mode excitations is broken due to the Zeeman effect. Since the transverse waves are coupled to the collective modes, the Zeeman effect changes the relative phase velocity of opposite circular polarization components, i.e., it induces circular birefringence. For example, if a linearly-polarized wave is injected into the fluid, then its polarization rotates as it propagates through ^{3}He−B due to the relative phase velocity of each component, a phenomenon known as the acoustic Faraday effect. This effect can be interpreted as arising

The material presented in Chapter 4 was previously published in: Thomas I. Tuegel and Taylor L. Hughes. "Hall viscosity and the acoustic Faraday effect". Phys. Rev. B **96**, 174524 (2017). DOI: 10.1103/PhysRevB.96.174524. Some text has been modified.

directly from the Hall viscosity generated by the application of the magnetic field.

4.2 Helium-3 phenomenology

The superfluid B-phase of ^{3}He is described by the spin-triplet, p-wave pairing Balian–Werthamer state [46, 72, 86]. The order parameter is a 3×3 complex matrix,

$$d_{ij} = \frac{\Delta}{\sqrt{3}} R_{ij}(\hat{\mathbf{n}}, \theta) e^{i\phi} \tag{4.1}$$

parameterized by the self-energy amplitude Δ, the phase ϕ, and the rotation R_{ij} of the spin by an angle θ around an axis $\hat{\mathbf{n}}$ relative to the orbital angular momentum [86]. The ground state and collective mode excitations are eigenstates of the *twisted* total angular momentum operator,

$$\mathbf{J} = \mathbf{L} + R^{-1}\mathbf{S}. \tag{4.2}$$

The states are additionally labeled by their signature under particle-hole symmetry; the real part of d_{ij} transforms with signature $+1$, and the imaginary with signature -1.

The six families of states $J = \{0, 1, 2\}^{\{+,-\}}$ comprise 18 states in all. The $J = 0^-$ and $J = 1^+$ states are the Goldstone modes, coupling to longitudinal zero sound and spin waves respectively [78, 79]. The counterparts of these modes, $J = 0^+$ and $J = 1^-$, are not relevant to this discussion: these branches of modes are at, and beyond, the pair-breaking edge and so they are strongly damped [135]. The real $J = 2^+$ excitations do not couple to transverse waves in the quasi-classical linear response theory, so we do not consider them [46, 82, 135]. It is only the $J = 2^-$ *imaginary squashing* modes that couple to transverse acoustic waves below the pair-breaking frequency, and are primarily responsible for collision-less transverse sound.

4.3 The acoustic Faraday effect

The Faraday effect is the rotation of a linearly-polarized optical wave propagating through a gyrotropic (magneto-optically active) medium: an applied magnetic field breaks time-reversal symmetry, creating optical birefringence between left- and right-hand polarized waves known as *circular birefringence* [66]. Circular birefringence leads to a phase shift between linear

polarization components passing through the medium; that phase shift has the effect of rotating the linear polarization vector around the axis of propagation. The *acoustic* Faraday effect refers to the analogous rotation of linearly-polarized transverse acoustic waves. As in the optical Faraday effect, the rotation of transverse acoustic wave polarization is due to the phase shift induced by circular birefringence. In this section, we review the propagation of acoustic plane waves and show that their circular birefringence is a manifestation of Hall viscosity.

4.3.1 Wave equation

We begin by reviewing wave propagation in isotropic viscoelastic media in three dimensions and go on to include the anisotropic Hall viscosity. Wave propagation is governed by two equations: the continuity equation

$$\partial_t \rho + \partial_a g^a = 0 \tag{4.3}$$

where ρ is the mass density and g^a the momentum density, and the constitutive equation

$$\partial_t g^a + \partial_b T^{ba} = 0 \tag{4.4}$$

where T^{ab} is the stress tensor and $a, b = 1, 2, 3$. Designating the displacement field as u^a, the momentum density is

$$g^a = \rho\, \partial_t u^a. \tag{4.5}$$

Throughout we assume linear displacements and linear density variations. The stress tensor is related to the strain,

$$w_{ab} = \tfrac{1}{2}(\partial_a u_b + \partial_b u_a), \tag{4.6}$$

and the strain rate $\partial_t w_{ab}$, through the elasticity λ^{abcd} and viscosity η^{abcd} tensors:

$$T^{ab} = -\lambda^{abcd} w_{cd} - \eta^{abcd} \partial_t w_{cd}. \tag{4.7}$$

The elasticity and viscosity tensors are each symmetric under exchange of their last two indices due to using the symmetric strain tensor w_{cd}. In an isotropic system, they are conventionally parameterized

$$\lambda^{abcd} = G\big(\delta^{ac}\delta^{bd} + \delta^{ad}\delta^{bc}\big) + \big(K - \tfrac{2}{3}G\big)\delta^{ab}\delta^{cd} \tag{4.8a}$$

$$\eta^{abcd} = H\big(\delta^{ac}\delta^{bd} + \delta^{ad}\delta^{bc}\big) + \big(\Xi - \tfrac{2}{3}H\big)\delta^{ab}\delta^{cd} \tag{4.8b}$$

where G (H) is the shear modulus (viscosity) and K (Ξ) is the bulk modulus (viscosity).

Now let us choose a plane-wave ansatz for an acoustic wave, i.e., let the displacement field be a plane wave with wavevector $\mathbf{q}$ and frequency ω:

$$\mathbf{u}(\mathbf{x}, t) = \mathbf{u}\, e^{i(\mathbf{q}\cdot\mathbf{x}-\omega t)}. \tag{4.9}$$

In three dimensions, we can decompose the polarization vector $\mathbf{u}$ using an oriented triad of real, orthonormal vectors $\{\mathbf{e}_1, \mathbf{e}_2, \mathbf{e}_3\}$ (the linear polarization basis) such that $\mathbf{e}_3$ is chosen to be the direction of propagation: $\mathbf{q} = q\,\mathbf{e}_3$. Under this ansatz, the density may fluctuate linearly around the background density ρ_0,

$$\rho(\mathbf{x}, t) = \rho_0 + \delta\rho\, e^{i(\mathbf{q}\cdot\mathbf{x}-\omega t)}. \tag{4.10}$$

To linear order, the momentum density is independent of the density fluctuations,

$$\mathbf{g}(\mathbf{x}, t) = -i\omega\, \rho_0 \mathbf{u}(\mathbf{x}, t). \tag{4.11}$$

The strain tensor and stress tensor are

$$w_{ab} = \tfrac{i}{2}(q_a u_b + q_b u_a) \tag{4.12a}$$
$$T^{ab} = -i\big(\lambda^{abcd} - i\omega\eta^{abcd}\big) q_c u_d \tag{4.12b}$$

where we have used the symmetry of the elasticity and viscosity tensors in the second equation above. Evaluated under this ansatz, the continuity equation

$$-i\omega\, \delta\rho + q\,\omega\,\rho_0 u^3 = 0 \tag{4.13}$$

determines that the density fluctuations

$$\delta\rho = i\, q\, \rho_0 u^3 \tag{4.14}$$

are proportional to and out-of-phase with the longitudinal displacement; this justifies our assertion in Eq. (4.11) that the linear momentum density is independent of the density fluctuations. The constitutive equation is

$$-\rho\omega^2 u^a + q^2(\lambda^{ac} - i\omega\eta^{ac})u_c = 0, \tag{4.15}$$

where, for brevity, we have designated nine components each of the elasticity and viscosity tensors as

$$\lambda^{3a3c} = \lambda^{ac} \quad \text{and} \quad \eta^{3a3c} = \eta^{ac} \quad \text{where} \quad a, c \in \{1, 2, 3\}. \tag{4.16}$$

Equation (4.15) determines the speed of wave propagation.

4.3.2 Longitudinal waves

Longitudinal waves have displacement along the direction of propagation,

$$u^1 = u^2 = 0 \quad \text{and} \quad u^3 \neq 0. \tag{4.17}$$

According to Eq. (4.10) there are density fluctuations proportional to the displacement field. Using the constitutive equation (4.15) and the isotropic elasticity and viscosity tensors (4.8), we find the speed of longitudinal waves $c_l(\omega)$ in isotropic media is given by

$$c_l(\omega)^2 = \rho_0^{-1}\left[\left(K + \tfrac{4}{3}G\right) - i\omega\left(\Xi + \tfrac{4}{3}H\right)\right]. \tag{4.18}$$

The real part $\operatorname{Re} c_l(\omega)^2$ includes the contribution of the bulk modulus, effectively a restoring force against compression. The imaginary part $\operatorname{Im} c_l(\omega)^2$ is related to the attenuation of longitudinal waves due to dissipative viscosity producing a drag force.

4.3.3 Transverse waves

Transverse waves propagate in an elastic medium because the elasticity provides a restoring force against a strain gradient perpendicular to the direction of propagation (transverse). Displacement is only transverse to the direction of propagation, $u^3 = 0$. Following Eq. (4.10), there are no density fluctuations due to transverse waves and we do not expect the bulk modulus or viscosity to affect the speed of sound. Using the constitutive equation (4.15) and the isotropic elasticity and viscosity tensors (4.8), we find the speed of transverse waves $c_t(\omega)$ in isotropic media is given by

$$c_t(\omega)^2 = \rho_0^{-1}(G - i\omega H). \tag{4.19}$$

As above, the elasticity provides a restoring force against the wave displacement; here only the shear modulus G contributes to $\operatorname{Re} c_t(\omega)^2$. The shear viscosity H is responsible for a drag force leading to the imaginary (attenuating) term $\operatorname{Im} c_t(\omega)^2$.

4.3.4 Hall viscosity

The anti-symmetric part of the viscosity is often neglected because it vanishes in time-reversal invariant systems and isotropic systems in three dimensions [4]. When present, however, the anti-symmetric or Hall viscosity

leads to a force perpendicular to the strain rate gradient. To highlight the relationship between Hall viscosity and angular momentum, we may prefer to think of this as a non-dissipative *torque*. To see this clearly, we work in the circular polarization basis, $\{\mathbf{e}_+, \mathbf{e}_-, \mathbf{e}_3\}$, where

$$\mathbf{e}_\pm = \tfrac{1}{\sqrt{2}}(\mathbf{e}_1 \pm i\mathbf{e}_2). \tag{4.20}$$

This basis has a metric given by

$$g_{++} = g_{--} = \mathbf{e}_+ \cdot \mathbf{e}_+ = \mathbf{e}_- \cdot \mathbf{e}_- = 0 \tag{4.21a}$$
$$g_{+-} = g_{-+} = \mathbf{e}_+ \cdot \mathbf{e}_- = \mathbf{e}_- \cdot \mathbf{e}_+ = 1 \tag{4.21b}$$

so we must take care when raising and lowering indices. The components of a 2-index tensor A in the circular basis are related to the linear basis by

$$A^{++} = (A^{--})^* = \tfrac{1}{2}(A^{11} - A^{22}) - \tfrac{i}{2}(A^{12} + A^{21}) \tag{4.22a}$$
$$A^{+-} = (A^{-+})^* = \tfrac{1}{2}(A^{11} + A^{22}) - \tfrac{i}{2}(A^{12} - A^{21}) \tag{4.22b}$$

where A may be the (reduced) elasticity λ or viscosity η.

To extend our study to include Hall viscosity, we allow anisotropy along the direction of propagation e_3 to remain relevant to experiments in ^{3}He−B where a magnetic field is applied along e_3. Maintaining rotation symmetry in the e_1−e_2 plane preserves the conservation of angular momentum of circularly polarized waves. The A^{++} and A^{--} components of the reduced elasticity and viscosity are required to vanish, as they violate rotation symmetry by coupling right-circular and left-circular polarized waves. We also neglect the dissipative terms $\operatorname{Im}\lambda^{+-}$ and $\operatorname{Re}\eta^{+-}$ because transverse waves in ^{3}He−B only couple to non-dissipative order parameter fluctuations [86]. Including the ordinary shear viscosity through the $\operatorname{Re}\eta^{+-}$ coefficient would introduce a contribution to the constitutive equation out of phase with the other terms, leading to a damped solution instead of an undamped plane wave. The combination of rotation symmetry and exclusion of dissipative effects imposes the constraints

$$\lambda^{12} = \lambda^{21} = 0 \tag{4.23a}$$
$$\eta^{11} = \eta^{22} = 0. \tag{4.23b}$$

The only surviving terms contributing to the speed of sound are the shear modulus,

$$G = \tfrac{1}{2}\big(\lambda^{11} + \lambda^{22}\big) \tag{4.24}$$

and the Hall viscosity,

$$\eta_H = \tfrac{1}{2}\big(\eta^{12} - \eta^{21}\big). \tag{4.25}$$

The speed $c_\pm(\omega)$ of each circular polarization component is given by

$$c_\pm(\omega)^2 = \rho_0^{-1}(G \mp \omega\eta_H). \tag{4.26}$$

Immediately we see that each component has a different phase velocity: the fluid exhibits circular birefringence when $\eta_H \neq 0$, i.e., when time-reversal symmetry is broken. An observation of circular birefringence in transverse acoustic waves would enable the direct determination of the Hall viscosity coefficient. We consider this possibility in the context of ^{3}He−B below.

4.4 Zeeman splitting

Circularly-polarized transverse acoustic waves transform under the $J = 2$ angular momentum representation and carry $m = \pm 1$; therefore, to conserve angular momentum, they may couple only to the subset of the $J = 2^-$ multiplet with $m = \pm 1$ [86]. The dispersion relation for waves with frequency ω and wavevector q is [23, 86]

$$\frac{\omega^2}{v_F^2 q^2} = \Lambda_0 + \Lambda_{(2^-)} \frac{\omega^2}{\omega^2 - \omega_{(2^-)}^2 - \frac{2}{5} v_F^2 q^2}, \tag{4.27}$$

where v_F is the Fermi velocity, Λ_0 is the effective quasiparticle restoring force (which is insensitive to the magnetic field), and $\Lambda_{(2^-)}$ is the coupling to the $J = 2^-$ collective modes. The denominator of the second term depends on the dispersion relation of the imaginary-squashing collective modes,

$$\omega^2 = \omega_{(2^-)}^2 + \tfrac{2}{5} v_F^2 q^2, \tag{4.28}$$

where $\omega_{(2^-)}$ is the frequency edge for the $J = 2^-$ modes. The sensitivity of the transverse acoustic waves to the magnetic field is primarily due to the Zeeman splitting of the $J = 2^-$ collective modes that modifies $\omega_{(2^-)}$. The Zeeman effect may also be thought of as generating a contribution to the Hall viscosity that is responsible for acoustic circular birefringence.

In zero magnetic field, the lowest energy, fully degenerate $J = 2^-$ modes have frequency $\omega_{(2^-)} = \sqrt{\frac{12}{5}}\Delta$. The shear modulus due to the $J = 2^-$ collective modes can be determined using Eq. (4.26),

$$\rho^{-1} G_{(2^-)} = \frac{\Lambda_{(2^-)} v_F^2 \omega^2}{\omega^2 - \frac{12}{5}\Delta^2 - \frac{2}{5} v_F^2 q^2}. \tag{4.29}$$

The quasiparticle contribution to the shear modulus is neglected because it contains only time-reversal invariant contributions; thus it is insensitive to the magnetic field and cannot contribute to the Hall viscosity. In the long-wavelength limit, i.e., near resonance,

$$\lim_{q\to 0}\rho^{-1}G_{(2^-)}=\frac{\Lambda_{(2^-)}v_F^2\omega^2}{\omega^2-\frac{12}{5}\Delta^2}. \tag{4.30}$$

Applying a weak magnetic field along the propagation direction breaks the $J=2^-$ degeneracy by Zeeman splitting:

$$\omega_{(2^-)}=\sqrt{\tfrac{12}{5}}\Delta+m_{(2^-)}g_{(2^-)}\omega_L \tag{4.31}$$

where $g_{(2^-)}$ is the Landé g-factor [114], $m_{(2-)}$ is the angular momentum quantum number along the field direction, and ω_L is the Larmor frequency of the $J=2^-$ modes given by

$$g_{(2^-)}\hbar\omega_L=\gamma B_z, \tag{4.32}$$

and γ is the effective coupling constant of the collective modes to the magnetic field [111]. The dispersion relation (4.27) now differs for each of the $m_{(2^-)}=\pm 1$ components,

$$\frac{\omega^2}{v_F^2q^2}=\Lambda_0+\Lambda_{(2^-)}\frac{\omega^2}{\omega^2-\left[\sqrt{\frac{12}{5}}\Delta\pm g_{(2^-)}\omega_L\right]^2-\frac{2}{5}v_F^2q^2}. \tag{4.33}$$

Consider the limit near resonance in which the magnetic field B is weak enough to justify expansion to linear order in B, i.e.,

$$g_{(2^-)}\omega_L\ll\sqrt{\omega^2-\tfrac{12}{5}\Delta^2}\ll\Delta. \tag{4.34}$$

The Hall viscosity under weak magnetic fields and in the long-wavelength limit is determined by comparison with Eq. (4.26) to find

$$\lim_{q\to 0}\eta_H=-2G_{(2^-)}\frac{g_{(2^-)}\omega_L}{\omega^2-\frac{12}{5}\Delta^2}, \tag{4.35}$$

neglecting terms of order $(\omega^2-\frac{12}{5}\Delta^2)/\omega^2$. This shows explicitly that the Zeeman splitting of the $J=2^-$ collective modes may be interpreted as a direct contribution to the Hall viscosity coefficient and hence affects the transverse acoustic wave propagation.

4.5 Effective model of collective modes

A simple effective model of the low-energy superfluid collective modes as an ensemble of non-interacting bosons suffices to derive a Hall viscosity coefficient in agreement with the circular birefringence result above. The success of this model further supports the interpretation of the acoustic Faraday effect as a Zeeman-induced Hall viscosity.

Consider the collective modes as non-interacting bosons with orbital angular momentum $\hat{\mathbf{L}}$ and spin $\hat{\mathbf{S}}$. The orbital angular momentum represents, roughly, the orbital angular momentum of the quasiparticles making up the superfluid pairs. At the mean field level, the effective interaction—experienced by the quasiparticles as they orbit—is perturbed by the strain on the system; therefore, the orbital angular momentum couples to strain. However, the spin—an internal degree of freedom—is not coupled to the strain in this context. Indeed, the Cooper pair has a spatial extent, so its orbital angular momentum is sensitive to the (effective) spatial metric induced by the strain. Spin, on the other hand, is the intrinsic angular momentum of a point-like particle and insensitive to the effective strain metric.

With this assumption, the dynamics of the collective modes are given by the model Hamiltonian

$$H = H_0(\hat{\mathbf{J}}) + \gamma \mathbf{B} \cdot \hat{\mathbf{J}} + \mu^{-1} w^{mn} \hat{L}_m \hat{L}_n + 2\gamma w^{mn} B_m \hat{L}_n, \tag{4.36}$$

where μ is the effective pair moment of inertia and γ is the effective pair coupling to the magnetic field. The symmetrized strain tensor w_{mn} is defined in Eq. (4.6). The Hamiltonian $H_0(\hat{\mathbf{J}})$ is the zero-field, zero-strain Hamiltonian for the bosons. With $\hat{\mathbf{J}}$ given by Eq. (4.2), and knowing that the low-energy collective modes of ^{3}He−B arise from the $L = S = 1$ pairs, it suffices to take

$$H_0(\hat{\mathbf{J}}) = \sum_{J=0}^{2} \sum_{m=-J}^{J} \hbar\omega_{(J^-)} |J, m\rangle\langle J, m| \tag{4.37}$$

with the well-established spectrum of particle-hole antisymmetric collective modes,

$$\omega_{(0^-)} = 0,\ \omega_{(1^-)} = 2\Delta, \text{ and } \omega_{(2^-)} = \sqrt{\tfrac{12}{5}}\Delta. \tag{4.38}$$

The spectrum could be chosen to model another system by H_0, or to include particle-hole symmetric modes, and it should apply in more general contexts.

The strain susceptibility is given by the Kubo formula [14, 64]

$$\chi^{abmn} = -\frac{i}{\omega}\frac{1}{\sqrt{g}}\left\langle \frac{\delta T^{ab}}{\delta w_{mn}} \right\rangle + \lim_{\epsilon\to 0^+}\frac{1}{\hbar\omega^+}\int_0^\infty \mathrm{d}t\, e^{i\omega^+ t}\left\langle \left[T^{ab}(t), T^{mn}\right]\right\rangle \quad (4.39)$$

where the symmetric stress tensor is

$$T^{ab} = -\frac{1}{\sqrt{g}}\frac{\delta H}{\delta w_{ab}} = \frac{1}{\sqrt{g}}\left(g^{am}g^{bn} + g^{an}g^{bm}\right)\left[\frac{1}{2\mu}\hat{L}_m\hat{L}_n + \gamma B_m\hat{L}_n\right], \quad (4.40)$$

and the effective metric is $g_{mn} = \delta_{mn} + 2w_{mn}$. The stress tensor is independent of H_0 because the latter is insensitive to strain. At zero strain, this yields

$$T^{ab}\big|_{w=0} = -\frac{1}{2\mu}\left(\hat{L}^a\hat{L}^b + \hat{L}^b\hat{L}^a\right) - \gamma\left(B^a\hat{L}^b + B^b\hat{L}^a\right). \quad (4.41)$$

The variational term of the susceptibility at zero strain depends on the expectation value of

$$\frac{1}{\sqrt{g}}\frac{\delta T^{ab}}{\delta w_{mn}}\bigg|_{w=0} = -T^{ab}\delta^{mn} - \left(\delta^{ma}\left[\frac{1}{2\mu}\left(\hat{L}^n\hat{L}^b + \hat{L}^b\hat{L}^n\right) + \gamma(B^n\hat{L}^b + B^b\hat{L}^n)\right] + [m\leftrightarrow n] + [a\leftrightarrow b] + [ma\leftrightarrow nb]\right) \quad (4.42)$$

giving the infinite-frequency (contact) contribution to the transport coefficients; if the zero-field ground state is isotropic in space, then it gives no contribution to η_H. The commutator term gives the finite-frequency contribution; it vanishes unless the orbital angular momentum $L > 0$ and time-reversal symmetry is broken. Evaluation of the commutator term proceeds in the usual way, by inserting a resolution of the identity

$$1 = \sum_{J=0}^{2}\sum_{m=-J}^{J} |J,m\rangle\langle J,m| \quad (4.43)$$

between $T^{ab}(t)$ and T^{mn}. For our effective model of ^{3}He−B collective modes, the shear modulus is

$$\begin{aligned} G_{(2^-)} &= -\tfrac{1}{2}i\omega\left(\chi^{1313} + \chi^{2323}\right) \\ &= \frac{1}{3}\frac{n}{\hbar}\left[\frac{\hbar^2}{2\mu}\right]^2\sqrt{\frac{12}{5}}\frac{\Delta}{\left(\omega^2 - \frac{12}{5}\Delta^2\right)} + \frac{4}{3}\frac{\hbar^2}{2\mu}n, \end{aligned} \quad (4.44)$$

where n is the boson number density. The Hall viscosity coefficient is

$$\begin{aligned}\eta_H &= \tfrac{1}{2}\left(\chi^{1323} - \chi^{2313}\right) \\ &= -\frac{2}{3}\frac{n}{\hbar}\left[\frac{\hbar^2}{2\mu}\right]^2 \sqrt{\frac{12}{5}}\frac{\Delta}{\left(\omega^2 - \frac{12}{5}\Delta^2\right)^2}\frac{\gamma B_z}{\hbar}\end{aligned} \tag{4.45}$$

where $\gamma B_z/\hbar = g_{(2^-)}\omega_L$. Near resonance, i.e., when $\omega^2 - \frac{12}{5}\Delta^2 \ll \Delta^2$, the shear modulus is entirely dominated by its divergent term and the Hall viscosity coefficient generated by Zeeman splitting agrees with the prediction from the previous section,

$$\eta_H = -2G_{(2^-)}\frac{g_{(2^-)}\omega_L}{\omega^2 - \frac{12}{5}\Delta^2}. \tag{4.46}$$

Therefore, the model supports the conclusion that the Zeeman-split collective modes induce the Hall viscosity that is responsible for the acoustic Faraday effect in ^{3}He−B.

4.6 Summary

In Chapter 4 we re-examined the phenomenon of the acoustic Faraday effect in ^{3}He−B. We showed that Hall viscosity generally leads to circular birefringence of transverse acoustic waves, a result we expect to hold in other systems where the effect has been or is expected to be observed. The acoustic Faraday effect is attributed to Zeeman splitting of the ^{3}He−B collective models; we do not question this explanation, rather we demonstrate that Zeeman splitting *leads to* Hall viscosity. We constructed a simple effective model for the collective modes which has as inputs only well-established phenomenological features of ^{3}He−B: the angular momentum state and frequency of the active modes. Coupled to a magnetic field, Zeeman splitting in our simple model leads to Hall viscosity, justifying our claim.

Chapter 5

Entanglement

5.1 Introduction

The central object of entanglement spectrum methods is the *reduced density matrix* [95, 96] constructed by tracing out a subsystem, also referred to as making an *entanglement cut*. If A is a subsystem of S then the reduced density matrix on A is [95]

$$\rho_{\mathsf{A}} = \mathrm{Tr}_{\overline{\mathsf{A}}}\, \rho \tag{5.1}$$

where ρ is the density matrix on S and the trace is carried out over $\overline{\mathsf{A}}$, the complement of A in S. The subsystem A is often taken to be half of the total system, but it proves useful to take other subsystems as well. If $\mathcal{O}_{\mathsf{A}}$ is an operator such that $\operatorname{supp} \mathcal{O}_{\mathsf{A}} \leq \mathsf{A}$, then [95]

$$\langle \mathcal{O}_{\mathsf{A}} \rangle = \mathrm{Tr}_{\mathsf{S}}\, \rho\, \mathcal{O}_{\mathsf{A}} = \mathrm{Tr}_{\mathsf{A}}\, \rho_{\mathsf{A}} \mathcal{O}_{\mathsf{A}}. \tag{5.2}$$

Formally, the reduced density matrix may be written as the thermal density matrix of an *entanglement Hamiltonian* $\mathcal{H}_{\mathsf{A}}$,

$$\rho_{\mathsf{A}} = Z_{\mathsf{A}}^{-1} e^{-\mathcal{H}_{\mathsf{A}}}, \quad \text{where } Z_{\mathsf{A}} = \mathrm{Tr}_{A}\, e^{-\mathcal{H}_{\mathsf{A}}}. \tag{5.3}$$

When the bosonic or fermionic Hamiltonian of the total system is quadratic, the entanglement Hamiltonian is also quadratic [95],

$$\mathcal{H}_{\mathsf{A}} = \sum_i \varepsilon_i a_i^\dagger a_i, \tag{5.4}$$

where the eigenvalues ε_i are called the *entanglement spectrum*. The creation and annihilation operators a_i are given by a unitary transformation Q of the creation and annihilation operators c_i or the original system,

$$a_i = c_j Q_{ji} \quad \text{and} \quad a_i^\dagger = c_j^\dagger \overline{Q_{ji}} \tag{5.5}$$

The unitarity of Q ensures that the a_i obey the same commutation or anti-commutation relation as the c_i operators. The single-particle basis defined by Q forms a convenient basis for computing expectation values on A.

5.2 Entanglement spectrum

5.2.1 Correlation function eigenvalues

Peschel [95] explains that the quadratic entanglement Hamiltonian$\mathcal{H}$ is related to the single-particle correlation function C on the subsystem A. The correlation function is given by

$$C_{ij} = \mathrm{Tr}_A \ \rho_{\mathsf{A}} c_i^\dagger c_j \quad \text{where} \quad i,j \ \in \mathsf{A} \tag{5.6}$$

and c_j is the fermion annihilation operator at j. (The same is applicable to bosons, but hereafter we consider only fermions.) Inverting the relations (5.5) we have

$$C_{ij} = Q_{im}\Big(\mathrm{Tr}_{\mathsf{A}} \ Z_{\mathsf{A}}^{-1} e^{-\mathcal{H}_{\mathsf{A}}} \, a_m^\dagger a_n\Big)\overline{Q}_{nj}. \tag{5.7}$$

The trace is diagonal in the a_i basis, or

$$C_{ij} = \sum_m Q_{im}\overline{Q}_{mj}\Big(\mathrm{Tr}_{\mathsf{A}} \ Z_{\mathsf{A}}^{-1} \, e^{-\mathcal{H}_{\mathsf{A}}} a_m^\dagger a_m\Big) \tag{5.8}$$

with the partition function given by

$$Z_{\mathsf{A}}^{-1} = \mathrm{Tr}_{\mathsf{A}} \, e^{-\mathcal{H}_{\mathsf{A}}} = \prod_i \sum_{\left\langle a_i^\dagger a_i \right\rangle}^{\{0,1\}} e^{-\varepsilon_i} = \prod_i \left(1 + e^{-\varepsilon_i}\right). \tag{5.9}$$

Therefore, the single-particle correlation function shares its eigenfunctions with the quadratic entanglement Hamiltonian $\mathcal{H}_A$,

$$C_{ij} = Q_{im}\left[\frac{1}{e^{\varepsilon_m}+1}\right]\overline{Q}_{mj} \tag{5.10}$$

and the eigenvalues ξ_i of C are [95]

$$\xi_i = \frac{1}{e^{\varepsilon_i}+1}. \tag{5.11}$$

Instead, the entanglement spectrum can be deduced from the spectrum of C,

$$\varepsilon_i = \log\left(\xi_i^{-1} - 1\right) = \log\left(\frac{1-\xi_i}{\xi_i}\right). \tag{5.12}$$

This expression has the obvious utility that it deals with the single-particle correlation function rather than the many-body density matrix.

5.2.2 Correspondence between entanglement spectra

Under an entanglement cut, the density matrix is partitioned into the reduced density matrices ρ_{A} and $\rho_{\overline{\mathsf{A}}}$ and an off-diagonal block ρ_T,

$$\rho = \begin{pmatrix} \rho_{\mathsf{A}} & \overline{\rho_T} \\ \rho_T & \rho_{\overline{\mathsf{A}}} \end{pmatrix}. \tag{5.13}$$

At zero temperature, ρ is a projector, i.e., $\rho^2 = \rho$ giving three conditions on ρ_{A}, $\rho_{\overline{\mathsf{A}}}$, and ρ_T:

$$\overline{\rho_T}\rho_T = (1-\rho_{\mathsf{A}})\rho_{\mathsf{A}} \tag{5.14a}$$
$$\rho_T\,\overline{\rho_T} = (1-\rho_{\overline{\mathsf{A}}})\rho_{\overline{\mathsf{A}}} \tag{5.14b}$$
$$\rho_T = \rho_T\,\rho_{\mathsf{A}} + \rho_{\overline{\mathsf{A}}}\,\rho_T. \tag{5.14c}$$

The reduced density matrices are diagonalized by

$$\rho_{\mathsf{A}} = U_{\mathsf{A}}\,\Lambda_{\mathsf{A}}\,\overline{U_{\mathsf{A}}} \quad \text{where} \quad \Lambda_{\mathsf{A}} = \operatorname{diag}\left(\{\lambda_{\mathsf{A},i}\}\right) \tag{5.15a}$$
$$\rho_{\overline{\mathsf{A}}} = U_{\overline{\mathsf{A}}}\,\Lambda_{\overline{\mathsf{A}}}\,\overline{U_{\overline{\mathsf{A}}}} \quad \text{where} \quad \Lambda_{\overline{\mathsf{A}}} = \operatorname{diag}\left(\{\lambda_{\overline{\mathsf{A}},i}\}\right). \tag{5.15b}$$

The eigenvalues and eigenvectors of the reduced density matrices are related to the singular value decomposition [76] of ρ_T,

$$\rho_T = U_T\,\Sigma_T\,\overline{V_T} \quad \text{where} \quad \Sigma_T = \begin{pmatrix} \operatorname{diag}\left(\{\sigma_{T,i}\}\right) \\ 0 \end{pmatrix} \tag{5.16}$$

where we assume (without loss of generality) that $\dim \rho_{\mathsf{A}} \leq \dim \rho_{\overline{\mathsf{A}}}$. The left (right) singular vectors of ρ_T are the eigenvectors of $\rho_T\,\overline{\rho_T}$ ($\overline{\rho_T}\,\rho_T$) respectively, so that

$$U_T = U_{\overline{\mathsf{A}}} \quad \text{and} \quad V_T = U_{\mathsf{A}}, \tag{5.17}$$

and the singular values are the square-roots of the eigenvalues of the same,

$$\sigma_{T,i} = \sqrt{(1-\lambda_{\mathsf{A},i})\lambda_{\mathsf{A},i}} = \sqrt{(1-\lambda_{\overline{\mathsf{A}},i})\lambda_{\overline{\mathsf{A}},i}}. \tag{5.18}$$

There are at least $(\dim \rho_{\overline{\mathsf{A}}} - \dim \rho_{\mathsf{A}})$ eigenvectors of $\rho_{\overline{\mathsf{A}}}$ with singular value $\sigma_T = 0$ (due to the dimensions of Σ_T) and therefore with $\lambda_{\overline{\mathsf{A}}} \in \{0, 1\}$. Equation (5.14c) shows that ρ_T maps eigenvectors u_{A} of ρ_{A} into eigenvectors of $\rho_{\overline{\mathsf{A}}}$,

$$(1-\lambda_{\mathsf{A}})(\rho_T\,u_{\mathsf{A}}) = \rho_{\overline{\mathsf{A}}}(\rho_T\,u_{\mathsf{A}}) \tag{5.19}$$

which justifies the correspondence between λ_{A} and $\lambda_{\overline{\mathsf{A}}}$ in Eq. (5.18).

5.3 Global symmetries

One motivation to study the reduced density matrix is to understand the topology of the subsystem state in A. Topological invariants are computed as a trace on A, so it is crucial that the global symmetry protecting the state be respected by the reduced density matrix if A is to be in a symmetry-protected topological state. In general, the topological indices of a symmetry-protected topological state are invariant under any cut (real-space or otherwise) which respects the protecting symmetries [56]; as a specific example relevant to our cases, consider a global (on-site) symmetry g of the Hamiltonian,

$$[H, g]_{\pm} = 0 \tag{5.20}$$

where g is either a commuting $[\cdot,\cdot]_+$ or an anti-commuting $[\cdot,\cdot]_-$ symmetry. The topology is defined with respect to the filling of single-particle states at $E < 0$ or the spectral projector P, i.e., the single-particle density matrix. The flat-band Hamiltonian $1 - 2P$ is also symmetric under g,

$$[1 - 2P, g]_{\pm} = 0 \tag{5.21}$$

because g either maps each single-particle eigenstate onto itself (commuting) or onto a partner with the opposite occupancy under P (anti-commuting). Under a partition of the system S into disjoint subsystems A and $\overline{\mathsf{A}}$, the flat-band Hamiltonian can be written as a sum of terms with support on A or $\overline{\mathsf{A}}$, plus a term mapping each subsystem into the other:

$$1 - 2P = (1_{\mathsf{A}} - 2P_{\mathsf{A}}) + (1_{\overline{\mathsf{A}}} - 2P_{\overline{\mathsf{A}}}) - 2P_{\mathsf{A}\overline{\mathsf{A}}} \tag{5.22}$$

If the partition respects g, i.e., it does not cut through any unit cell, then each term is individually symmetric under g:

$$[1_{\mathsf{A}} - 2P_{\mathsf{A}}, g]_{\pm} = 0 \tag{5.23a}$$
$$[1_{\overline{A}} - 2P_{\overline{A}}, g]_{\pm} = 0 \tag{5.23b}$$
$$[P_{\mathsf{A}\overline{\mathsf{A}}}, g]_{\pm} = 0. \tag{5.23c}$$

P_{A} is the reduced density matrix on A; although it generally represents a thermal state, we can flatten $1_{\mathsf{A}} - 2P_{\mathsf{A}}$ into a quantum reduced density matrix (as the Hamiltonian H was flattened) without breaking the global symmetry g. The flattened, reduced density matrix is used to compute topological indices.

5.4 Entropy and mutual information

The relative entropy of two densities ρ_{A} and ρ_{B} is [91]

$$S(\rho_{\mathsf{A}}|\rho_{\mathsf{B}}) = \begin{cases} \operatorname{Tr} \rho_{\mathsf{A}}(\log \rho_{\mathsf{A}} - \log \rho_{\mathsf{B}}) & \text{if } \operatorname{supp} \rho_{\mathsf{A}} \leq \operatorname{supp} \rho_{\mathsf{B}} \\ \infty & \text{otherwise.} \end{cases} \tag{5.24}$$

An important special case is the von Neumann entropy,

$$S(\rho_{\mathsf{A}}) \ = -S(\rho_{\mathsf{A}}|1) = -\operatorname{Tr}_{\mathsf{A}} \rho_{\mathsf{A}} \log \rho_{\mathsf{A}} \tag{5.25}$$

measuring correlation across the boundary of A. The entanglement entropy is readily computed in terms of the single-particle correlation spectrum (5.11),

$$S(\rho_{\mathsf{A}}) = -\sum_i \xi_i \log \xi_i + (1-\xi_i) \log (1-\xi_i). \tag{5.26}$$

Recall that the correlation spectrum takes values $\xi_i \in [0,1]$; states at $\xi_i = 0$ and $\xi_i = 1$ do not contribute to the entanglement entropy, which is dominated by states at $\xi_i = 1/2$. A state at $\xi_i = 1/2$ has equal weight in A and $\overline{\mathsf{A}}$, i.e., it is maximally correlated across the boundary of A. The correspondence in eigenvalues when $\lambda_{\overline{\mathsf{A}}} \notin \{0,1\}$ implies that the regions have the same entanglement entropy $S(\rho_{\mathsf{A}}) = S(\rho_{\overline{\mathsf{A}}})$.

The mutual information of regions A and B is the entropy of their joint state relative to their marginal states, [139]

$$I(\mathsf{A},\mathsf{B}) \ = S(\rho_{\mathsf{AB}}|\rho_{\mathsf{A}} \otimes \rho_{\mathsf{B}}) = S(\rho_{\mathsf{A}}) + S(\rho_{\mathsf{B}}) - S(\rho_{\mathsf{AB}}). \tag{5.27}$$

Whereas the entanglement entropy measures correlation of a region with its complement, the mutual information measures correlation between two disjoint regions. Figure 5.1 explains this interpretation graphically:

- $S(\rho_{\mathsf{A}})$ ($S(\rho_{\mathsf{B}})$) measures the correlation between A and $\overline{\mathsf{A}}$ (B and $\overline{\mathsf{B}}$), and
- $S(\rho_{\mathsf{AB}})$ measures the correlation between $\mathsf{A} \cup \mathsf{B}$ and $\overline{\mathsf{A}} \cap \overline{\mathsf{B}}$, but
- $S(\rho_{\mathsf{AB}})$ does not include any correlations between A and B because

$$\mathsf{A} \cap (\overline{\mathsf{A}} \cap \overline{\mathsf{B}}) \ = \mathsf{B} \cap (\overline{\mathsf{A}} \cap \overline{\mathsf{B}}) = \varnothing, \tag{5.28}$$

  so that

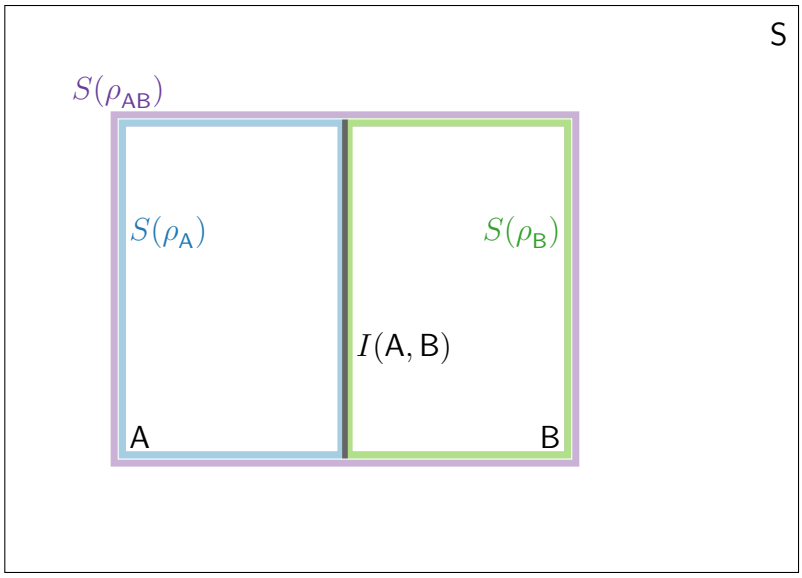

Figure 5.1: Entanglement entropy and mutual information of regions A and B in S. The entanglement entropy $S(\rho_i)$ measures correlation between a region i and its complement. The mutual information $I(i,j)$ measures correlation across the boundary between two regions i and j, discounting common correlations with their shared environment.

- the mutual information is the excess correlation between A and B over the correlations with their common environment.

Equation (5.27) is also valid when A and B are not disjoint, but the interpretation becomes murkier. In practice, we will not be troubled by interpreting the mutual information of overlapping regions; rather, we use the mutual information to measure the degree of hybridization of topologically-protected states in disjoint regions.

The mutual information $I(\mathsf{A}:\mathsf{B})$ bounds correlation functions between regions A and B [139]. The relative entropy gives the mutual information,

$$I(\mathsf{A},\mathsf{B}) = S(\rho_{\mathsf{AB}}|\rho_{\mathsf{A}}\otimes\rho_{\mathsf{B}}) \tag{5.29}$$

which is bounded below by

$$S(\rho|\sigma) \geq \frac{1}{2}\|\rho-\sigma\|^2. \tag{5.30}$$

The mutual information is thus bounded

$$I(\mathsf{A},\mathsf{B}) \geq \frac{1}{2}\|\rho_{\mathsf{AB}}-\rho_{\mathsf{A}}\otimes\rho_{\mathsf{B}}\|^2. \tag{5.31}$$

Next consider the connected correlation function

$$C(\mathcal{A},\mathcal{B}) = \langle \mathcal{A}\otimes\mathcal{B}\rangle - \langle\mathcal{A}\rangle\langle\mathcal{B}\rangle \tag{5.32}$$

where $\mathcal{A}$ and $\mathcal{B}$ are operators with support on A and B respectively. In terms of the densities,

$$\begin{aligned} C(\mathcal{A},\mathcal{B}) &= \operatorname{Tr}\rho_{\mathsf{AB}}(\mathcal{A}\otimes\mathcal{B}) - \operatorname{Tr}(\rho_{\mathsf{A}}\otimes\rho_{\mathsf{B}})(\mathcal{A}\otimes\mathcal{B}) \\ &= \operatorname{Tr}(\rho_{\mathsf{AB}} - \rho_{\mathsf{A}}\otimes\rho_{\mathsf{B}})(\mathcal{A}\otimes\mathcal{B}). \end{aligned} \tag{5.33}$$

Therefore, the correlation function is bounded above by

$$C(\mathcal{A},\mathcal{B}) \leq \|\rho_{\mathsf{AB}} - \rho_{\mathsf{A}}\otimes\rho_{\mathsf{B}}\|\,\|\mathcal{A}\otimes\mathcal{B}\|. \tag{5.34}$$

The norm of the direct product is bounded by $\|\mathcal{A}\otimes\mathcal{B}\| \leq \|\mathcal{A}\|\,\|\mathcal{B}\|$ so that

$$\frac{C(\mathcal{A},\mathcal{B})}{\|\mathcal{A}\|\,\|\mathcal{B}\|} \leq \|\rho_{\mathsf{AB}} - \rho_{\mathsf{A}}\otimes\rho_{\mathsf{B}}\|. \tag{5.35}$$

The bound (5.31) on the mutual information imples [139]

$$C(\mathcal{A},\mathcal{B})^2 \leq 2\,I(\mathsf{A},\mathsf{B})\,\|\mathcal{A}\|^2\,\|\mathcal{B}\|^2. \tag{5.36}$$

5.5 Summary

In Chapter 5 we introduced the entanglement spectrum of the reduced density matrix and described how both are determined by the single-particle correlation function for non-interacting systems. We use the entanglement spectrum in Chapter 6 to compute geometric response in the quantum Hall effect. In Chapter 7, we use the reduced density matrix to classify symmetry-protected topological phases; for the classification, it is important that the reduced density matrix respect the same global symmetries as the Hamiltonian as demonstrated in Section 5.3. We also use the mutual information between subsystems (Section 5.4) as a diagnostic of coupling which may destroy an embedded topological phase.

Chapter 6

Momentum Polarization

6.1 Introduction

The momentum polarization is calculated in a cylindrical geometry from the expectation value of the translation operator T (in the periodic direction) applied only to one half of the cylinder. The expectation value can be computed using the reduced density matrix [130],

$$\tau \equiv \left\langle T^L \right\rangle = \mathrm{Tr}_L\, \rho_L T. \tag{6.1}$$

Tu, Zhang, and Qi [130] show that τ can be easily calculated for free-fermion systems using the entanglement spectrum to extract the topological spin h and central charge c of the conformal field theory at the edge of a topological phase. Consider that, in the long-wavelength limit, the reduced density matrix of a cylinder cut in half can be written in terms of the Hamiltonians H_{Ll} and H_{Lr} of the respective conformal edge theories of the left and right edges of the left half-cylinder only [130]:

$$\rho_L = \rho_{Ll} \otimes \rho_{Lr} = Z^{-1} e^{-\beta_l H_{Ll} - \beta_r H_{Lr}}. \tag{6.2}$$

The relevant half-cylinder translation operator is

$$T^L = \exp\left[i(P_l + P_r)\frac{\Delta y}{R} \right], \tag{6.3}$$

where Δy is the distance translated (which we take to be a multiple of the lattice constant for lattice systems), R is the radius of the cylinder, and P_l and P_r are the generators of translations (momentum operators) of the left

The material presented in Chapter 6 was previously published in: Thomas I. Tuegel and Taylor L. Hughes. "Hall viscosity and momentum transport in lattice and continuum models of the integer quantum Hall effect in strong magnetic fields". Phys. Rev. B **92**, 165127 (2015). DOI: 10.1103/PhysRevB.92.165127. Some figures are reprinted with modifications. Some text and captions have been modified.

and right edge theories on the half-cylinder, respectively [41, 130]. The left edge is far from the right half and uncorrelated so that $\beta_l \to \infty$; therefore only the ground state of the left edge contributes. The ground state expectation value of P_l is $h - c/24$ where h is the topological spin mod 1 and c is the chiral central charge mod 24 [41]. The contribution of the left edge is [130]

$$\mathrm{Tr}_{Ll}\, \rho_{Ll} \exp\left[iP_l \frac{\Delta y}{R}\right] = \exp\left[i\frac{\Delta y}{R}\Big(h - \frac{c}{24}\Big)\right] \tag{6.4}$$

On the other hand, β_r takes a finite value because the right edge is entangled with the right half-cylinder. In general, the right edge gives a non-universal contribution [130]

$$\mathrm{Tr}_{Lr}\, \rho_{Lr} \exp\left[iP_r \frac{\Delta y}{R}\right] = \exp\left[-2\pi R\alpha\right]. \tag{6.5}$$

The contributions of the left and right edge scale differently with R, so we can extract the central charge and topological spin.

For free fermions, the momentum polarization phase τ is easily calculated in terms of the entanglement spectrum for a cylinder by the formula [130]

$$\tau = \prod_{n,k} \frac{1}{2}\left[\left(1 + e^{ik\Delta y}\right) + \left(1 - e^{ik\Delta y}\right)\tanh \tfrac{1}{2}\varepsilon_n(k)\right] \tag{6.6}$$

where $\prod_{n,k}$ is a product over the bands n and y-wavenumbers k; $\varepsilon_n(k)$ is the entanglement eigenvalue of the state in band n with momentum $\hbar k$. The entanglement spectrum can be expressed in terms of the eigenvalues $\xi_n^{(L)}(k)$ of the single particle correlation function (5.12),

$$\varepsilon_n(k) = \log \frac{1 - \xi_n^{(L)}(k)}{\xi_n^{(L)}(k)}. \tag{6.7}$$

The correlation function is $C^{(L)}(k) = \left\langle c^\dagger_{(i,a)}(k) c_{(j,b)}(k)\right\rangle$ where k are the wavenumbers in the periodic direction, i, j run-over the lattice sites on the left half of the cylinder, and a, b run-over all of the onsite degrees of freedom. $C^{(L)}(k)$ projects states onto the left half of the cylinder, but we it is more useful to compute this formula in terms of the projections onto the right half, $\xi_n(k) = 1 - \xi_n^{(L)}(k)$. Using these identities, it is convenient to rewrite (6.6) as

$$\tau = \prod_{n,k} \frac{1}{2}\left[\left(1 + e^{ik\Delta y}\right) + \left(1 - e^{ik\Delta y}\right)(2\xi_n(k) - 1)\right]. \tag{6.8}$$

In a remarkable extension of this work, Zaletel, Mong, and Pollmann [142] show that in quantum Hall states, the Hall viscosity gives an imaginary contribution to the non-universal coefficient α,

$$\tau = \exp\left[i\frac{\Delta y}{R}\left(h - \frac{c}{24}\right) - 2\pi i R \Delta y \frac{\eta_H}{\hbar} + \ldots\right]; \tag{6.9}$$

additional non-universal terms with different R-scaling have been elided. They consider a full twist such that $\Delta y = 2\pi R$, but the result carries over for smaller Δy as well. Thus, the viscosity and central charge can be extracted from a fit of $2\pi R \operatorname{Arg} \tau$; the former from the quadratic coefficient, the latter from the constant coefficient.

We can understand how the momentum polarization phase encodes the viscosity by considering the action of the shear strain generators on the ground state. Here, we show that the Hall viscosity can be extracted by comparing the momentum polarization calculated with a real-space cut to the phase taken with an orbital cut. We note that Park and Haldane [92] identified two distinct contributions to the Hall viscosity, and the contribution which interests us here is due to changing the shape of the Landau orbitals under shear strain. The second contribution, the guiding center Hall viscosity, comes from the electron correlations and is absent in the integer quantum Hall models we study here. We review how the momentum polarization phase calculated with a real-space cut encodes both Hall viscosity contributions. Although we consider only the integer effect, the guiding center Hall viscosity also has a super-extensive term due to the non-zero net momentum in each half of the system [92]. We show that this background can be subtracted by calculating the momentum polarization phase with an *orbital* cut and comparing the two results.

6.2 Adiabatic response

Before continuing to calculate the momentum polarization phase, let us remind ourselves of the origin of the adiabatic curvature under strain. Suppose we are given a Hamiltonian H taking parameters in a space X and we are tasked to calculate the transport coefficients measuring the response of H to variation in X. Along a path in parameter space $X(t) \in \mathsf{X}$, the time-dependent Hamiltonian $H(t) = \mathrm{d}H\,(\dot{X})$ governs the dynamical evolution of

the system according to the Schrödinger equation,

$$i\hbar\,\partial_t\psi(t) = H(t)\psi(t). \tag{6.10}$$

The computation of transport coefficients would seem simply to be a matter of selecting an appropriate path $X(t)$, but we are plagued by one difficulty: in general, the time-dependent Schrödinger equation admits no stationary solution. The Adiabatic Theorem allows us to salvage this approach in the limit $\mathrm{d}H\,(\dot{X}) \to 0$, wherein $\psi(t)$ is an eigenstate of $H(t)$ at every instant [13, 61]. The price to pay is that $H(t)$ does not generate the adiabatic evolution of the system, i.e., the propagator $U(t, t_0)$ generated by $H(t)$,

$$i\hbar\,\partial_t U(t, t_0) = H(t)\,U(t, t_0) \tag{6.11}$$

does not respect the projector $P(t)$. Let $U_{\mathrm{Ad}}(t, t_0)$ be the adiabatic propagator that respects the projector,

$$U_{\mathrm{Ad}}(t, t_0)\,P(t_0) = P(t)\,U_{\mathrm{Ad}}(t, t_0) \tag{6.12}$$

and its complement $Q(t) = 1 - P(t)$ in the same way. Avron, Seiler, and Yaffe [6] showed that the adiabatic Hamiltonian

$$H_{\mathrm{Ad}} = H + i\hbar\,[\partial_t P, P] \tag{6.13}$$

generates an adiabatic propagator which approximates as closely as possible the dynamical evolution according to H in the sense that

$$P(t)U(t, t_0)P(t_0) = U_{\mathrm{Ad}}(t, t_0)P(t_0) + \mathcal{O}((t - t_0)^2) \tag{6.14}$$

and likewise for $Q(t)$. Response functions for the adiabatically-evolving state are computed using H_{Ad} in place of the dynamical Hamiltonian H. The response function is given by the expectation value [5, 7]

$$\langle\partial_j H_{\mathrm{Ad}}\rangle = \langle\partial_j E\rangle + i\hbar\,\langle[\partial_i P, \partial_j P]\rangle\dot{X}^i \tag{6.15}$$

where partial derivatives are taken in X. The commutator is the adiabatic curvature,

$$\langle[\partial_i P, \partial_j P]\rangle = \langle\partial_i\psi|\,\partial_j\psi\rangle - \langle\partial_j\psi|\,\partial_i\psi\rangle = -2i\,\mathrm{Im}\,\langle\partial_i\psi|\,\partial_j\psi\rangle. \tag{6.16}$$

Adiabatic responses such as the Hall conductivity or viscosity can be computed using the adiabatic curvature and Eq. (6.15) [7, 73].

6.3 Hall viscosity

Evaluating the momentum polarization phase reveals that the strain generators lead to a non-universal Hall viscosity contribution. This section closely follows Park and Haldane [92]. First, let us decompose our physical coordinate $\mathbf{R}$ into a guiding center coordinate $\tilde{\mathbf{r}}$ and an orbital coordinate $\mathbf{r}$:

$$\mathbf{R} = \tilde{\mathbf{r}} + \mathbf{r}. \tag{6.17}$$

There is a metric $G_{\mu\nu}$ associated with the physical coordinate $\mathbf{R}$, as well as metrics $\tilde{g}_{\mu\nu}$ and $g_{\mu\nu}$ associated with each coordinate $\tilde{\mathbf{r}}$ and $\mathbf{r}$, respectively. Let $\tilde{\jmath}^{\mu\nu}(\mathbf{R})$ be the strain generators in $\tilde{g}_{\mu\nu}$ acting at $\mathbf{R}$; likewise let $\jmath^{\mu\nu}(\mathbf{R})$ be the strain generators associated with $g_{\mu\nu}$. The strain generators obey at each point the commutation relations [92]

$$\left[\jmath^{\mu\nu}, \jmath^{\alpha\beta}\right] = -\frac{i}{2}\left(\epsilon^{\mu\alpha}\jmath^{\nu\beta} + \epsilon^{\mu\beta}\jmath^{\nu\alpha} + \mu \leftrightarrow \nu\right) \tag{6.18a}$$

$$\left[\tilde{\jmath}^{\mu\nu}, \tilde{\jmath}^{\alpha\beta}\right] = -\frac{i}{2}\left(\epsilon^{\mu\alpha}\tilde{\jmath}^{\nu\beta} + \epsilon^{\mu\beta}\tilde{\jmath}^{\nu\alpha} + \mu \leftrightarrow \nu\right) \tag{6.18b}$$

$$\left[\tilde{\jmath}^{\mu\nu}, \jmath^{\alpha\beta}\right] = 0, \tag{6.18c}$$

where we have suppressed the dependence on $\mathbf{R}$. The strain generator in the physical coordinate is

$$J^{\mu\nu}(\mathbf{R}) = \tilde{\jmath}^{\mu\nu}(\mathbf{R}) + \jmath^{\mu\nu}(\mathbf{R}) \tag{6.19}$$

so that the unitary operator implementing strain on quantum states is [14, 92]

$$W(\lambda) = \exp\left[i\int \mathrm{d}^2\mathbf{R}\ \lambda_{\mu\nu}(\mathbf{R})J^{\mu\nu}(\mathbf{R})\right] \tag{6.20}$$

where $\lambda_{\mu\nu}$ is a symmetric tensor parametrizing the strain.

The strain operator (6.20) can be written as the product of strain transformations on each coordinate because the strain generators on different coordinates commute (6.18):

$$W(\lambda) = w(\lambda)\tilde{w}(\lambda) \tag{6.21a}$$

$$w(\lambda) = \exp\left[i\int \mathrm{d}^2\mathbf{R}\ \lambda_{\mu\nu}(\mathbf{R})\jmath^{\mu\nu}(\mathbf{R})\right] \tag{6.21b}$$

$$\tilde{w}(\lambda) = \exp\left[i\int \mathrm{d}^2\mathbf{R}\ \lambda_{\mu\nu}(\mathbf{R})\tilde{\jmath}^{\mu\nu}(\mathbf{R})\right]. \tag{6.21c}$$

To first order in $\lambda_{\mu\nu}$, the variation in the metric under strain is [92]

$$\delta G_{\mu\nu}(\mathbf{R}) = -\epsilon^{\alpha\beta}G_{\mu\alpha}(\mathbf{R})\lambda_{\beta\nu}(\mathbf{R}) + \mu \leftrightarrow \nu. \tag{6.22}$$

In our particular case, translating half of the cylinder induces strain at the center,

$$\lambda_{\mu\nu}(x,y) = \delta(x)\Delta y \begin{pmatrix} 1 & 0 \\ 0 & 0 \end{pmatrix}. \tag{6.23}$$

The momentum polarization expectation value τ (6.8) is the ground state expectation value $\langle W(\lambda)\rangle$ under this strain field.

Before we proceed to compute the required expectation values and find the momentum polarization phase, let us see how the Hall viscosity enters the calculation. We can represent the viscosity tensor in terms of the adiabatic curvature (6.16) of the ground state under shear strain [7, 92]:

$$\begin{aligned} H^{\mu\nu\alpha\beta}(\mathbf{R}) &= 2\hbar\,\mathrm{Im}\left\langle \frac{\mathrm{d}\Psi(\lambda)}{\mathrm{d}\lambda_{\mu\nu}(\mathbf{R})} \middle| \frac{\mathrm{d}\Psi(\lambda)}{\mathrm{d}\lambda_{\alpha\beta}(\mathbf{R})} \right\rangle \\ &= -i\hbar\langle\Psi|\big[J^{\mu\nu}(\mathbf{R}), J^{\alpha\beta}(\mathbf{R})\big]|\Psi\rangle. \end{aligned} \tag{6.24}$$

where $|\Psi(\lambda)\rangle = W(\lambda)|\Psi\rangle$. Because the strain generator $J^{\mu\nu}$ is the sum of orbital and guiding center strain generators, we conclude that the viscosity also has contributions due to each strain generator, which we separately denote

$$\eta^{\mu\nu\alpha\beta} = -i\hbar\langle\Psi|\big[j^{\mu\nu}, j^{\alpha\beta}\big]|\Psi\rangle \tag{6.25a}$$

$$\tilde{\eta}^{\mu\nu\alpha\beta} = -i\hbar\langle\Psi|\big[\tilde{\jmath}^{\mu\nu}, \tilde{\jmath}^{\alpha\beta}\big]|\Psi\rangle \tag{6.25b}$$

Now, using the strain field (6.23), we find

$$\tau_{\mathrm{RES}} = \langle\Psi|W(\lambda)|\Psi\rangle = \langle\Psi|\tilde{w}(\lambda)|\Psi\rangle\langle\Psi|w(\lambda)|\Psi\rangle, \tag{6.26}$$

where τ_{RES} is the momentum polarization phase τ (6.8) computed with the real-space entanglement spectrum. The expectation value of $\tilde{w}$ is the momentum polarization phase computed with the orbital entanglement spectrum [92], while the expectation value of w is

$$\begin{aligned} \langle\Psi|w(\lambda)|\Psi\rangle &= \langle\Psi|\exp\left[i\int \mathrm{d}^2\mathbf{R}\ \lambda_{\mu\nu}(\mathbf{R})j^{\mu\nu}(\mathbf{R})\right]|\Psi\rangle \\ &= \langle\Psi|\exp\left[i\int \mathrm{d}^2\mathbf{R}\ \delta(x)\Delta y\, j^{xx}(\mathbf{R})\right]|\Psi\rangle. \end{aligned} \tag{6.27}$$

The expectation value can be moved inside the exponential because j^{xx} at different points commute,

$$\langle\Psi|w(\lambda)|\Psi\rangle = \exp\left[i\int \mathrm{d}^2\mathbf{R}\ \delta(x)\Delta y\,\langle\Psi|j^{xx}(\mathbf{R})|\Psi\rangle\right]. \tag{6.28}$$

Evaluating the integral, assuming a uniform ground state expectation value, gives

$$\langle\Psi|w(\lambda)|\Psi\rangle = \exp\left[2\pi i\, R\Delta y\, \langle\Psi|j^{xx}|\Psi\rangle\right], \tag{6.29}$$

where we have kept terms only to first order in Δy. Using the strain generator commutation relations (6.18), we substitute

$$\langle\Psi|j^{xx}|\Psi\rangle = i\langle\Psi|[j^{xx}, j^{xy}]|\Psi\rangle = -\frac{1}{\hbar}\eta^{xxxy} = -\frac{1}{\hbar}\eta_H \tag{6.30}$$

to find

$$\langle\Psi|w(\lambda)|\Psi\rangle = \exp\left[-\frac{2\pi i}{\hbar} R\Delta y\, \eta_H\right]. \tag{6.31}$$

Returning to the expression for the momentum polarization phase (6.26),

$$\tau_{\mathrm{RES}} = \tau_{\mathrm{OES}} \exp\left[-\frac{2\pi i}{\hbar} R\Delta y\, \eta_H\right], \tag{6.32}$$

where $\tau_{\mathrm{OES}} = \langle\Psi|\tilde{w}(\lambda)|\Psi\rangle$ is the momentum polarization phase computed with the orbital entanglement spectrum. Hence, we can determine that an alternate form of the (orbital contribution to the) Hall viscosity is given by

$$\eta_H = -\frac{\hbar}{2\pi\, R\Delta y} \operatorname{Arg} \frac{\tau_{\mathrm{RES}}}{\tau_{\mathrm{OES}}} \tag{6.33}$$

for systems in uniform magnetic fields.

6.4 Models

6.4.1 Landau and Dirac–Landau levels

The Hall viscosity can be determined (6.33) by computing the momentum polarization phases τ_{RES} and τ_{OES},

$$\tau_{\mathrm{RES}} = \prod_{n,k} \frac{1}{2}\left[\left(1 + e^{ik\Delta y}\right) + \left(1 - e^{ik\Delta y}\right)(2C_n(k) - 1)\right] \tag{6.34a}$$

$$\tau_{\mathrm{OES}} = \prod_{n} \prod_{k>0} e^{ik\Delta y}. \tag{6.34b}$$

We take $\prod_n$ to span the occupied Landau levels. The correlation function $C_n(k)$ (2.43b) is tabulated for small n (2.44) in Chapter 2. The Hall viscosity is extracted from the momentum polarization phases by isolating the term quadratic in R (6.33). The result is shown in the lower panel of Fig. 6.1,

which shows that the calculation converges when $L > 2\sqrt{2\pi}\ell_B$. This is the same criterion as for the convergence of the momentum transport calculation, shown again in the top panel of Fig. 6.1: each half of the cylinder must be wider than a single wavefunction. The Hall viscosity of Dirac–Landau levels can be expressed in terms of the Landau level Hall viscosity determined by this calculation, as shown in Sec. 2.5.2.

6.4.2 Hofstadter model

In Sec. 3.3.1, we calculated the Hall viscosity of the Hofstadter–Landau levels numerically using the momentum transport method. Now let us compare those results to the result of the momentum polarization method. We use the correlation function to compute (6.8) the momentum polarization phases,

$$\tau_{\mathrm{RES}} = \prod_{m,k} \frac{1}{2}\Big[\big(1+e^{ik\Delta y}\big) + \big(1-e^{ik\Delta y}\big)\Big(2\langle \mathcal{P}_R\rangle_{(m,k_y)} - 1\Big)\Big] \tag{6.35a}$$

$$\tau_{\mathrm{OES}} = \prod_{m,k} \frac{1}{2}\Big[\big(1+e^{ik\Delta y}\big) + \big(1-e^{ik\Delta y}\big)\Big(2\Theta(\langle x\rangle_{(m,k)}) - 1\Big)\Big], \tag{6.35b}$$

where Θ is the Heaviside step function and $\langle A\rangle_{(m,k_y)}$ denotes the expectation value of A in the state $|m,k_y\rangle$. In a lattice model, Δy must be an integer in units of the lattice constant. The resulting viscosity calculation is shown in Fig. 6.2. The Hall viscosity obtained for the first three Landau levels agrees with the continuum value in the weak field limit. Where the calculation converges, i.e., $q \gtrsim 20$, it agrees qualitatively with the momentum transport method, although the momentum polarization calculation appears to deviate less from the continuum Hall viscosity at small q.

6.4.3 Lattice Dirac model

The Hall viscosity of the lattice Dirac model was also calculated by the momentum polarization method (6.33) using the correlation function (6.8) to compute τ_{RES} and τ_{OES},

$$\tau_{\mathrm{RES}} = \prod_{j,k} \frac{1}{2}\Big[\big(1+e^{ik\Delta y}\big) + \big(1-e^{ik\Delta y}\big)\Big(2\langle \mathcal{P}_R\rangle_{(j,k)} - 1\Big)\Big] \tag{6.36a}$$

$$\tau_{\mathrm{OES}} = \prod_{j,k} \frac{1}{2}\Big[\big(1+e^{ik\Delta y}\big) + \big(1-e^{ik\Delta y}\big)\Big(2\Theta(\langle x\rangle_{(j,k_y)}) - 1\Big)\Big], \tag{6.36b}$$

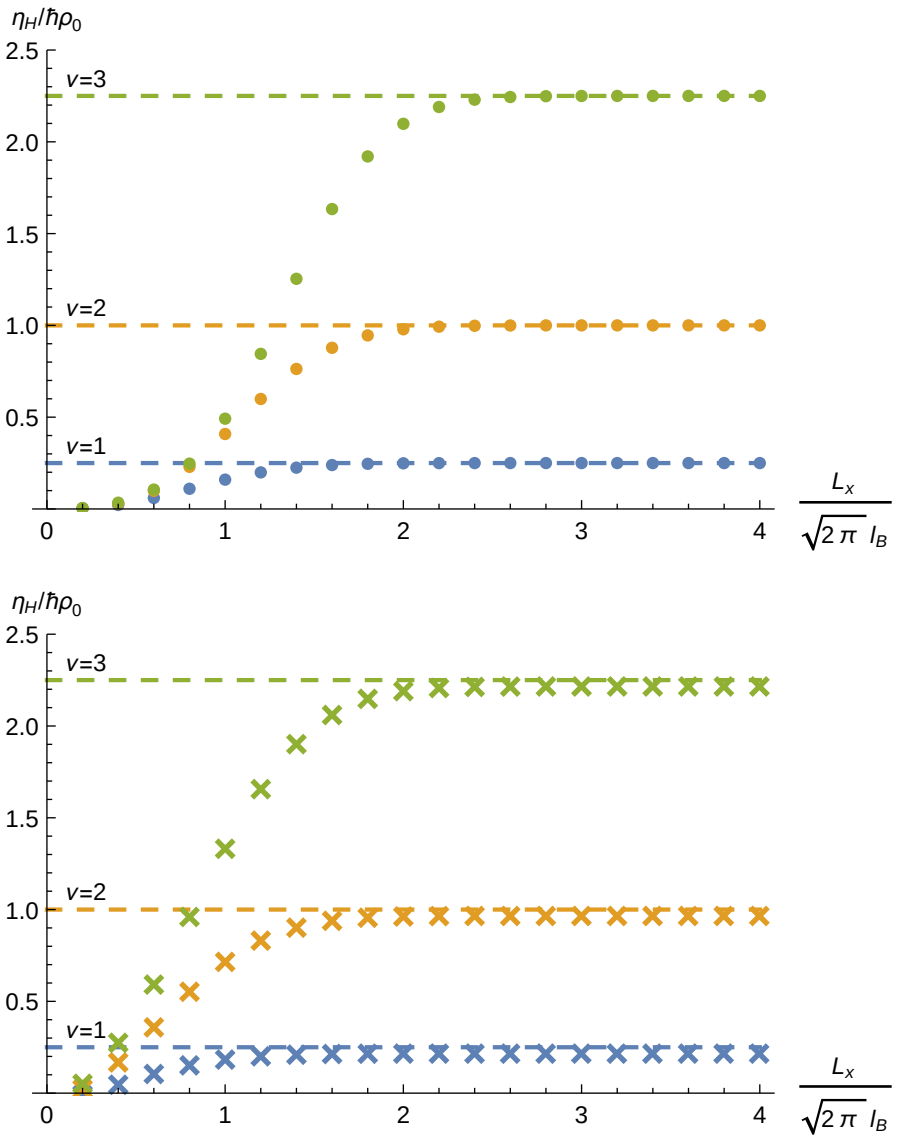

Figure 6.1: The Hall viscosity (η_H) of the lowest Landau levels calculated by the momentum transport method (above, from Figure 2.2) and by the momentum polarization method (below). The calculation converges when $L_x > 2\sqrt{2\pi}\ell_B$, i.e., when each half of the cylinder is wider than a single wavefunction. The Hall viscosity is given in units of $\hbar\rho_0$ where $\rho_0 = 1/2\pi\ell_B^2$ is the electron density of the lowest Landau level. From: Thomas I. Tuegel and Taylor L. Hughes. "Hall viscosity and momentum transport in lattice and continuum models of the integer quantum Hall effect in strong magnetic fields". Phys. Rev. B **92**, 165127 (2015). DOI: 10.1103/PhysRevB.92.165127.

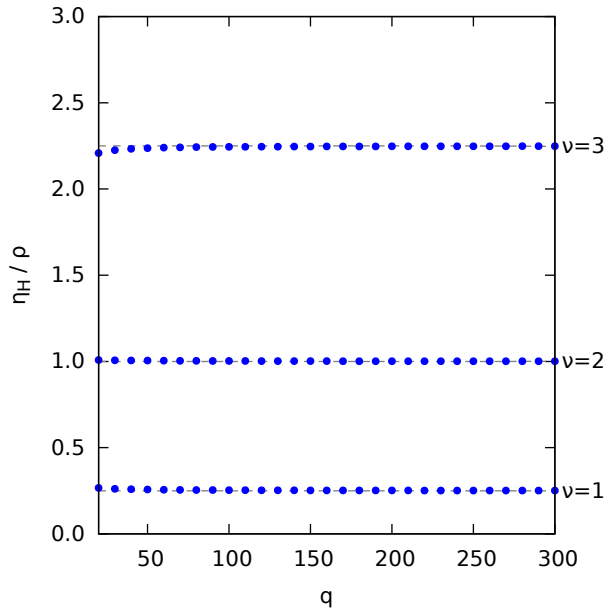

Figure 6.2: The Hall viscosity of the lowest Hofstadter Landau levels calculated by the momentum polarization method. The length of the system varies as $N_x = 2q - 1$ to keep commensurate boundaries. The Hall viscosity of the corresponding continuum Landau levels is shown by a dashed line for comparison. From: Thomas I. Tuegel and Taylor L. Hughes. "Hall viscosity and momentum transport in lattice and continuum models of the integer quantum Hall effect in strong magnetic fields". Phys. Rev. B **92**, 165127 (2015). DOI: 10.1103/PhysRevB.92.165127.

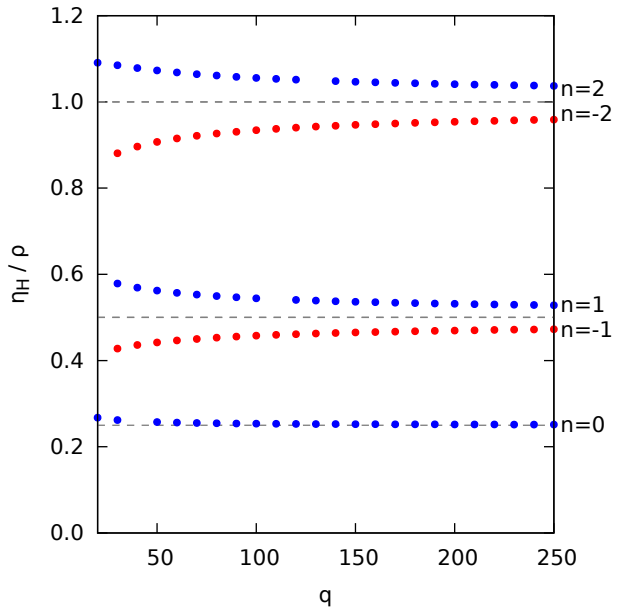

Figure 6.3: The Hall viscosity of the lowest lattice Dirac Landau levels calculated by the momentum polarization method. The length of the system varies as $N_x = 2q - 1$ to keep commensurate boundaries. In each case, only the indicated individual Landau levels are filled. Missing points indicate a convergence failure in the fitting to extract the Hall viscosity. From: Thomas I. Tuegel and Taylor L. Hughes. "Hall viscosity and momentum transport in lattice and continuum models of the integer quantum Hall effect in strong magnetic fields". Phys. Rev. B **92**, 165127 (2015). DOI: 10.1103/PhysRevB.92.165127.

where Θ is the Heaviside step function and $\langle A \rangle_{(m,k)}$ denotes the expectation value of A in the state $|m, k\rangle$. As with any lattice model, Δy must be an integer in units of the lattice constant. The Hall viscosity obtained this way agrees with the momentum transport calculation, showing the same convergence to the continuum value of η_H at large q (Fig. 6.3). Note that although both methods show a deviation from the continuum Hall viscosity at small q, the momentum polarization method shows a smaller deviation and with opposite sign. Points are missing from these figures where the fitting required for the momentum polarization method has failed. The momentum polarization method was only considered for calculating the Hall viscosity with individual Landau levels filled; we did not consider filling from the bottom of the spectrum because the momentum polarization method is only sensitive to the momentum mod 2π, so it is difficult to obtain convergence when momentum on the right half-cylinder is large.

6.5 Summary

In Chapter 6 we describe a method to compute the Hall viscosity coefficient using the entanglement spectrum by comparing orbital and real-space entanglement cuts. We compared this method to the momentum transport method developed in Chapter 2 and found the same results. We also applied the momentum polarization method to the lattice models in Chapter 3; while the results are qualitatively similar, there are unexplained discrepancies between the methods.

Chapter 7

Embedded Topological Insulators

7.1 Introduction

A composite system constructed from two free-fermion insulators of the same symmetry class and dimensionality is classified by the sum of topological invariants—even when the systems are coupled or disorder is present—if the bulk gap remains open and the common symmetry is unbroken [33, 63, 116, 125]. Herein we extend this classification to allow that the constituent systems are of different dimensionality. We focus on the case of a topological system embedded in a trivial system of higher dimension, which we term an *embedded TI*. By allowing for arrays of more than two constituent systems, we find that this classification already encompasses the weak and antiferromagnetic TIs.

7.2 Disentangling transformation

7.2.1 Topological invariants

In general, the topological invariants of a free-fermion system are computed using its single-particle spectral projector P. For a system with lattice translation symmetry, we can be more specific; given a single-particle Hamiltonian H, we construct the Bloch Hamiltonian at quasi-momentum $\mathbf{k}$ in the Brillouin zone,

$$H(\mathbf{k}) = \langle \mathbf{k}|H|\mathbf{k}\rangle \tag{7.1}$$

which has eigenvectors $\{|u_n(\mathbf{k})\rangle\}$ (the periodic Bloch functions) and eigenvectors $\{E_n(\mathbf{k})\}$ (the band energies). Eigenvectors of H are of the form $|u_n(\mathbf{k})\rangle \otimes |\mathbf{k}\rangle$. Using the Bloch functions, we can define the spectral projector

onto Bloch states over the Brillouin zone

$$P(\mathbf{k}) = \sum_{E_n(\mathbf{k})<E_\mathrm{F}} |u_n(\mathbf{k})\rangle\langle u_n(\mathbf{k})| \tag{7.2}$$

where E_F is the Fermi energy. Computing invariants of the system amounts to computing homotopy invariants of the smooth vector bundle over the Brillouin zone defined by $P(\mathbf{k})$ [19, 116]; which invariants are appropriate to compute depends on the dimensionality and global symmetries of the system [63, 99, 109, 113]. The projector $P(\mathbf{k})$ acts on Bloch states, but we can also construct the projector P onto the entire Hilbert space,

$$P = \int_\mathrm{BZ} \frac{\mathrm{d}\mathbf{k}}{|\mathcal{C}^\star|}\, P(\mathbf{k}) \otimes |\mathbf{k}\rangle\langle\mathbf{k}| \tag{7.3}$$

where the integral is normalized by the reciprocal unit cell volume $|\mathcal{C}^\star|$. Using the projector P enables other computation schemes—such as real-space formulas [83]—that do not necessarily rely on translation invariance. The projector P also defines the flat-band Hamiltonian,

$$H_\mathrm{flat} = 1 - 2P \quad \text{or} \quad H(\mathbf{k})_\mathrm{flat} = 1 - 2P(\mathbf{k}) \tag{7.4}$$

which is, with $E_\mathrm{F} = 0$, homotopic to the original Hamiltonian.

The remarkable feature of symmetry-protected topological phases is that their invariants are protected under continuous deformations of the system that do not close the bulk energy gap or break the protecting symmetry. For a projector P there is an equivalence class $[P]$ of homotopic projectors; if $c(P)$ is the topological index for P, then $c([P]) = c(P)$. $c(\cdot)$ takes values in an Abelian group, either $\mathbb{Z}$, $\mathbb{Z}_2$, or direct products thereof for weak SPT phases [33, 63, 121]. Let us consider two systems M and N with projectors P_M and P_N respectively. If $\dim \mathsf{M} = \dim \mathsf{N}$ and the systems respect the same global symmetries, then a decoupled, composite system $\mathsf{M} \otimes \mathsf{N}$ has as its projector $P_\mathsf{M} \oplus P_\mathsf{N}$ so that its classification is

$$c(P_\mathsf{M} \oplus P_\mathsf{N}) = c([P_\mathsf{M}]) + c([P_\mathsf{N}]). \tag{7.5}$$

If M and N are coupled so that the projector is $P_\mathsf{MN} \neq P_\mathsf{M} \oplus P_\mathsf{N}$, but the bulk gap remains open and the coupling does not spoil the protecting symmetry, then the classification does not change,

$$c(P_\mathsf{MN}) = c([P_\mathsf{M} \oplus P_\mathsf{N}]) = c([P_\mathsf{M}]) + c([P_\mathsf{N}]), \quad P_\mathsf{MN} \in [P_\mathsf{M} \oplus P_\mathsf{N}]. \tag{7.6}$$

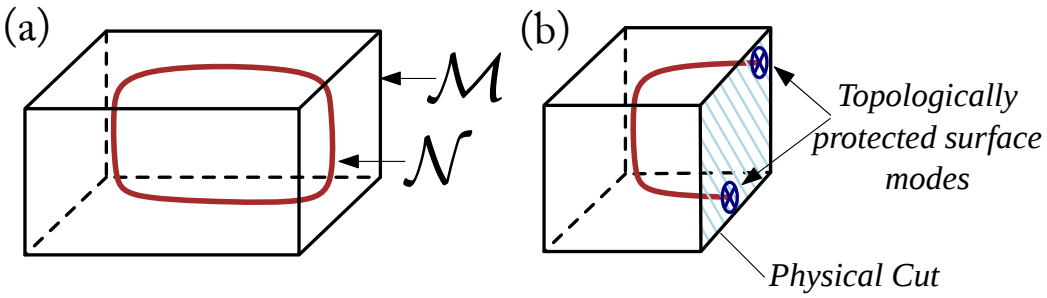

Figure 7.1: Examples of composite systems with $\dim \mathsf{N} < \dim \mathsf{M}$, (a) a closed system and (b) a system where M has been cleaved to expose topological surface states bound on N. From: Thomas I. Tuegel, Victor Chua, and Taylor L. Hughes. "Embedded Topological Insulators" (2018). arXiv: 1802.06790. Credit: Victor Chua.

If now we allow $\dim \mathsf{M} \neq \dim \mathsf{N}$, then Eq. (7.5) is invalid: what could it possibly mean to apply the same classifier $c(\cdot)$ to two projectors P_{M} and P_{N} which do not belong to the same classification? Although Eq. (7.5) does not apply, the composite system *does* retain a signature of the topology of its components: Consider the case when $c(P_{\mathsf{M}}) = 0$ and take $\dim \mathsf{N} < \dim \mathsf{M}$ as in Fig. 7.1; assuming no coupling between M and N, a physical cut through M and N certainly leaves topological states on the surface of M localized at N. When the systems are coupled, the result is less clear. We expect (perhaps naively) that if the coupling does not spoil the protecting symmetry, then the surface states survive as long as the bulk gap remains open. In the next section, we make this intuition precise by disentangling the coupled system.

7.2.2 Disentangled projectors

To disentangle M from N, we begin by making an entanglement cut between the two components. The entanglement cut leads to the single-particle reduced density matrices,

$$\rho_{\mathsf{N}} = \operatorname{Tr}_{\mathsf{M}} P_{\mathsf{MN}} \quad \text{and} \quad \rho_{\mathsf{M}} = \operatorname{Tr}_{\mathsf{N}} P_{\mathsf{MN}}. \tag{7.7}$$

If the entanglement spectrum $\{\xi_i\}$ of ρ_{N} is gapped at $\xi = \frac{1}{2}$, then we can form the entanglement projector

$$\Pi_{\mathsf{N}} = \sum_{\xi_i > \frac{1}{2}} |\xi_i\rangle\langle\xi_i|. \tag{7.8}$$

If the spectrum of ρ_{N} is gapped, the spectrum of ρ_{M} is also gapped (5.18) so that we can construct Π_{M}. The gap in the entanglement spectrum falls at $\xi = \frac{1}{2}$ because this correlation eigenvalue corresponds to the Fermi (entanglement) energy in the Fermi-Dirac distribution for ξ. Coupling M to N causes the two to become entangled, i.e., the entanglement entropy is non-zero:

$$S(\rho_{\mathsf{M}}) = S(\rho_{\mathsf{N}}) > 0. \tag{7.9}$$

The entanglement-spectral projectors $\Pi_{\square}$ have *no* entanglement entropy; hence we refer to Π_{M} and Π_{N} as the *disentangled* projectors and to the construction procedure as *disentangling*. The entanglement cut is made to preserve the global symmetries, so we can compute the topological indices $c(\Pi_{\mathsf{N}})$ and $c(\Pi_{\mathsf{M}})$.

The disentangled projectors are significant because they are adiabatically connected to the respective decoupled projectors if the bulk gap remains open,

$$\Pi_{\mathsf{M}} \in [P_{\mathsf{M}}] \qquad \Pi_{\mathsf{N}} \in [P_{\mathsf{N}}] \tag{7.10}$$

so that $c(\Pi_{\mathsf{M}}) = c(P_{\mathsf{M}})$ and $c(\Pi_{\mathsf{N}}) = c(P_{\mathsf{N}})$, i.e., each system retains the signature of its component topology. That the disentangled projectors reflect the decoupled topology of each subsystem follows from the continuity of the projector: Consider the single particle spectral projector of the decoupled system, $P_{\mathsf{M}\oplus\mathsf{N}}$; in the form of a matrix, it is diagonal, given by

$$P_{\mathsf{M}\oplus\mathsf{N}} = \begin{pmatrix} P_{\mathsf{M}} & \\ & P_{\mathsf{N}} \end{pmatrix}. \tag{7.11}$$

The entanglement spectrum is gapped because the systems are uncoupled. Suppose that the systems are coupled so that the spectral projector is no longer diagonal, but given by

$$P_{\mathsf{MN}} = \begin{pmatrix} \Pi_{\mathsf{M}} & \Pi_{\mathsf{MN}} \\ \Pi_{\mathsf{MN}}^{\dagger} & \Pi_{\mathsf{N}} \end{pmatrix}. \tag{7.12}$$

If the coupling does not break the protecting symmetry or close the bulk energy gap, then P_{MN} is a continuous deformation of $P_{\mathsf{M}\oplus\mathsf{N}}$. Each block of P_{MN} must therefore be a continuous deformation, or $\Pi_{\mathsf{M}} \in [P_{\mathsf{M}}]$ and $\Pi_{\mathsf{N}} \in [P_{\mathsf{N}}]$.

Although we have explicitly discussed the case that $c(\Pi_{\mathsf{M}}) = 0$, the disentangling procedure applies equally to cases where M is non-trivial. We can

also consider a system with many regions of interest, which we can successively disentangle so that in general a system $\mathsf{S} = \bigsqcup_i^N \mathsf{R}_i$ composed of N disjoint subsystems R_i is classified by the direct product of indices,

$$c(\{\mathsf{R}_i\}) = \bigotimes_i^N c(\Pi_{\mathsf{R}_i}) = \big(c(\Pi_{\mathsf{R}_1}),\, c(\Pi_{\mathsf{R}_2}),\, \ldots,\, c(\Pi_{\mathsf{R}_N})\big). \tag{7.13}$$

A nontrivial composite index does not guarantee the existence of topological states on a particular surface; we must consider, for example, which—if any—of the component systems intersects the cut. In the presence of multiple topological components, surface states are also subject to finite size effects: correlations between components are generally exponentially suppressed in an insulator, but nearby surface states may yet couple and open a gap—albeit a suppressed gap. Finite size effects also compromise the integrity of surface states in ordinary topological insulators—consider that the definition of the projector (7.3) is only valid in the thermodynamic limit—so we do not consider this a flaw in the composite index. The mutual information quantifies the correlation between two components; in the limit $I(\mathsf{R}_i, \mathsf{R}_j) \to 0$, the components R_i and R_j are independent with surface states that do not couple together. We will consider the mutual information again in Section 7.3.2.

7.3 Isolated embedded TIs

7.3.1 Topological wires

One of the simplest realizations of an embedded TI is a chiral symmetric wire embedded in a trivial two-dimensional insulator. Chiral symmetry is associated with a Hamiltonian that respects the symmetry of a bipartite lattice by coupling only opposite sublattices. Let S be the chirality operator with eigenvalues ± 1 on each respective sublattice; the system has chiral symmetry if $(HS + SH) = 0$. The only topological insulators in one dimension fall into the chiral-symmetric AIII, BDI, (both carrying a $\mathbb{Z}$ invariant) and CII (carrying a $2\mathbb{Z}$ invariant) classes. For simplicity, we use wires in the BDI class having the Bloch Hamiltonian

$$H_{\mathrm{BDI}}(k_x) = \sigma^1\, t_1 \sin k_x + \sigma^2 (t_2 - t_1 \cos k_x) \tag{7.14}$$

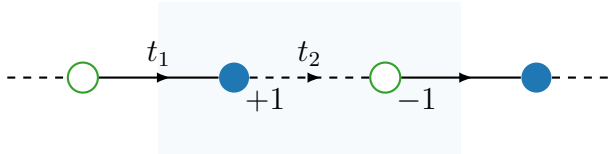

Figure 7.2: A two-orbital model of a class BDI chiral-symmetric wire. The unit cell is indicated by the light, shaded rectangle. The subsites have chirality $+1$ (solid blue circle) and -1 (open green circle). The intercell hopping is it_1 (directed solid black line) and the intracell hopping is it_2 (directed dashed black line).

which has eigenvalues and eigenvectors $E_n(k_x)$ and $|u_n(k_x)\rangle$ respectively; the Hamiltonian and Bloch functions are taken in the periodic gauge, i.e.,

$$H(k_x + 2\pi) = H(k_x) \tag{7.15a}$$
$$|u_n(k_x + 2\pi)\rangle = |u_n(k_x)\rangle \tag{7.15b}$$

so that the winding number ν below is quantized [131]. The Hamiltonian has particle-hole symmetry realized as $P = K$ (where K is complex conjugation), time-reversal symmetry realized as $T = K\sigma^3$, and chiral symmetry $S = \sigma^3$. A representative real-space schematic of the model is shown in Fig. 7.2. The topological invariant $\nu \in \mathbb{Z}$ is given by

$$\nu = \int \frac{\mathrm{d}k_x}{2\pi} \sum_n \langle u_n(k_x)|iS\,\partial_{k_x}|u_n(k_x)\rangle \tag{7.16}$$

where $\sum_n$ is the sum over *all* Bloch bands. Each Bloch band has a chiral partner with opposite energy, so the sum may be taken over only occupied Bloch bands instead,

$$\nu = \int \frac{\mathrm{d}k_x}{\pi} \sum_n^{E_n<0} \langle u_n(k_x)|iS\,\partial_{k_x}|u_n(k_x)\rangle. \tag{7.17}$$

The Hamiltonian in Eq. (7.14) has a topological phase with $\nu = 1$ when $|t_1| > |t_2|$ and a trivial phase with $\nu = 0$ when $|t_1| < |t_2|$.

The one-dimensional class BDI wire can be extended into two dimensions by stacking wires in an array. Chiral symmetry requires the unit cell be enlarged as indicated and the chirality operator alternates sign between wires, $S = \sigma^3 \otimes \sigma^3$. The Bloch Hamiltonian is

$$H_2(k_x, k_y) = \mathbb{1} \otimes H_{\mathrm{BDI}}(k_x) + \left[\sigma^1(t_3 \cos k_y + t_4) + \sigma^2 t_3 \sin k_y\right] \otimes \mathbb{1}. \tag{7.18}$$

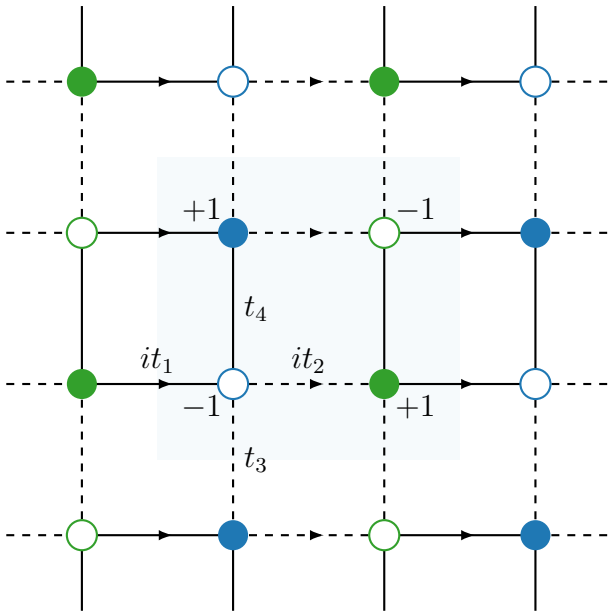

Figure 7.3: An array of two class BDI wires. The unit cell is indicated by the light, shaded rectangle. The subsites have chirality $+1$ (solid) and -1 (open). The subsite colors are used only to visually distinguish the two wires. The horizontal hopping potentials are it_1 (inter-cell, directed solid black line) and it_2 (intra-cell, directed dashed black line). The inter-layer hopping potentials are t_3 (inter-cell, undirected dashed black line) and t_4 (intra-cell, undirected solid black line).

Each wire is made trivial by choosing $|t_1| < |t_2|$ as described above. The wires are weakly coupled with dimerized inter-layer hopping to prevent formation of a strong or weak TI in the y-direction, i.e., $|t_4| < |t_3| < |t_1|$. With no topological states on any surface, the bulk model is trivial under every classification. A topological wire can be embedded into the real-space corresponding to (7.18) by replacing one trivial wire with a topological wire, i.e., choosing new hopping potentials $|t_1'| > |t_2'|$ for one wire, shown schematically in Fig. 7.4. Exact diagonalization of the real-space system with open boundaries shows (Fig. 7.5) zero modes localized on the wire at the surface. The entanglement spectrum of the system with closed boundaries (Fig. 7.6) is gapped and the disentangled projector of the embedded TI has $\nu = 1$.

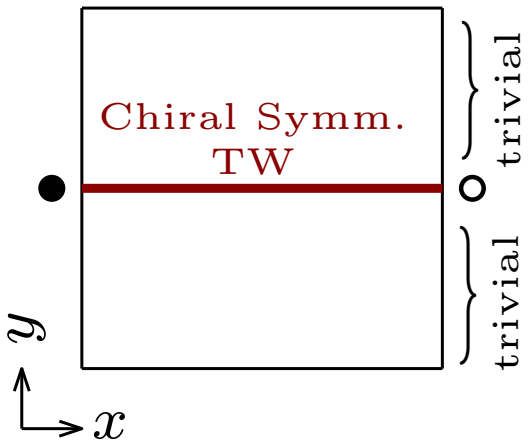

Figure 7.4: Schematic of an embedded topological wire (dark red line) in two dimensions. The impurity layer is a class BDI wire with $|t_1'| > |t_2'|$ surrounded by a trivial bulk insulator. Topological zero modes are bound on the embedded TI at the surface. From: Thomas I. Tuegel, Victor Chua, and Taylor L. Hughes. "Embedded Topological Insulators" (2018). arXiv: 1802.06790. Credit: Victor Chua.

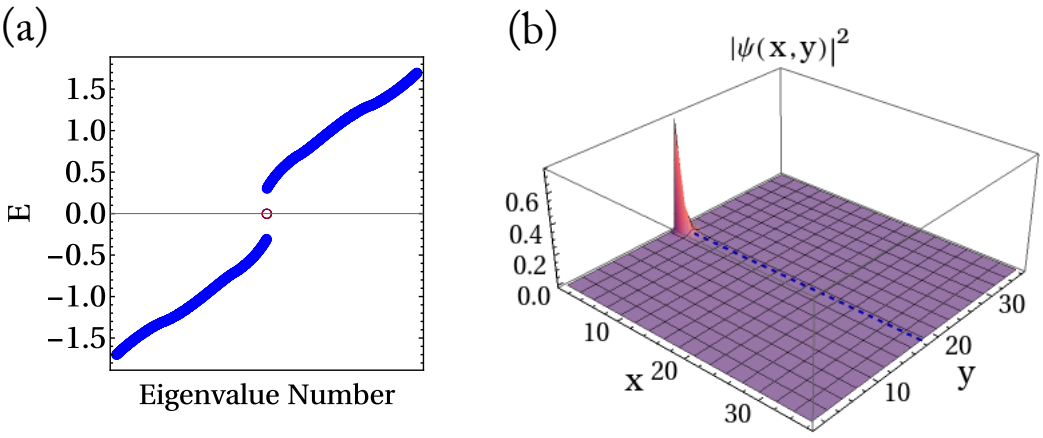

Figure 7.5: (a) Energy spectrum of the system with open boundaries, obtained by exact diagonalization, showing the topological zero modes. (b) The zero modes are localized on the embedded TI (dashed line). The system has dimensions $L_x = L_y = 36$. The bulk insulator has parameters $(t_1, t_2) = (0.5, 1.0)$ and $(t_3, t_4) = (0.1, 0.1)$. The embedded topological wire has parameters $(t_1', t_2') = (1.0, 0.5)$. From: Thomas I. Tuegel, Victor Chua, and Taylor L. Hughes. "Embedded Topological Insulators" (2018). arXiv: 1802.06790. Credit: Victor Chua.

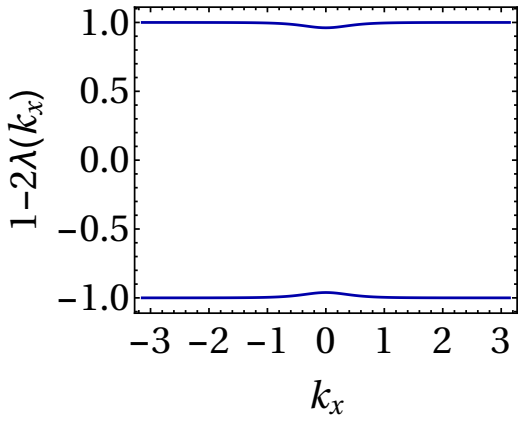

Figure 7.6: The entanglement spectrum of a closed, two-dimensional system with a single embedded topological wire. The topological invariant of the disentangled bands is $\nu = 1$, as anticipated by the presence of topological zero modes in the system with open boundaries. The bulk insulator has parameters $(t_1, t_2) = (0.5, 1.0)$ and $(t_3, t_4) = (0.1, 0.1)$. The embedded topological wire has parameters $(t_1', t_2') = (1.0, 0.5)$. From: Thomas I. Tuegel, Victor Chua, and Taylor L. Hughes. "Embedded Topological Insulators" (2018). arXiv: 1802.06790. Credit: Victor Chua.

7.3.2 Chern insulators

In three dimensions, an embedded TI can be realized as a two-dimensional Chern insulator with $\mathrm{Ch}_1 = 1$ embedded into a trivial bulk comprised of a stack of Chern insulators in the trivial phase. The two-dimensional Chern insulator breaks time-reversal, particle-hole, and chiral symmetries and so falls into class A with a $\mathbb{Z}$-valued invariant. A simple two-orbital Chern insulator has the Bloch Hamiltonian

$$H_{\mathrm{A}}(k_x, k_y) = \sigma^1 \sin k_x + \sigma^2 \sin k_y + \sigma^3(2 - m - \cos k_x - \cos k_y) \quad (7.19)$$

with topological invariant Ch_1 determined by m,

$$\mathrm{Ch}_1 = \begin{cases} 0 & m < 0 \\ +1 & 0 < m < 2 \\ -1 & 2 < m < 4 \\ 0 & m > 4. \end{cases} \quad (7.20)$$

The three-dimensional bulk stack of insulators has Bloch Hamiltonian

$$H_3(\mathbf{k}) = H_{\mathrm{A}}(k_x, k_y) + \mathbb{1}\, 2\delta_z \cos k_z \quad (7.21)$$

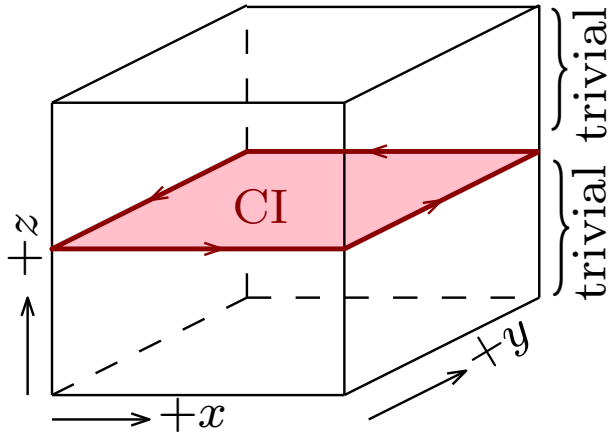

Figure 7.7: Schematic diagram of a Chern insulator (red) embedded in a trivial three-dimensional bulk. Chiral edge currents (arrows) appear on open boundaries in the x- and y-directions. From: Thomas I. Tuegel, Victor Chua, and Taylor L. Hughes. "Embedded Topological Insulators" (2018). arXiv: 1802.06790. Credit: Victor Chua.

where we set $m < 0$ in H_{A} to trivialize the layers. The bulk three-dimensional model is trivial under all classifications. A single Chern insulator is embedded by transforming the Bloch Hamiltonian into real-space and picking out one layer (Fig. 7.7) to replace m with m', setting $0 < m' < 2$. For small δ_z, e.g., $|\delta_z| < \min(|m|, |m'|)$, the composite system remains gapped and therefore adiabatically connected to the decoupled limit ($\delta_z = 0$). Chiral edge modes appear on an open boundary in the y-direction (Fig. 7.8) that are localized on the impurity layer (Fig. 7.9). The entanglement spectrum of the closed system is gapped (Fig. 7.10) and the disentangled bands have a topological invariant $\mathrm{Ch}_1 = 1$.

By embedding a pair of Chern insulators, we can construct an example to demonstate that two embedded TIs with quantized topological invariants of disentangled projectors may be trivial overall. Consider embedding two Chern insulators in two different phases with $0 < m' < 2$ ($\mathrm{Ch}_1 = +1$) and $2 < m'' < 4$ ($\mathrm{Ch}_1 = -1$), shown schematically in Fig. 7.11. Considered as a two-dimensional band insulator, the system is topologically trivial, but the embedded layers have chiral edge states with opposite dispersion shown in Fig. 7.12 crossing $E = 0$ at $k_x = 0, \pi$. Consequently, the surface is gapless as long as the bulk gap does not close.

Instead of embedding two Chern insulators with different parameters, we

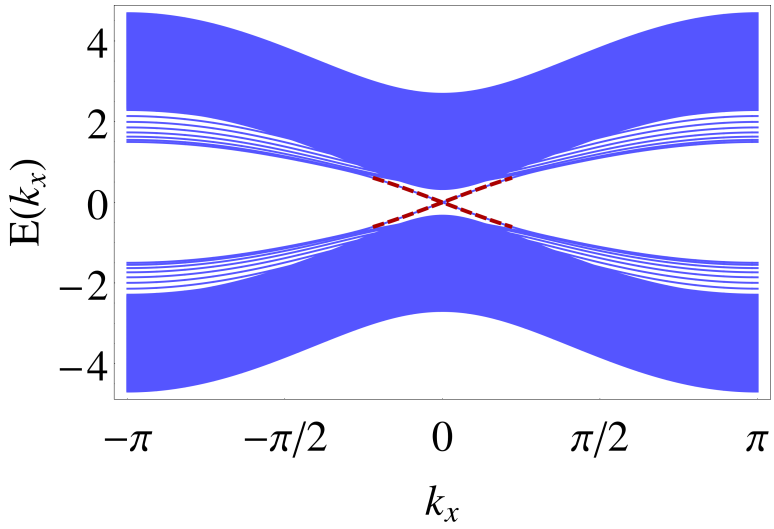

Figure 7.8: Energy spectrum of an embedded Chern insulator in a trivial three-dimensional bulk. Two-dimensional bands (thin blue lines) localize near the embedded layer whereas three-dimensional bands (thick blue lines) permeate the bulk. Topological edge modes (red) appear on open boundaries in the y-direction. The system is infinite in the x-direction, but finite size $L_y = L_z = 20$ in the y- and z-directions. The y-direction has open boundaries, while the x- and z-directions have periodic boundary conditions. The trivial bulk has $m = -0.5$, the embedded layer has $m' = 0.5$, and the interlayer hopping potential is $\delta_z = 0.1$. From: Thomas I. Tuegel, Victor Chua, and Taylor L. Hughes. "Embedded Topological Insulators" (2018). arXiv: 1802.06790. Credit: Victor Chua.

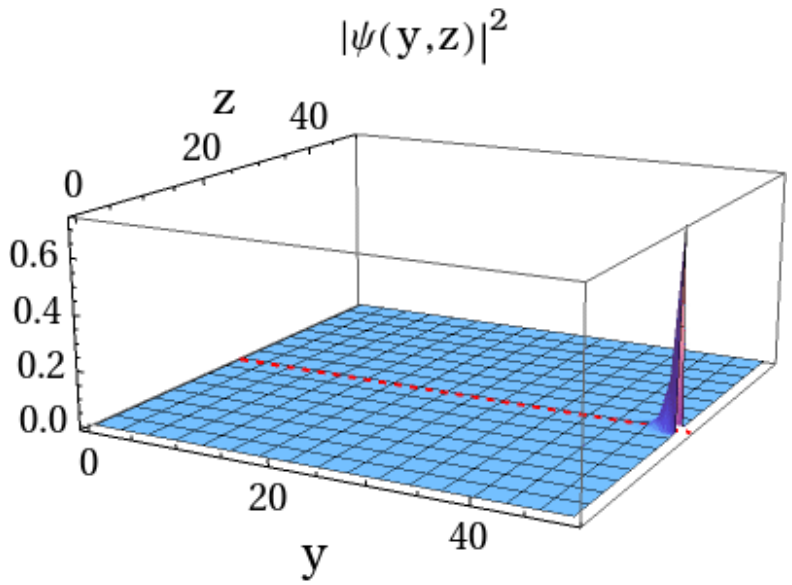

Figure 7.9: The zero modes are localized on the embedded Chern insulator (dashed red line). The system has dimensions $L_y = L_z = 48$ with fixed $k_x = 0$. The y-direction has open boundaries, while the x- and z-directions have periodic boundary conditions. The trivial bulk has $m = -0.5$, the embedded layer has $m' = 0.5$, and the inter-layer hopping potential is $\delta_z = 0.1$. From: Thomas I. Tuegel, Victor Chua, and Taylor L. Hughes. "Embedded Topological Insulators" (2018). arXiv: 1802.06790. Credit: Victor Chua.

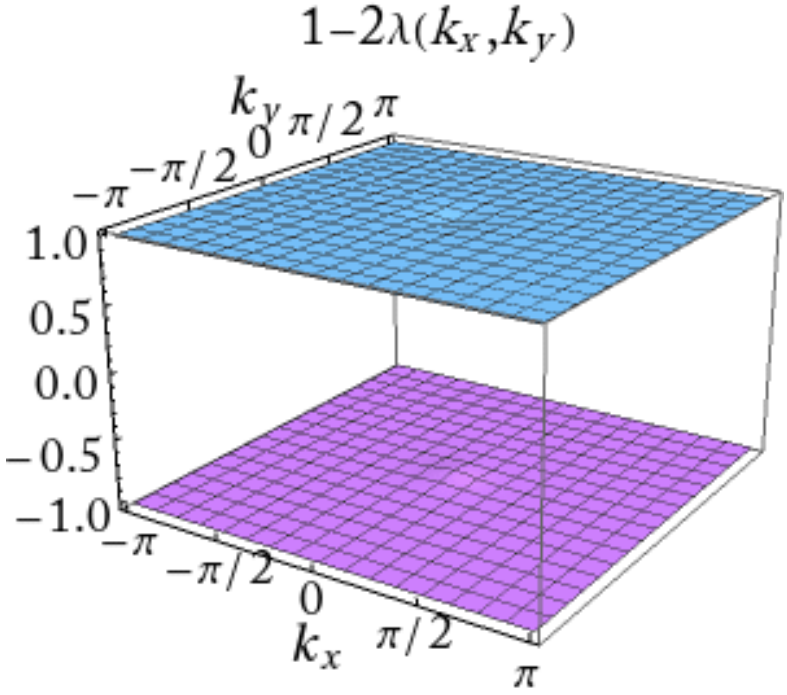

Figure 7.10: The entanglement spectrum of a closed, three-dimensional system with a single embedded topological Chern insulator. The topological invariant of the disentangled bands is $\mathrm{Ch}_1 = 1$, as anticipated by the presence of topological surface states in the system with open boundaries. The system has $L_z = 20$ layers, where the trivial bulk has $m = -0.5$, the embedded layer has $m' = 0.5$, and the inter-layer hopping potential is $\delta_z = 0.1$. From: Thomas I. Tuegel, Victor Chua, and Taylor L. Hughes. "Embedded Topological Insulators" (2018). arXiv: 1802.06790. Credit: Victor Chua.

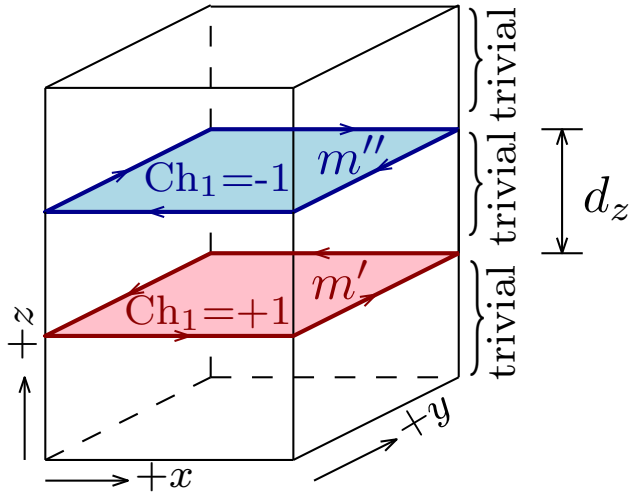

Figure 7.11: Schematic of two embedded Chern insulators in distinct phases. The lower (red) and upper (blue) impurity layers are Chern insulators of opposite topological invariants $\mathrm{Ch}_1 = \pm 1$ with $m = m'$ and $m = m''$ respectively. d_z denotes the number of trivial layers between embedded layers. From: Thomas I. Tuegel, Victor Chua, and Taylor L. Hughes. "Embedded Topological Insulators" (2018). arXiv: 1802.06790. Credit: Victor Chua.

can embed a $\mathrm{Ch}_1 = +1$ insulator and its time-reversal partner, depicted in Fig. 7.13(a). Each embedded layer has a gapped entanglement spectrum as shown in Fig. 7.13(b) and the composite index (7.13) is well defined, although the system is topologically trivial as a two-dimensional band insulator. When the layers are decoupled, the surface states must be localized to each embedded layer and so remain gapless as in Fig. 7.14(b). When the layers are coupled, however, the topological surface states are gapped as seen in Fig. 7.14(a). Figure 7.14(c) shows that the surface gap closes quickly as the layers are separated; we recover the topological surface states when the layers are sufficiently separated. The opening of the surface gap is indicated in the non-zero mutual information in Fig. 7.13(c). The mutual information of the embedded pair decays exponentially in Fig. 7.13(d) with the separation between embedded layers, as anticipated for a band insulator. Figure 7.15 illustrates the three contributions to the mutual information. The mutual information is computed without a boundary present, i.e., in periodic boundary conditions; the data needed to predict the surface mode coupling is already present in the bulk system.

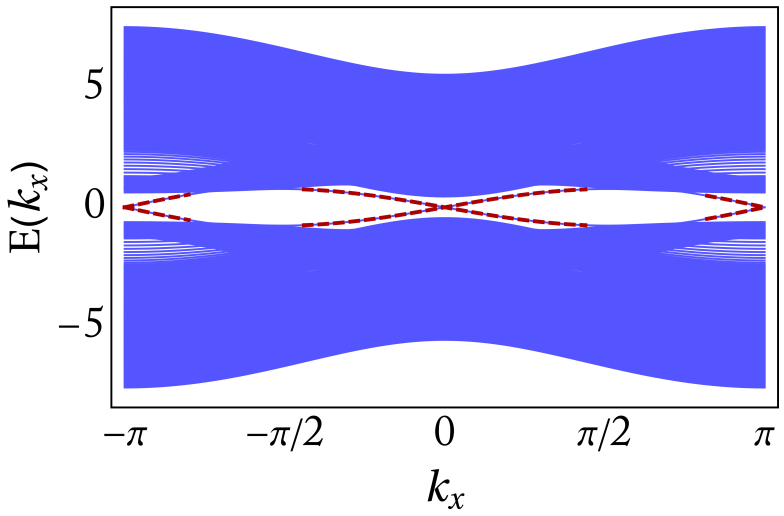

Figure 7.12: Spectrum of two embedded Chern insulators in distinct phases. Gapless topological edge modes localized on their respective layer (dashed red lines) cross at $k_x = 0, \pi$. The crystal has $L_z = 20$ layers with periodic boundary conditions and $d_z = 4$ layers between embedded TIs. There are open boundary conditions in the y-direction with size $L_y = 20$. The trivial layers have $m = -2$ and the $\mathrm{Ch}_1 = \pm 1$ layers have $m' = 1$ and $m'' = 3$ respectively. The inter-layer hopping potential is $\delta_z = 0.8$. From: Thomas I. Tuegel, Victor Chua, and Taylor L. Hughes. "Embedded Topological Insulators" (2018). arXiv: 1802.06790. Credit: Victor Chua.

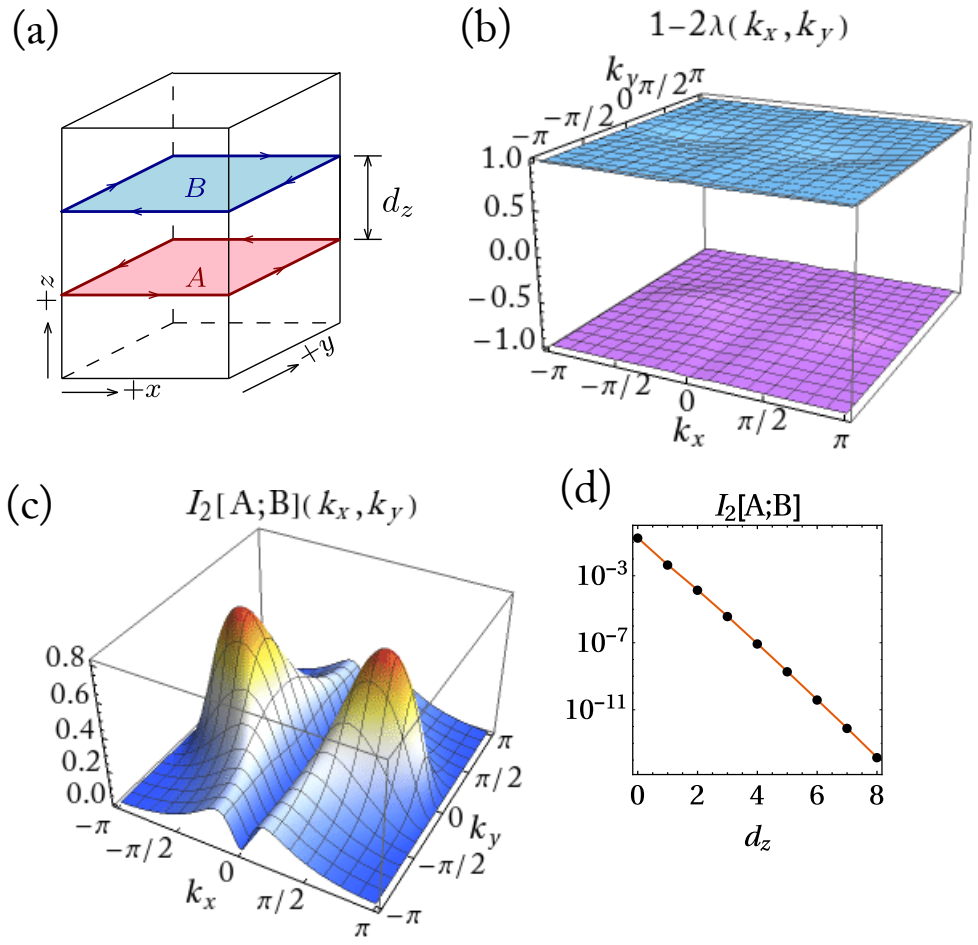

Figure 7.13: Mutual information measures of embedded time-reversal pair of Chern insulators. (a) Schematic of two embedded Chern insulators related by time-reversal. (b) The entanglement spectrum of region A is gapped, even at $d_z = 0$. The lower entanglement band has Chern number $\mathrm{Ch}_1 = +1$. (c) The mutual information band structure $I(\mathsf{A},\mathsf{B})(\mathbf{k})$ between the two embedded layers at $d_z = 0$. (d) The total mutual information $I(\mathsf{A},\mathsf{B})$ decays exponentially as the layers are separated. The trivial layers have $m = -2$ and the non-trivial layers have $m' = 1$. The inter-layer hopping potential is $\delta_z = 0.4$. The system is finite with $L_z = 24$ layers and periodic boundary conditions in the x- and y-direction. From: Thomas I. Tuegel, Victor Chua, and Taylor L. Hughes. "Embedded Topological Insulators" (2018). arXiv: 1802.06790. Credit: Victor Chua.

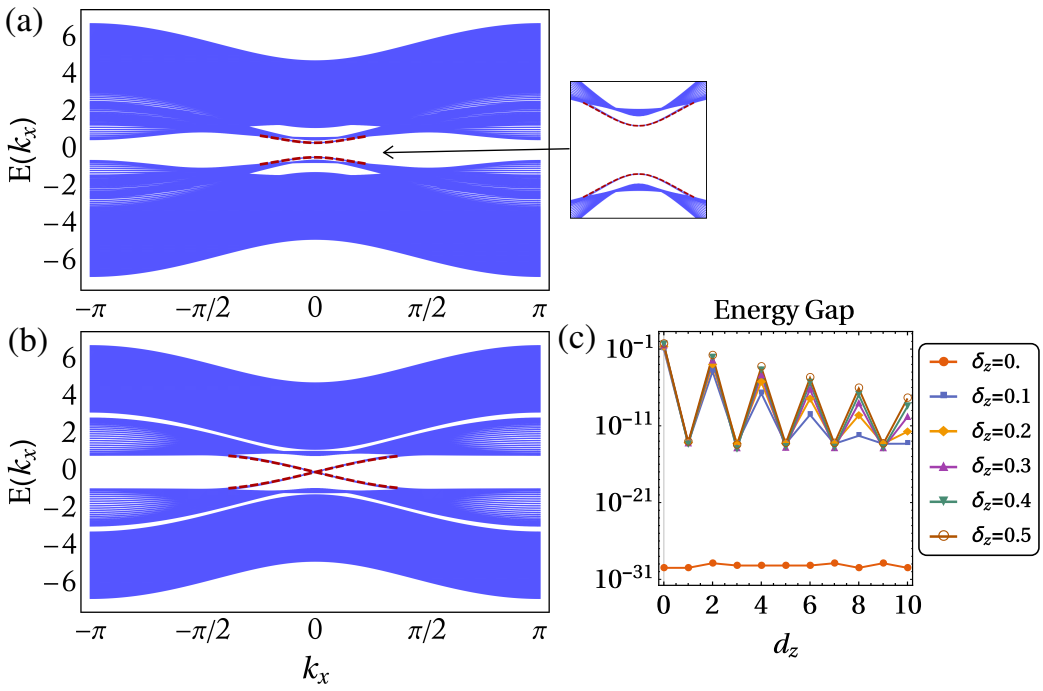

Figure 7.14: Energy spectra of embedded time-reversal pair of Chern insulators with edge states (red dashed lines) crossing at $k_x = 0$. (a) The edge states are gapped when $d_z = 0$ and $\delta_z = 0.4$. (b) When the embedded layers are separated at $d_z = 8$ and $\delta_z = 0.4$, the edge states are nearly gapless. (c) The spectral gap at $k_x = 0$ closes quickly as d_z increases. The limit of machine precision is shown at $\delta_z = 0$. The trivial layers have $m = -2$ and the embedded non-trivial layers have $m' = 1$. The system is finite with $L_y = L_z = 20$ with periodic boundary conditions in the z-direction, but an open boundary in the y-direction. From: Thomas I. Tuegel, Victor Chua, and Taylor L. Hughes. "Embedded Topological Insulators" (2018). arXiv: 1802.06790. Credit: Victor Chua.

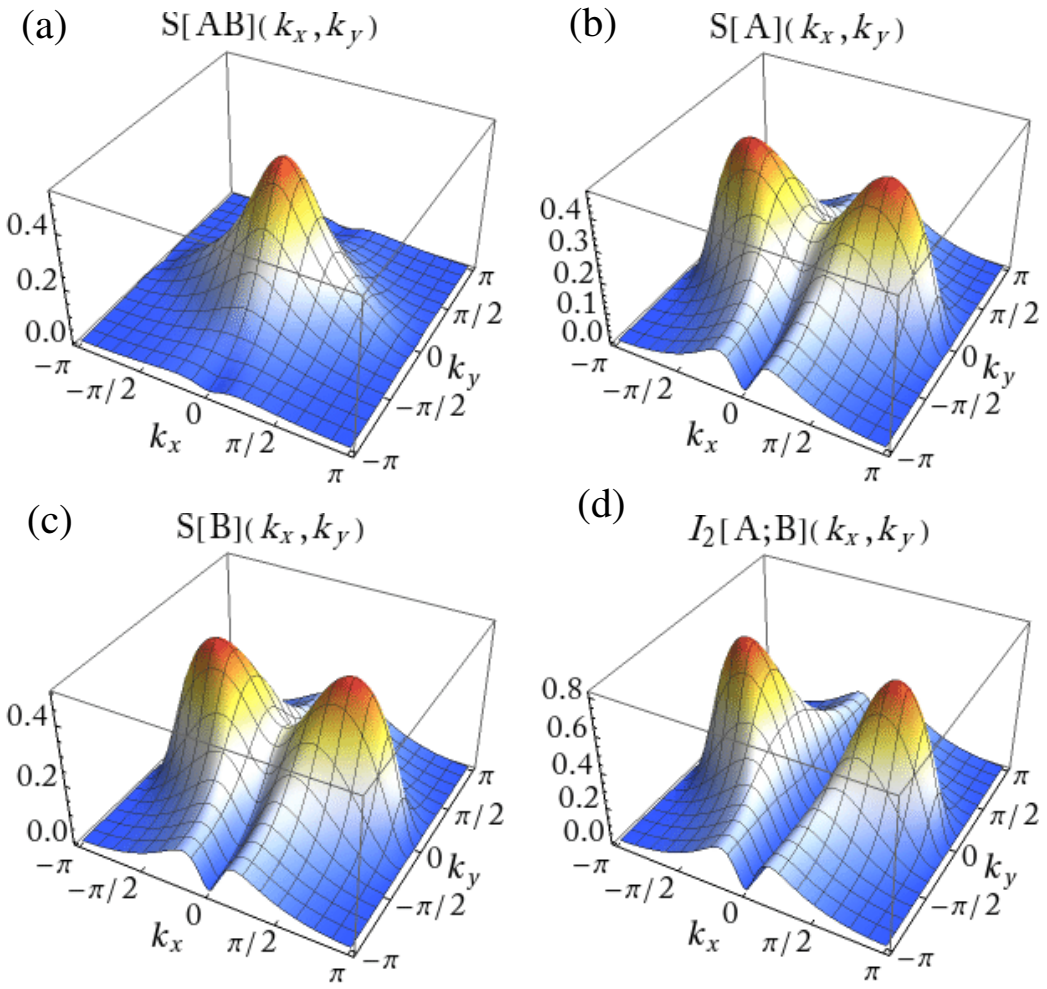

Figure 7.15: The mutual information band structure $I(\mathsf{A},\mathsf{B})(\mathbf{k})$ comprises three contributions: (a) the entanglement entropy of both regions $S(\rho_{\mathsf{AB}})(\mathbf{k})$ and (b) the entanglement entropy of each region $S(\rho_{\mathsf{A}})(\mathbf{k})$ and (c) $S(\rho_{\mathsf{B}})(\mathbf{k})$, i.e., (d) $I(\mathsf{A},\mathsf{B})(\mathbf{k}) = S(\rho_{\mathsf{A}})(\mathbf{k}) + S(\rho_{\mathsf{B}})(\mathbf{k}) - S(\rho_{\mathsf{AB}})(\mathbf{k})$. From: Thomas I. Tuegel, Victor Chua, and Taylor L. Hughes. "Embedded Topological Insulators" (2018). arXiv: 1802.06790. Credit: Victor Chua.

7.4 Embedded TI crystals

A weak TI can be treated as a crystal of embedded TIs where the layers of the weak TI are the embedded systems. The composite topological index (7.13) is a sequence of indices which repeat due to lattice translation invariance. The composite index can be summarized by an index for each lattice vector [36]. Any transverse cut through the components leads to surface states, thus accounting for the modes on certain surfaces of the weak TI. Edge dislocations can be treated as additional embedded TIs, accounting for the modes bound at those defects [125].

An antiferromagnetic TI (AFTI) is another case of an embedded TI crystal. The AFTI breaks time-reversal symmetry, but is symmetric under the magnetic space group generated by the combination of time-reversal $\mathcal{T}$ and a half-lattice-vector translation $T_{1/2}$, $S = \mathcal{T}T_{1/2}$ [29, 84, 117]. An AFTI can arise when antiferromagnetic order is imposed on a three-dimensional strong TI protected by time-reversal symmetry or when stacking two-dimensional topological insulators with alternating Chern numbers. Surfaces that do not break the magnetic space group symmetry S are gapless; the zero modes are protected by Kramers-like degeneracy in the plane with zero momentum along the half-lattice-vector translation $T_{1/2}$. The AFTI can be regarded as a crystal of embedded TIs where the composite index (7.13) is a periodic sequence of indices where the sum of indices in a single unit cell is zero. The magnetic space group symmetry is essential for the protection of the topological surface states because the topological subsystems are not well isolated.

7.5 Defects

The classification of embedded TIs predicts new robust topological modes at defects in certain bulk-trivial systems. For example, in crystals where the trivial unit cell hosts topological subunits, crystal defects such as stacking faults and partial dislocations can leave remnant embedded TI states. A simple realization of this example is a stack of alternating Chern insulators,

shown in Fig. 7.16(a), with the Hamiltonian

$$H(\mathbf{k}) = \left(\sigma^3 \otimes \sigma^1\right) \sin k_x + \left(\mathbb{1} \otimes \sigma^2\right) \sin k_y + \left(\mathbb{1} \otimes \sigma^3\right)[2 - m_1 - \cos k_x - \cos k_y] + \left(\sigma^1 \otimes \mathbb{1}\right)[\gamma_z + \delta_z \cos k_z] - \left(\sigma^3 \otimes \sigma^3\right) m_2 \tag{7.22}$$

Each unit cell contains two Chern insulator layers which are time-reversal partners. The model parameters m_1 and m_2 control the m-parameter of the individual Chern insulators. The interlayer hopping is controlled by γ_z (intra-unit cell hopping) and δ_z (inter-unit cell hopping). The model is not a strong or weak TI, and while it is similar to the antiferromagnetic TI, the hopping potentials between $\mathrm{Ch}_1 = \pm 1$ layers are chosen to break the antiferromagnetic symmetry; broken inversion symmetry also ensures it is not a mirror-symmetric crystalline TI. The layers share a symmetry and dimensionality, so the bulk topological index vanishes by Eq. (7.6); however, the model has a non-trivial classification by Eq. (7.13). Stacking faults in the trivial system, shown in Fig. 7.16(c), host protected topological modes in open boundary conditions localized at the defect, seen in Fig. 7.16(d). Partial dislocation defects, such as Fig. 7.16(e), also host topological surface states seen in Fig. 7.16(f). Both types of defect are realized in a real-space model by inverse-Fourier transforming the Hamiltonian (7.22) in the stacking direction (z) and one other direction in the plane of the Chern insulator layers (y); periodic boundary conditions are maintained in the z and x directions. In the pristine crystal, the topological substructure is hidden because the alternating layers carry opposite topological modes which couple together to open the surface gap. Stacking faults and partial dislocations reveal the topological substructure because the defect spatially separates the alternating layers so that one set of surface states is uncompensated.

7.6 Summary

In Chapter 7 we developed a classification of composite symmetry-protected topological systems based on disentangled projectors. We classify components based on the topological indices of disentangleable subsystems. We introduced embedded topological insulators and showed that our method correctly classifies embedded TIs in two and three dimensions. Our composite topological index also generalizes the description of weak TIs and

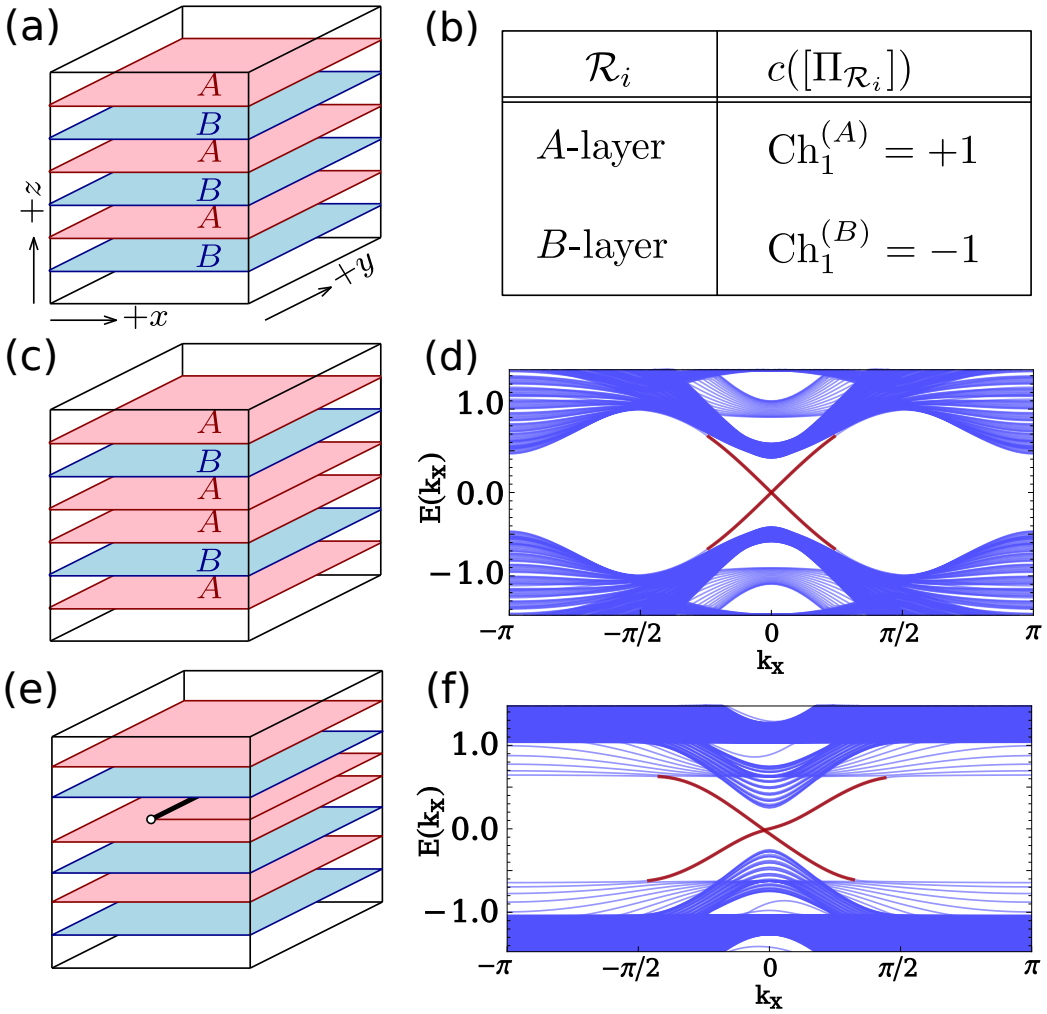

Figure 7.16: (a) Schematic of alternating stacked Chern insulators, with indices given by the table (b). (c) Schematic of a stacking fault defect and (d) energy spectrum under open boundary conditions, using parameters $m_1 = 1$, $m_2 = -0.1$, $\gamma_z = 0.05$, and $\delta_z = 0.5$. (e) Schematic of a partial dislocation defect and (f) energy spectrum under open boundary conditions, using parameters $m_1 = 1$, $m_2 = 0$, $\gamma_z = 0.5$, and $\delta_z = 0.25$. The energy spectra show the presence of topological surface states which are localized at the respective defects. The parameters are defined in Eq. (7.22). From: Thomas I. Tuegel, Victor Chua, and Taylor L. Hughes. "Embedded Topological Insulators" (2018). arXiv: 1802.06790. Credit: Victor Chua.

antiferromagnetic TIs. Finally, we showed that our classification reveals the possibility of bulk-trivial systems to carry topological modes bound at certain defects.

Chapter 8

Conclusion

We began with a review of the geometric response of the quantum Hall effect; by understanding that response in relation to the electromagnetic response, we developed and demonstrated a method to compute the Hall viscosity coefficient based on momentum transport. We applied the momentum transport method to lattice models of the quantum Hall effect, finding general agreement with continuum models, but deviation when the magnetic length scale is comparable to the lattice scale. Using our new understanding of Hall viscosity in terms of momentum transport, we reinterpreted the observation of the acoustic Faraday effect in superfluid ^{3}He−B to show that Hall viscosity leads to circular birefringence of transverse acoustic waves. In Chapter 5, we turned our attention to the reduced density matrix and methods based on the entanglement spectrum. We explored a method to compute the Hall viscosity from the entanglement spectrum and found it comparable to our previous results in continuum and lattice systems. Then we pursued a different direction based on the entanglement spectrum, finally developing a classification of composite topological systems, particularly embedded topological insulators.

Our results for the Hall viscosity of lattice models of the quantum Hall effect leave some questions unanswered. There remains some discrepancy between the momentum-transport and momentum-polarization results which is not explained. The regime of interest, where the magnetic length is comparable to the lattice size, may not be experimentally accessible, although it may be possible to impose a periodic potential to create an artificial lattice, if not in a two-dimensional electron gas then perhaps in a photonic analog.

We are excited about the observation of Hall viscosity in ^{3}He−B. An experiment that simultaneously measures the zero-field speed of sound with the acoustic Faraday effect could precisely quantify the Hall viscosity coefficient. The acoustic Faraday effect has also been predicted or observed for

other systems such as crystalline $Tb_3Ga_5O_{12}$ [123, 124] and superconductor vortex lattices [27, 28, 118]. We suggest that these systems are also promising avenues for future experimental investigations of the Hall viscosity.

Our classification of composite topological systems yields several directions for future work. We have not addressed how disorder affects the embedded phases, although our classification method still applies to that case. The classification also suggests that defects in layered antiferromagnetic materials may host embedded TIs. One promising candidate are the Sn−X (tin-halides) where topological states are predicted to coexist with antiferromagnetic order [89]. Antiferromagnetic TIs may also support embedded TIs if the magnetic group symmetry is broken.

References

[1] Alexander G Abanov. "On the effective hydrodynamics of the fractional quantum Hall effect". Journal of Physics A: Mathematical and Theoretical **46**, 292001 (2013). DOI: 10.1088/1751-8113/46/29/292001.

[2] Alexander G. Abanov and Andrey Gromov. "Electromagnetic and gravitational responses of two-dimensional noninteracting electrons in a background magnetic field". Phys. Rev. B **90**, 014435 (2014). DOI: 10.1103/PhysRevB.90.014435.

[3] Oleg Andreev, Michael Haack, and Stefan Hofmann. "On nonrelativistic diffeomorphism invariance". Phys. Rev. D **89**, 064012 (2014). DOI: 10.1103/PhysRevD.89.064012.

[4] J. E. Avron. "Odd Viscosity". J. Stat. Phys. **92**, 543–557 (1998). DOI: 10.1023/A:1023084404080.

[5] J. E. Avron, A. Raveh, and B. Zur. "Adiabatic quantum transport in multiply connected systems". Rev. Mod. Phys. **60**, 873–915 (1988). DOI: 10.1103/RevModPhys.60.873.

[6] J. E. Avron, R. Seiler, and L. G. Yaffe. "Adiabatic theorems and applications to the quantum hall effect". Communications in Mathematical Physics **110**, 33–49 (1987). DOI: 10.1007/BF01209015.

[7] J. E. Avron, R. Seiler, and P. G. Zograf. "Viscosity of Quantum Hall Fluids". Phys. Rev. Lett. **75**, 697–700 (1995). DOI: 10.1103/PhysRevLett.75.697.

[8] Debarghya Banerjee et al. “Odd viscosity in chiral active fluids”. Nature Communications **8**, 1573 (2017). DOI: 10.1038/s41467-017-01378-7.

[9] Maissam Barkeshli, Suk Bum Chung, and Xiao-Liang Qi. “Dissipationless phonon Hall viscosity”. Phys. Rev. B **85**, 245107 (2012). DOI: 10.1103/PhysRevB.85.245107.

[10] Wladimir A. Benalcazar, Jeffrey C. Y. Teo, and Taylor L. Hughes. “Classification of two-dimensional topological crystalline superconductors and Majorana bound states at disclinations”. Phys. Rev. B **89**, 224503 (2014). DOI: 10.1103/PhysRevB.89.224503.

[11] B. Andrei Bernevig, Taylor L. Hughes, and Shou-Cheng Zhang. “Quantum Spin Hall Effect and Topological Phase Transition in HgTe Quantum Wells”. Science **314**, 1757–1761 (2006). DOI: 10.1126/science.1133734.

[12] Rudro R Biswas. “Semiclassical theory of viscosity in quantum Hall states” (2013). arXiv: 1311.7149.

[13] M. Born and V. Fock. “Beweis des Adiabatensatzes”. Zeitschrift für Physik **51**, 165–180 (1928). DOI: 10.1007/BF01343193.

[14] Barry Bradlyn, Moshe Goldstein, and N. Read. “Kubo formulas for viscosity: Hall viscosity, Ward identities, and the relation with conductivity”. Phys. Rev. B **86**, 245309 (2012). DOI: 10.1103/PhysRevB.86.245309.

[15] Barry Bradlyn and N. Read. “Low-energy effective theory in the bulk for transport in a topological phase”. Phys. Rev. B **91**, 125303 (2015). DOI: 10.1103/PhysRevB.91.125303.

[16] Pasquale Calabrese and Alexandre Lefevre. “Entanglement spectrum in one-dimensional systems”. Phys. Rev. A **78**, 032329 (2008). DOI: 10.1103/PhysRevA.78.032329.

[17] T. Can, M. Laskin, and P. Wiegmann. “Fractional Quantum Hall Effect in a Curved Space: Gravitational Anomaly and Electromag-

netic Response". Phys. Rev. Lett. **113**, 046803 (2014). DOI: 10.1103/PhysRevLett.113.046803.

[18] A. H. Castro Neto et al. "The electronic properties of graphene". Rev. Mod. Phys. **81**, 109–162 (2009). DOI: 10.1103/RevModPhys.81.109.

[19] Ching-Kai Chiu et al. "Classification of topological quantum matter with symmetries". Rev. Mod. Phys. **88**, 035005 (2016). DOI: 10.1103/RevModPhys.88.035005.

[20] Gil Young Cho, Yizhi You, and Eduardo Fradkin. "Geometry of fractional quantum Hall fluids". Phys. Rev. B **90**, 115139 (2014). DOI: 10.1103/PhysRevB.90.115139.

[21] Gil Young Cho et al. "Condensation of lattice defects and melting transitions in quantum Hall phases". Phys. Rev. B **91**, 035122 (2015). DOI: 10.1103/PhysRevB.91.035122.

[22] J. Ignacio Cirac et al. "Entanglement spectrum and boundary theories with projected entangled-pair states". Phys. Rev. B **83**, 245134 (2011). DOI: 10.1103/PhysRevB.83.245134.

[23] C. A. Collett et al. "Zeeman Splitting and Nonlinear Field-Dependence in Superfluid ^{3}He". J. Low Temp. Phys. **171**, 214–219 (2013). DOI: 10.1007/s10909-012-0692-6.

[24] Alberto Cortijo et al. "Elastic Gauge Fields in Weyl Semimetals". Phys. Rev. Lett. **115**, 177202 (2015). DOI: 10.1103/PhysRevLett.115.177202.

[25] G. De Chiara et al. "Entanglement Spectrum, Critical Exponents, and Order Parameters in Quantum Spin Chains". Phys. Rev. Lett. **109**, 237208 (2012). DOI: 10.1103/PhysRevLett.109.237208.

[26] Dong-Ling Deng, Xiaopeng Li, and S. Das Sarma. "Quantum Entanglement in Neural Network States". Phys. Rev. X **7**, 021021 (2017). DOI: 10.1103/PhysRevX.7.021021.

[27] D. Domínguez et al. “Interaction of Vortex Lattice with Ultrasound and the Acoustic Faraday Effect”. Phys. Rev. Lett. **74**, 2579–2582 (1995). DOI: 10.1103/PhysRevLett.74.2579.

[28] D. Domínguez et al. “Interaction of vortices with ultrasound and the acoustic Faraday effect in type-II superconductors”. Phys. Rev. B **53**, 6682–6692 (1996). DOI: 10.1103/PhysRevB.53.6682.

[29] Mildred S Dresselhaus, Gene Dresselhaus, and Ado Jorio. *Group Theory. Application to the Physics of Condensed Catter*. Springer-Verlag Berlin Heidelberg, (2008). DOI: 10.1007/978-3-540-32899-5.

[30] J. Dubail, N. Read, and E. H. Rezayi. “Real-space entanglement spectrum of quantum Hall systems”. Phys. Rev. B **85**, 115321 (2012). DOI: 10.1103/PhysRevB.85.115321.

[31] Lukasz Fidkowski. “Entanglement Spectrum of Topological Insulators and Superconductors”. Phys. Rev. Lett. **104**, 130502 (2010). DOI: 10.1103/PhysRevLett.104.130502.

[32] Eduardo Fradkin. *Field theories of condensed matter physics*. Cambridge University Press, (2013).

[33] Daniel S. Freed and Gregory W. Moore. “Twisted Equivariant Matter”. Annales Henri Poincaré. **14**, 1927–2023. (2013). 8. DOI: 10.1007/s00023-013-0236-x.

[34] M. Fremling, T. H. Hansson, and J. Suorsa. “Hall viscosity of hierarchical quantum Hall states”. Phys. Rev. B **89**, 125303 (2014). DOI: 10.1103/PhysRevB.89.125303.

[35] Liang Fu. “Topological Crystalline Insulators”. Phys. Rev. Lett. **106**, 106802 (2011). DOI: 10.1103/PhysRevLett.106.106802.

[36] Liang Fu, C. L. Kane, and E. J. Mele. “Topological Insulators in Three Dimensions”. Phys. Rev. Lett. **98**, 106803 (2007). DOI: 10.1103/PhysRevLett.98.106803.

[37] Keisuke Fujii and Yusuke Nishida. "Low-energy effective field theory of superfluid ^{3}He−B and its gyromagnetic and Hall responses" (2016). arXiv: 1610.06330.

[38] Takahiro Fukui and Yasuhiro Hatsugai. "Entanglement Chern Number for an Extensive Partition of a Topological Ground State". Journal of the Physical Society of Japan **83**, 113705 (2014). DOI: 10.7566/JPSJ.83.113705.

[39] Takahiro Fukui, Ken-Ichiro Imura, and Yasuhiro Hatsugai. "Symmetry Protected Weak Topological Phases in a Superlattice". Journal of the Physical Society of Japan **82**, 073708 (2013). DOI: 10.7566/JPSJ.82.073708.

[40] Michael Geracie et al. "Spacetime symmetries of the quantum Hall effect". Phys. Rev. D **91**, 045030 (2015). DOI: 10.1103/PhysRevD.91.045030.

[41] Paul H Ginsparg. "Applied conformal field theory" (1988). arXiv: hep-th/9108028.

[42] Andrey Gromov and Alexander G. Abanov. "Density-Curvature Response and Gravitational Anomaly". Phys. Rev. Lett. **113**, 266802 (2014). DOI: 10.1103/PhysRevLett.113.266802.

[43] Andrey Gromov and Alexander G. Abanov. "Thermal Hall Effect and Geometry with Torsion". Phys. Rev. Lett. **114**, 016802 (2015). DOI: 10.1103/PhysRevLett.114.016802.

[44] Andrey Gromov et al. "Framing Anomaly in the Effective Theory of the Fractional Quantum Hall Effect". Phys. Rev. Lett. **114**, 016805 (2015). DOI: 10.1103/PhysRevLett.114.016805.

[45] F. D. M. Haldane. "Hall viscosity and intrinsic metric of incompressible fractional Hall fluids" (2009). arXiv: 0906.1854.

[46] W. P. Halperin and E. Varoquaux. "Order-Parameter Collective Modes in Superfluid ^{3}He". *Helium Three*. Ed. by W. P. Halperin and L. P. Pitaevskii. Vol. 26. Modern Problems in Condensed Matter Sciences.

Elsevier, (1990). Chap. 7, 353–522. DOI: 10.1016/B978-0-444-87476-4.50013-3.

[47] M. Z. Hasan and C. L. Kane. "Colloquium: Topological insulators". Rev. Mod. Phys. **82**, 3045–3067 (2010). DOI: 10.1103/RevModPhys.82.3045.

[48] Yasuhiro Hatsugai. "Edge states in the integer quantum Hall effect and the Riemann surface of the Bloch function". Phys. Rev. B **48**, 11851–11862 (1993). DOI: 10.1103/PhysRevB.48.11851.

[49] Yoshimasa Hidaka et al. "Viscoelastic-electromagnetism and Hall viscosity". Progress of Theoretical and Experimental Physics **2013**, 013A02 (2013). DOI: 10.1093/ptep/pts063.

[50] Douglas R. Hofstadter. "Energy levels and wave functions of Bloch electrons in rational and irrational magnetic fields". Phys. Rev. B **14**, 2239–2249 (1976). DOI: 10.1103/PhysRevB.14.2239.

[51] Carlos Hoyos, Sergej Moroz, and Dam Thanh Son. "Effective theory of chiral two-dimensional superfluids". Phys. Rev. B **89**, 174507 (2014). DOI: 10.1103/PhysRevB.89.174507.

[52] Carlos Hoyos and Dam Thanh Son. "Hall Viscosity and Electromagnetic Response". Phys. Rev. Lett. **108**, 066805 (2012). DOI: 10.1103/PhysRevLett.108.066805.

[53] Timothy H. Hsieh and Liang Fu. "Bulk Entanglement Spectrum Reveals Quantum Criticality within a Topological State". Phys. Rev. Lett. **113**, 106801 (2014). DOI: 10.1103/PhysRevLett.113.106801.

[54] Timothy H. Hsieh, Liang Fu, and Xiao-Liang Qi. "Tensor network implementation of bulk entanglement spectrum". Phys. Rev. B **90**, 085137 (2014). DOI: 10.1103/PhysRevB.90.085137.

[55] Biao Huang. "Hall viscosity revealed via density response". Phys. Rev. B **91**, 235101 (2015). DOI: 10.1103/PhysRevB.91.235101.

[56] Zhoushen Huang et al. “Invariance of Topological Indices Under Hilbert Space Truncation”. Phys. Rev. Lett. **120**, 016403 (2018). DOI: 10.1103/PhysRevLett.120.016403.

[57] Taylor L. Hughes, Robert G. Leigh, and Eduardo Fradkin. “Torsional Response and Dissipationless Viscosity in Topological Insulators”. Phys. Rev. Lett. **107**, 075502 (2011). DOI: 10.1103/PhysRevLett.107.075502.

[58] Taylor L. Hughes, Robert G. Leigh, and Onkar Parrikar. “Torsional anomalies, Hall viscosity, and bulk-boundary correspondence in topological states”. Phys. Rev. D **88**, 025040 (2013). DOI: 10.1103/PhysRevD.88.025040.

[59] C. L. Kane and E. J. Mele. “Quantum Spin Hall Effect in Graphene”. Phys. Rev. Lett. **95**, 226801 (2005). DOI: 10.1103/PhysRevLett.95.226801.

[60] C. L. Kane and E. J. Mele. “Z_2 Topological Order and the Quantum Spin Hall Effect”. Phys. Rev. Lett. **95**, 146802 (2005). DOI: 10.1103/PhysRevLett.95.146802.

[61] Tosio Kato. “On the Adiabatic Theorem of Quantum Mechanics”. Journal of the Physical Society of Japan **5**, 435–439 (1950). DOI: 10.1143/JPSJ.5.435.

[62] Taro Kimura. “Hall and spin Hall viscosity ratio in topological insulators” (2010). arXiv: 1004.2688.

[63] Alexei Kitaev. “Periodic table for topological insulators and superconductors”. AIP Conference Proceedings. **1134**, 22–30. (2009).

[64] Ryogo Kubo. “Statistical-Mechanical Theory of Irreversible Processes. I. General Theory and Simple Applications to Magnetic and Conduction Problems”. J. Phys. Soc. Jpn. **12**, 570–586 (1957). DOI: 10.1143/JPSJ.12.570.

[65] L. D. Landau. “Oscillations in a Fermi Liquid”. Soviet Physics: J. Exp. Theor. Phys. **5**, 101 (1957).

[66] L. D. Landau, E. M. Liftshitz, and L. P. Pitaevskii. *Electrodynamics of Continuous Media*. 2nd ed. Pergamon Press, (1984).

[67] L. D. Landau et al. *Theory of Elasticity*. 3rd ed. Elsevier, (1986).

[68] Karl Landsteiner, Yan Liu, and Ya-Wen Sun. "Odd Viscosity in the Quantum Critical Region of a Holographic Weyl Semimetal". Phys. Rev. Lett. **117**, 081604 (2016). DOI: 10.1103/PhysRevLett.117.081604.

[69] R. B. Laughlin. "Quantized Hall conductivity in two dimensions". Phys. Rev. B **23**, 5632–5633 (1981). DOI: 10.1103/PhysRevB.23.5632.

[70] D. T. Lawson et al. "Attenuation of Zero Sound and the Low-Temperature Transitions in Liquid ^{3}He". Phys. Rev. Lett. **30**, 541–544 (1973). DOI: 10.1103/PhysRevLett.30.541.

[71] Y. Lee et al. "Discovery of the acoustic Faraday effect in superfluid ^{3}He−B". Nature **400**, 431–433 (1999). DOI: 10.1038/22712.

[72] Anthony J. Leggett. "A theoretical description of the new phases of liquid He 3". Rev. Mod. Phys. **47**, 331–414 (1975). DOI: 10.1103/RevModPhys.47.331.

[73] Péter Lévay. "Berry phases for Landau Hamiltonians on deformed tori". Journal of Mathematical Physics **36**, 2792–2802 (1995). DOI: 10.1063/1.531066.

[74] Hui Li and F. D. M. Haldane. "Entanglement Spectrum as a Generalization of Entanglement Entropy: Identification of Topological Order in Non-Abelian Fractional Quantum Hall Effect States". Phys. Rev. Lett. **101**, 010504 (2008). DOI: 10.1103/PhysRevLett.101.010504.

[75] Donghao Liu and Junren Shi. "Circular Phonon Dichroism in Weyl Semimetals". Phys. Rev. Lett. **119**, 075301 (2017). DOI: 10.1103/PhysRevLett.119.075301.

[76] Nicholas Loehr. *Advanced Linear Algebra*. Textbooks in Mathematics. CRC Press, (2014).

[77] Chi-Ken Lu, Dah-Wei Chiou, and Feng-Li Lin. "Manifestations of topological band crossings in bulk entanglement spectrum: An analytical study for integer quantum Hall states". Phys. Rev. B **92**, 075130 (2015). DOI: 10.1103/PhysRevB.92.075130.

[78] Kazumi Maki. "Propagation of zero sound in the Balian-Werthamer state". J. Low Temp. Phys. **16**, 465–477 (1974). DOI: 10.1007/BF00654896.

[79] Kazumi Maki. "Collective modes and spin waves in superfluid ^{3}He−B". J. Low Temp. Phys. **24**, 755–768 (1976). DOI: 10.1007/BF00657178.

[80] Kazumi Maki and Hiromichi Ebisawa. "Transverse zero sound in superfluid ^{3}He−B". J. Low Temp. Phys. **26**, 627–636 (1977). DOI: 10.1007/BF00655435.

[81] Michael P. Marder. *Condensed Matter Physics*. 2nd ed. John Wiley & Sons, Inc., (2010).

[82] Ross H. McKenzie and J. A. Sauls. "Collective Modes and Nonlinear Acoustics in Superfluid ^{3}He−B". *Helium Three*. Ed. by W. P. Halperin and L. P. Pitaevskii. Vol. 26. Modern Problems in Condensed Matter Sciences. Elsevier, (1990). Chap. 5, 255–311. DOI: 10.1016/B978-0-444-87476-4.50011-X.

[83] Ian Mondragon-Shem et al. "Topological Criticality in the Chiral-Symmetric AIII Class at Strong Disorder". Phys. Rev. Lett. **113**, 046802 (2014). DOI: 10.1103/PhysRevLett.113.046802.

[84] Roger S. K. Mong, Andrew M. Essin, and Joel E. Moore. "Antiferromagnetic topological insulators". Phys. Rev. B **81**, 245209 (2010). DOI: 10.1103/PhysRevB.81.245209.

[85] J. E. Moore and L. Balents. "Topological invariants of time-reversal-invariant band structures". Phys. Rev. B **75**, 121306 (2007). DOI: 10.1103/PhysRevB.75.121306.

[86] G. F. Moores and J. A. Sauls. "Transverse waves in superfluid ^{3}He−B". J. Low Temp. Phys. **91**, 13–37 (1993). DOI: 10.1007/bf00132087.

[87] Dung Xuan Nguyen, Dam Thanh Son, and Chaolun Wu. "Lowest Landau Level Stress Tensor and Structure Factor of Trial Quantum Hall Wave Functions" (2014). arXiv: 1411.3316.

[88] Evert P. L. van Nieuwenburg, Ye-Hua Liu, and Sebastian D. Huber. "Learning phase transitions by confusion". Nature Physics **13**, 435 (2017). DOI: 10.1038/nphys4037.

[89] C Niu et al. "Quantum spin Hall effect and topological phase transitions in honeycomb antiferromagnets" (2017). arXiv: 1705.07035.

[90] Qian Niu, D. J. Thouless, and Yong-Shi Wu. "Quantized Hall conductance as a topological invariant". Phys. Rev. B **31**, 3372–3377 (1985). DOI: 10.1103/PhysRevB.31.3372.

[91] Masanori Ohya and Dénes Petz. *Quantum Entropy and Its Use*. Texts and Monographs in Physics. Springer-Verlag, (1993).

[92] YeJe Park and F. D. M. Haldane. "Guiding-center Hall viscosity and intrinsic dipole moment along edges of incompressible fractional quantum Hall fluids". Phys. Rev. B **90**, 045123 (2014). DOI: 10.1103/PhysRevB.90.045123.

[93] Onkar Parrikar, Taylor L. Hughes, and Robert G. Leigh. "Torsion, parity-odd response, and anomalies in topological states". Phys. Rev. D **90**, 105004 (2014). DOI: 10.1103/PhysRevD.90.105004.

[94] D. N. Paulson, R. T. Johnson, and J. C. Wheatley. "Propagation of Collisionless Sound in Normal and Extraordinary Phases of Liquid ^{3}He below 3 mK". Phys. Rev. Lett. **30**, 829–833 (1973). DOI: 10.1103/PhysRevLett.30.829.

[95] Ingo Peschel. "Calculation of reduced density matrices from correlation functions". Journal of Physics A: Mathematical and General **36**, L205 (2003). DOI: 10.1088/0305-4470/36/14/101.

[96] Ingo Peschel and Viktor Eisler. "Reduced density matrices and entanglement entropy in free lattice models". Journal of Physics A: Mathematical and Theoretical **42**, 504003 (2009). DOI: 10.1088/1751-8113/42/50/504003.

[97] Frank Pollmann et al. "Entanglement spectrum of a topological phase in one dimension". Phys. Rev. B **81**, 064439 (2010). DOI: 10.1103/PhysRevB.81.064439.

[98] Emil Prodan, Taylor L. Hughes, and B. Andrei Bernevig. "Entanglement Spectrum of a Disordered Topological Chern Insulator". Phys. Rev. Lett. **105**, 115501 (2010). DOI: 10.1103/PhysRevLett.105.115501.

[99] Xiao-Liang Qi, Taylor L. Hughes, and Shou-Cheng Zhang. "Topological field theory of time-reversal invariant insulators". Phys. Rev. B **78**, 195424 (2008). DOI: 10.1103/PhysRevB.78.195424.

[100] Xiao-Liang Qi, Hosho Katsura, and Andreas W. W. Ludwig. "General Relationship between the Entanglement Spectrum and the Edge State Spectrum of Topological Quantum States". Phys. Rev. Lett. **108**, 196402 (2012). DOI: 10.1103/PhysRevLett.108.196402.

[101] Xiao-Liang Qi and Shou-Cheng Zhang. "Topological insulators and superconductors". Rev. Mod. Phys. **83**, 1057–1110 (2011). DOI: 10.1103/RevModPhys.83.1057.

[102] Xiao-Liang Qi et al. "Time-Reversal-Invariant Topological Superconductors and Superfluids in Two and Three Dimensions". Phys. Rev. Lett. **102**, 187001 (2009). DOI: 10.1103/PhysRevLett.102.187001.

[103] Ying Ran, Yi Zhang, and Ashvin Vishwanath. "One-dimensional topologically protected modes in topological insulators with lattice dislocations". Nature Physics **5**, 298–303 (2009). DOI: 10.1038/nphys1220.

[104] N. Read. "Non-Abelian adiabatic statistics and Hall viscosity in quantum Hall states and $p_x + ip_y$ paired superfluids". Phys. Rev. B **79**, 045308 (2009). DOI: 10.1103/PhysRevB.79.045308.

[105] N. Read and E. H. Rezayi. "Hall viscosity, orbital spin, and geometry: Paired superfluids and quantum Hall systems". Phys. Rev. B **84**, 085316 (2011). DOI: 10.1103/PhysRevB.84.085316.

[106] Iván D. Rodríguez and Germán Sierra. "Entanglement entropy of integer quantum Hall states". Phys. Rev. B **80**, 153303 (2009). DOI: 10.1103/PhysRevB.80.153303.

[107] Rahul Roy. "Topological phases and the quantum spin Hall effect in three dimensions". Phys. Rev. B **79**, 195322 (2009). DOI: 10.1103/PhysRevB.79.195322.

[108] Shinsei Ryu, Joel E. Moore, and Andreas W. W. Ludwig. "Electromagnetic and gravitational responses and anomalies in topological insulators and superconductors". Phys. Rev. B **85**, 045104 (2012). DOI: 10.1103/PhysRevB.85.045104.

[109] Shinsei Ryu et al. "Topological insulators and superconductors: tenfold way and dimensional hierarchy". New J. Phys. **12**, 065010 (2010). DOI: 10.1088/1367-2630/12/6/065010.

[110] Raul A. Santos, Chao-Ming Jian, and Rex Lundgren. "Bulk entanglement spectrum in gapped spin ladders". Phys. Rev. B **93**, 245101 (2016). DOI: 10.1103/PhysRevB.93.245101.

[111] J. A. Sauls and J. W. Serene. "Interaction Effects on the Zeeman Splitting of Collective Modes in Superfluid ^{3}He−B". Phys. Rev. Lett. **49**, 1183–1186 (1982). DOI: 10.1103/PhysRevLett.49.1183.

[112] Nathan Schine et al. "Synthetic Landau levels for photons". Nature **534**. Letter, 671–675 (2016). DOI: 10.1038/nature17943.

[113] Andreas P. Schnyder et al. "Classification of topological insulators and superconductors in three spatial dimensions". Phys. Rev. B **78**, 195125 (2008). DOI: 10.1103/PhysRevB.78.195125.

[114] N. Schopohl and L. Tewordt. "Landé factors of collective mode multiplets in ^{3}He−B and coupling strengths to sound waves". J. of Low Temp. Phys. **45**, 67–90 (1981). DOI: 10.1007/BF00661143.

[115] Hassan Shapourian, Taylor L. Hughes, and Shinsei Ryu. "Viscoelastic response of topological tight-binding models in two and three dimensions". Phys. Rev. B **92**, 165131 (2015). DOI: 10.1103/PhysRevB.92.165131.

[116] Ken Shiozaki and Masatoshi Sato. "Topology of crystalline insulators and superconductors". Phys. Rev. B **90**, 165114 (2014). DOI: 10.1103/PhysRevB.90.165114.

[117] Libor Šmejkal et al. "Topological antiferromagnetic spintronics: Part of a collection of reviews on antiferromagnetic spintronics" (2017). arXiv: 1706.00670.

[118] E. B. Sonin. "Interaction of Ultrasound with Vortices in Type-II Superconductors". Phys. Rev. Lett. **76**, 2794–2797 (1996). DOI: 10.1103/PhysRevLett.76.2794.

[119] A. Sterdyniak et al. "Real-space entanglement spectrum of quantum Hall states". Phys. Rev. B **85**, 125308 (2012). DOI: 10.1103/PhysRevB.85.125308.

[120] Michael Stone. "Gravitational anomalies and thermal Hall effect in topological insulators". Phys. Rev. B **85**, 184503 (2012). DOI: 10.1103/PhysRevB.85.184503.

[121] Michael Stone, Ching-Kai Chiu, and Abhishek Roy. "Symmetries, dimensions and topological insulators: the mechanism behind the face of the Bott clock". Journal of Physics A: Mathematical and Theoretical **44**, 045001 (2011). DOI: 10.1088/1751-8113/44/4/045001.

[122] Michael Stone and Paul Goldbart. *Mathematics for Physics*. Cambridge University Press, (2009).

[123] C. Strohm, G. L. J. A. Rikken, and P. Wyder. "Phenomenological Evidence for the Phonon Hall Effect". Phys. Rev. Lett. **95**, 155901 (2005). DOI: 10.1103/PhysRevLett.95.155901.

[124] A. Sytcheva et al. "Acoustic Faraday effect in $Tb_3Ga_5O_{12}$". Phys. Rev. B **81**, 214415 (2010). DOI: 10.1103/PhysRevB.81.214415.

[125] Jeffrey C. Y. Teo and C. L. Kane. "Topological defects and gapless modes in insulators and superconductors". Phys. Rev. B **82**, 115120 (2010). DOI: 10.1103/PhysRevB.82.115120.

[126] Ronny Thomale, D. P. Arovas, and B. Andrei Bernevig. "Nonlocal Order in Gapless Systems: Entanglement Spectrum in Spin Chains". Phys. Rev. Lett. **105**, 116805 (2010). DOI: 10.1103/PhysRevLett.105.116805.

[127] D. J. Thouless et al. "Quantized Hall Conductance in a Two-Dimensional Periodic Potential". Phys. Rev. Lett. **49**, 405–408 (1982). DOI: 10.1103/PhysRevLett.49.405.

[128] I V Tokatly and G Vignale. "Lorentz shear modulus of fractional quantum Hall states". Journal of Physics: Condensed Matter **21**, 275603 (2009). DOI: 10.1088/0953-8984/21/27/275603.

[129] Andrea Tomadin, Giovanni Vignale, and Marco Polini. "Corbino Disk Viscometer for 2D Quantum Electron Liquids". Phys. Rev. Lett. **113**, 235901 (2014). DOI: 10.1103/PhysRevLett.113.235901.

[130] Hong-Hao Tu, Yi Zhang, and Xiao-Liang Qi. "Momentum polarization: An entanglement measure of topological spin and chiral central charge". Phys. Rev. B **88**, 195412 (2013). DOI: 10.1103/PhysRevB.88.195412.

[131] Thomas I. Tuegel, Victor Chua, and Taylor L. Hughes. "Embedded Topological Insulators" (2018). arXiv: 1802.06790.

[132] Thomas I. Tuegel and Taylor L. Hughes. "Hall viscosity and momentum transport in lattice and continuum models of the integer quantum Hall effect in strong magnetic fields". Phys. Rev. B **92**, 165127 (2015). DOI: 10.1103/PhysRevB.92.165127.

[133] Thomas I. Tuegel and Taylor L. Hughes. "Hall viscosity and the acoustic Faraday effect". Phys. Rev. B **96**, 174524 (2017). DOI: 10.1103/PhysRevB.96.174524.

[134] Ari M. Turner, Yi Zhang, and Ashvin Vishwanath. "Entanglement and inversion symmetry in topological insulators". Phys. Rev. B **82**, 241102 (2010). DOI: 10.1103/PhysRevB.82.241102.

[135] D. Vollhardt and P. Wölfle. *The Superfluid Phases of Helium 3*. Taylor & Francis, (1990).

[136] X. G. Wen and A. Zee. "Shift and spin vector: New topological quantum numbers for the Hall fluids". Phys. Rev. Lett. **69**, 953–956 (1992). DOI: 10.1103/PhysRevLett.69.953.

[137] Xiao-Gang Wen. *Quantum Field Theory of Many Body Systems*. Oxford Univ. Press, (2004).

[138] P. Wiegmann. "Nonlinear Hydrodynamics and Fractionally Quantized Solitons at the Fractional Quantum Hall Edge". Phys. Rev. Lett. **108**, 206810 (2012). DOI: 10.1103/PhysRevLett.108.206810.

[139] Michael M. Wolf et al. "Area Laws in Quantum Systems: Mutual Information and Correlations". Phys. Rev. Lett. **100**, 070502 (2008). DOI: 10.1103/PhysRevLett.100.070502.

[140] Hong Yao and Xiao-Liang Qi. "Entanglement Entropy and Entanglement Spectrum of the Kitaev Model". Phys. Rev. Lett. **105**, 080501 (2010). DOI: 10.1103/PhysRevLett.105.080501.

[141] A. D. Zabolotskiy and Yu. E. Lozovik. "Strain-induced pseudomagnetic field in the Dirac semimetal borophene". Phys. Rev. B **94**, 165403 (2016). DOI: 10.1103/PhysRevB.94.165403.

[142] Michael P. Zaletel, Roger S. K. Mong, and Frank Pollmann. "Topological Characterization of Fractional Quantum Hall Ground States from Microscopic Hamiltonians". Phys. Rev. Lett. **110**, 236801 (2013). DOI: 10.1103/PhysRevLett.110.236801.

[143] Qiong Zhu, Xin Wan, and Guang-Ming Zhang. "Topologically distinct critical theories emerging from the bulk entanglement spectrum of integer quantum Hall states on a lattice". Phys. Rev. B **90**, 235134 (2014). DOI: 10.1103/PhysRevB.90.235134.